STATISTICAL PROPERTIES OF SPECKLE IN SYNTHETIC APERTURE RADAR IMAGES AND APPLICATIONS TO FORESTS AND THE OCEAN

HAIPENG WANG

Kochi University of Technology

DISSERTATION

Submitted for the degree of Doctor of Philosophy
Graduate School of Engineering
Environmental Systems Engineering
Kochi University of Technology, 2006

Kochi, Japan

Abstract

This thesis is concerned with the analysis of statistical properties of speckle in synthetic aperture radar (SAR) images, and its applications to extracting information on forests and to examining the validity of speckle reduction in SAR images of dynamic sea surfaces.

The manifestation and origin of speckle in optical and SAR images, and the outline of the thesis are first presented in Chapter 1. In Chapter 2, the fundamental statistical properties of speckle in general and speckle in SAR images are described, followed by the theories of Gaussian and non-Gaussian statistics. The principal difference between the Gaussian and non-Gaussian speckle is that the former does not contain information on scattering objects, while the latter does. Thus, the Gaussian speckle, in general, is treated as noise (except such techniques as speckle interferometry in astronomy, metallurgy and radar). Since the non-Gaussian speckle does carry information on the scattering objects, it is used to extract the statistical properties on the scattering objects. The frequently used non-Gaussian speckle models include the log-normal, Weibull, gamma and K-distributions, and their probability density functions (PDF) and the corresponding parameters are introduced using simulated speckle images. Several methods of parameter estimation are then described.

Before proceeding to the applications of SAR speckle, the SAR systems are introduced in Chapter 3. In this chapter, the processes through which the point spread function (PSF) is produced are described with the definition of spatial resolution both in the range (cross-track) and azimuth (along-track) directions. Multilook processing is briefly illustrated, followed by the statistical properties of a random rough surface and SAR images. In Chapter 4, SAR polarimetry is described to show its ability and inability in the analysis of SAR images of vegetation, namely rice plants, and forests. The 3-component decomposition analysis for full polarization data is carried out for Pi-SAR data over the Kojima rice fields and Tomakomai forests. The results of rice fields show that double bounce scattering is observed in some rice fields at L-band, but at X-band the backscatter is dominated by the surface scattering. For the Tomakomai forests, volume scattering is the main scattering at L-band, while the backscattering is dominated by surface scattering at X-band. Moreover, for the deciduous broadleaf trees and Japanese larch areas, volume scattering dominates the backscattering when their leaves fall in winter. The polarimetric analysis described in this chapter shows

that polarimetry is certainly useful for classifying different scattering processes (surface, double-bounce and volume) and hence image classification, but it is difficult to extract information in a single scattering process, *e.g.*, biomass of rice plants and forest trees.

Applications of non-Gaussian SAR speckle in forestry are presented in Chapter 5. The purpose of the study is to search the quantitative relation between tree parameters and high-resolution polarimetric SAR data. The approach we have taken is to utilize the non-Gaussian texture information in the polarimetric airborne Pi-SAR data over the coniferous forests in Hokkaido, Japan. The test areas of the Tomakomai National Forests are dominated with conifers of four main species: Japanese larch, Todo-fir, Yezo-spruce and Sakhalin-spruce. The radar cross section (RCS) in terms of forest parameters is first analyzed. It is found that the both X- and L-band RCS increase as the forest parameters increase and saturate at certain RCS levels. However, the X-band RCS data are not well correlated with forest parameters, and the saturation levels are difficult to define. The L-band RCS saturation levels are found approximately to the biomass of 40 tons/ha, the tree age of 30 years, the basal area of 30 m^2/ha, and the tree height of 8 m. The PDF of image amplitude is then investigated, and among Rayleigh, log-normal, Weibull and K-distributions, the K-distribution is found to fit best to the L-band data of all polarizations according to the Akaike information criterion (AIC). The relations between the order parameter of K-distribution and tree parameters are then investigated. It is found that the tree biomass correlated best with the order parameter. Moreover, the order parameter increases consistently with biomass to approximately 100 tons/ha which is well beyond the saturation limit of the L-band RCS. Thus, the regression curve of the order parameter in terms of tree biomass can be used to estimate the biomass beyond RCS saturation level. To evaluate this K-distribution empirical model, the ground truth data of 23 test sites were collected in August and September, 2005. Comparison between the tree biomass predicted by the model and the ground truth data shows the model accuracy of approximately 85%. It is concluded that, at least for the Hokkaido forests, this empirical model is an effective and superior way of estimating forest biomass from polarimetric SAR data in comparison with the conventional RCS model.

In Chapter 6, the interlook cross-correlation function (CCF) of Gaussian speckle is investigated in the images of dynamic sea surfaces. Multilook processing is a well-known technique for speckle reduction by dividing full aperture into several non-overlapped sub-apertures and the corresponding sub-images are formed independently. Since the spackle patterns produced by this technique are uncorrelated between looks, the speckle noise is reduced by addition of the sub-images on an intensity basis. It has been suggested that the partially overlapped sub-apertures can produce uncorrelated speckle patterns in the sub-images of dynamic ocean surfaces, and an extra look can be extracted for further speckle reduction. For testing this hypothesis, a

general integral expression is derived and discussed for the CCF of speckle patterns in SAR images processed by using partially overlapped sub-apertures of arbitrary Doppler center frequencies (or equivalent azimuth times). It is shown that, under the white noise approximation for the backscattered field, the CCF of the interlook speckle intensity patterns is given by the squared modulus of the autocorrelation function of the amplitude weighting function of sub-apertures where the time lag is the center time difference. It is also shown that the CCF of the interlook speckle patterns is independent of the surface coherence time of sea surface. The partially overlapped sub-aperture therefore cannot be used to improve the speckle reduction based on the conventional multilook processing with non-overlapping sub-apertures. The integral expression for the intensity CCF is then evaluated for a rectangular weighting function, and comparison is made with the JERS-1 L-band and RADARSAT-1 C-band SAR images of sea surface to test the theory. The CCFs computed from the JERS-1 SAR data show excellent agreement with the theory, and good agreement is obtained with the RADARSAT-1 data.

In Chapter 7, the conclusions of the present thesis are summarized and future studies are suggested.

The polarimetric analyses of rice fields and forests described in Chapter 4, the theories and experimental results presented in Chapter 5 and Chapter 6 constitute new results in the field of radar remote sensing.

Acknowledgements

My gratitude must go first to my supervisor Professor Kazuo Ouchi who gave me such a chance three years ago to pursue a doctorial degree in KUT and from then on who has been patiently guiding me through the followed years of study and research. Without his consistent help, constructive suggestions and fatherly encouragement, this thesis would not be fulfilled. Truly all that Professor Kazuo Ouchi has done for me will be cherished for the rest of my life.

I would extend my thanks to Drs. Manabu Watanabe, Masanobu Shimada and the students from Tokai University for their help when the ground truth data were collected. JAXA, NICT and Mitsubishi Heavy Industries Ltd. are also in the range of acknowledgements for providing the data used in this research. Help from Drs. Glen Davidson, Toshifumi Moriyama and Jeong Jong Heyok is genuinely appreciated, and to them as well as the researchers whose name can't be listed here due to the limit of space but whose work has definitely contributed to the fulfillment of this thesis, I acknowledge my debts.

I also truly feel it imperative to appreciate the financial assistance from Kochi University of Technology and the Nakajima Heiwa Foundation.

One of the reasons that this thesis can be accomplished is that there is a team of zealous people who have shown their friendship and helped me through difficult times during my living and study in Japan, and among whom Mr. Yoshichika Hara, Mr. Koichi Kitamura and Ms. Eriko Takenaka should be specially mentioned for their friendship. It is they who have helped me overcome language problems and get used to the study as well as living here and together with the other Japanese friends my study and stay in KUT has become a pleasant and memorable experience. Therefore, here I sincerely extend my gratitude to this group of people.

Finally, my special thanks will go to my wife and parents for their love, understanding and support. It is

they who are always behind me to sweeten my life when I feel tired and make me feel stronger in face of difficulties, and genuinely grateful for all that they've done for me, I take it as my mission to love and protect them for the rest of my life.

Table of Contents

List of Figures

List of Tables

List of Symbols and Abbreviations

A	Complex Amplitude
A_r, A_i	Real and Imaginary Part of Complex Amplitude
B	Bandwidth
B_{DN}	N-look Sub-Doppler Bandwidth
B_R	Signal Bandwidth of Chirp Pulse
D_A	Antenna Length
$\vec{E}_x$, $\vec{E}_y$	x-Component and y-Component of Electromagnetic Wave Propagating Along z-Axis Direction in Cartesian Coordinate System
$\hat{E}_x$, $\hat{E}_y$	Complex Amplitude of $\vec{E}_x$ and $\vec{E}_y$
H	Horizontal Polarization
H	Polarimetric Scattering Entropy
H_t	Tree Height
I	Intensity
$J(\cdot)$	Jacobian
$K_{\nu-1}(\cdot)$	Modified Bessel Function of Order $\nu - 1$
$L(\cdot)$	Likelihood Function
L_A	Synthetic Aperture Length
$P(x)$	Probability of x
P_s, P_d, P_v	Power of Surface, Double-Bounce and Volume Scattering
R	Slant-Range Distance
R_0	Shortest Slant-Range Distance of Platform and Target
S	Complex Scattering Amplitude
S_0	Amplitude of Received Signal
T	Coherence Matrix
V	Vertical Polarization
V	Trunk Volume

V_{ar}	Variance of $\ln x$ in log-normal Distribution
a_ξ, a_η	Major and Minor Semi-Axes of the Ellipse
b, c	Scaling Parameter and Shape Parameter of Weibull Distribution
c	Light Speed
dB	Decibel
$\vec{e}_x$, $\vec{e}_y$	Unit Vector Parallel to x- and y-axis
f_0	Radar Carrier Frequency
f_s, f_d, f_v	Surface, Double-Bounce and Volume Scattering Contributions
h	Altitude of Platform
k	Wavenumber Equal to $2\pi/\lambda$
s_0	Amplitude of Transmitted Signal
s_r	Reference Signal
s_t	Transmitted Signal
t, t'	Time Variables in Azimuth Direction
v_a	Platform Travel Speed
x	Platform Position
$x^{(n)}$	nth Normalized Moment of $P(x)$
x, y, z	Cartesian Coordinate System
$\Gamma(\cdot)$	Gamma Function
ΔX	Azimuth Resolution
ΔX_N	Spatial Resolution of N-look Image in Azimuth Direction
ΔY	Ground-Range Resolution
Λ	Diagonal Eigenvalue Matrix of T
Ψ_B	*Borgeaud* Basis
Ψ_P	*Pauli* Basis
α	Frequency Modulation Rate
α_e	Auxiliary Angle of Polarization Ellipse
β	Doppler Constant
δ_0	Phase Difference Equal to δ_y-δ_x
δ_x, δ_y	Phase of $\vec{E}_x$ and $\vec{E}_y$
θ_i	Incidence Angle
θ_0	Off-nadir Angle
λ	Wavelength

λ_1, λ_2, λ_3	Eigenvalues of Coherence Matrix
μ	Mean of $\ln x$ in log-normal Distribution
ν	Order Parameter of Gamma and K-distribution
σ	Radar Cross Section
σ^2	Variance
τ	Time Variable in Range Direction
τ_A	Aperture Synthesis Time or Integration Time
τ_n	Center Time of Look n in Multilook Processing
τ_p	Transmit Pulse Duration
ϕ	Phase of Complex Amplitude
χ	Ellipticity Angle
ψ_e	Inclination Angle of Polarization Ellipse
ω_c	Centre Radian Frequency
$<>$	Ensemble Average
$\langle x^n \rangle$	nth Moment of $P(x)$
ACF	Autocorrelation Function
AIC	Akaike Information Criterion
CCF	Cross-Correlation Function
DBH	Diameter at Breast Height
EM	Electromagnetic
FFT	Fast Fourier Transform
FM	Frequency Modulation
GBH	Girth at Breast Height
HH	Transmit Horizontal, Receive Horizontal Polarization
HV	Transmit Horizontal, Receive Vertical Polarization
IRF	Impulse Response Function
LSM	Least Square Method
MLE	Maximum Likelihood Method
MNLT	Memoryless Nonlinear Transformation
MOM	Moment Method
PDF	Probability Density Function
PRF	Pulse Repetition Frequency
PSF	Pint Spread Function

RAR	Real Aperture Radar
RCS	Radar Cross Section
SAR	Synthetic Aperture Radar
VH	Transmit Vertical, Receive Horizontal Polarization
VV	Transmit Vertical, Receive Vertical Polarization

Chapter 1

Introduction

1.1 Speckle and its Origin

When a fairly coherent beam of electromagnetic wave is either reflected from a randomly rough surface or propagates through a medium that changes the phase of the incident wave randomly, a random intensity distribution called "speckle" may be produced. This phenomenon was first observed in the field of optics by Exner in 1877, who found a radially granular pattern within the bright central Fraunhofer ring [1]. In the field of radar, the speckle or better known as "clutter" has been one of the major issues since the radar was first used for ship detection. It should be noted at this stage that the term "speckle" is generally used in the field of optics, while in the field of radar and acoustics, the random fluctuation in the signals, which we call speckle in optics, is traditionally called "clutter" [2]. Both the terms describe the same physical phenomenon, and in the present thesis, we use both the terms of "SAR speckle" and "SAR clutter" where appropriate.

During the World War II, tremendous effort was made to develop radar and image analysis for obvious military applications. The main purpose of early radar systems was target detection, and the work at the time was concerned mainly on noise reduction [2]. The utilization of SAR speckle in information extraction as well as speckle suppression started when the first spaceborne SAR was launched on board of the oceanographic satellite SEASAT in 1978. After SEASAT Shuttle-borne SARs and several spaceborne SARs were launched, and high-resolution airborne SARs were also developed by several countries. Accordingly, the study on Gaussian and non-Gaussian speckle has become one of the major subjects in the SAR community.

Thus, in the field of optics, the basic work and applications of speckle began since the early 1960s when the laser was invented and became commercially available [3], [4], but it was early 1980s when the research on SAR speckle started, and it is still in a developing stage.

Fig.1.1 shows a laser speckle pattern, illustrating granular and noise-like random fluctuations. Since speckle appears random, the best way to describe its property in quantitative manner is to use statistical description.

Figure 1.1: Far-field speckle pattern (courtesy of Prof. Kazuo Ouchi, Kochi University of Technology).

The origin of speckle is interference of coherent electromagnetic waves associated with the random nature of scattering objects. If a coherent wave is incident on a random rough surface, the phases of the scattered wave are proportional to the surface undulation. Therefore, if a surface is rough compared to the wavelength of the incident wave, the phases of the scattered wave are randomly distributed in the 0-2π interval. When these scattered waves from many scattering elements are combined at an image plane as in Fig.1.2, the complex amplitude in a single image pixel is a coherent sum of many contributions from independent scattering elements with random phases, and consequently a granular random speckle pattern is produced.

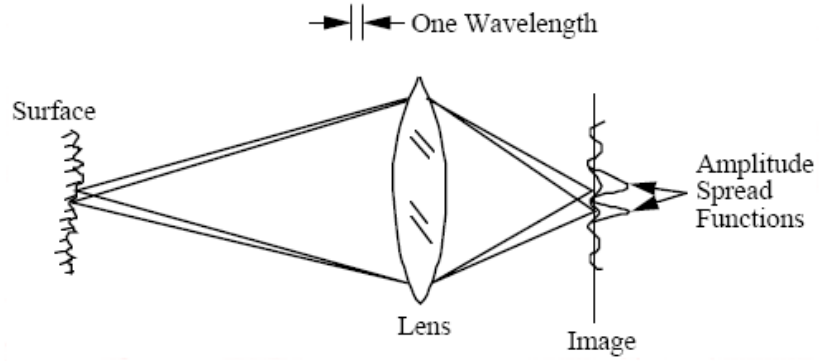

Figure 1.2: Physical origin of speckle for an imaging system.

Fig.1.3 illustrates the process of speckle formation in a simple manner. When an imaging system of finite resolution is used to form the image of a rough surface, there may be many scatterers in one resolution cell, and the value of each pixel in the image plane is the result of interference among many contributions within

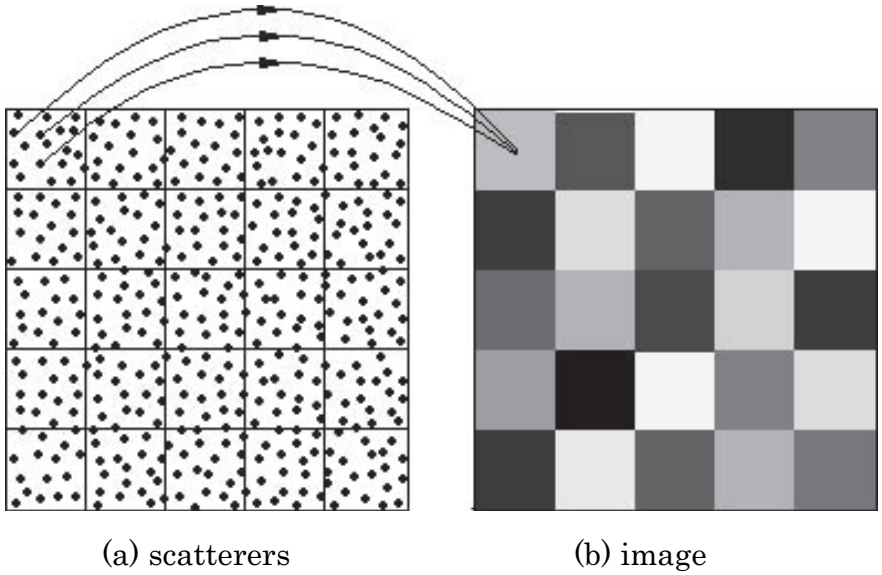

Figure 1.3: Speckle formation. The value of an image pixel (assume one pixel=one resolution cell) is determined by the coherent sum of contributions from randomly distributed scatterers in a resolution cell on the surface.

the corresponding resolution cell, where "many" implies more than 5-8 scatterers to satisfy the central limit theorem [5], [6]. The value of the pixel next to it is also a coherent sum of scattering elements in the neighbouring resolution cell. However, these scattering elements are not correlated with those in other resolution cells, and therefore the pixel values are statistically uncorrelated with each other. As a result, the image of a rough surface becomes a speckle pattern consisting of random and statistically independent pixel values.

1.1.1 Gaussian SAR Speckle

Fig.1.4 is an example of SAR speckle. The formation of speckle in SAR systems is the same as that described with reference to Fig.1.3 where the lens is replace by a SAR imaging system. The image in Fig.1.4 is formed by the C-band (wavelength 5.7 cm, frequency 5.3 GHz) SAR on board of the Canadian satellite RADARSAT-1. Fig.1.4(a) shows a speckle pattern in the image of a homogeneous field. The dark horizontal linear feature on the left hand side of Fig.1.4(b) is an airport runway, the white semi-vertical line at the center is a breakwater, and the quasi-periodic image on the right corresponds to ocean waves. The illuminating (range of cross-track) direction is from right to left, and the azimuth (along-track) direction is from top to bottom. The concrete break water gives strong backscatter and appears very bright because it is aligned almost orthogonal to the illuminating direction. The surface of the airport runway is smooth giving little backscatter, and appears dark in the image. These features are embedded in speckle, and because of this

speckle noise it is difficult to extract information from this image, for example, to segment the runway, or to measure the dominant wavelength of the ocean waves.

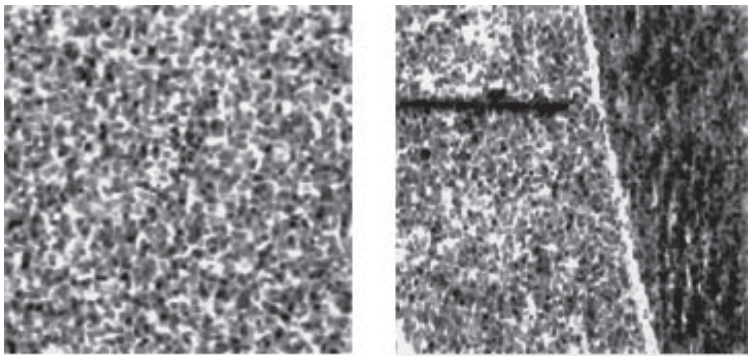

(a) (b)
(copyright CSA/RSI)

Figure 1.4: RADARSAT-1 SAR images of (a) a homogeneous area and (b) features embedded in speckle.

The homogeneous fluctuation in Fig.1.4(a) is closely approximated as Gaussian speckle. Gaussian speckle itself does not carry information on the scattering surface except that there are many randomly distributed scatterers within a resolution cell. However, if two slightly displaced Gaussian speckle patterns are formed on a same image plane and re-radiated by a coherent beam, they yield an interference pattern. The technique is known as "speckle interferometry", and it is the basis of techniques such as the measurement of objects' displacement and distortion [7], stellar speckle interferometry [8], and SAR interferometry [9], [10]. Other applications include measurement of surface roughness [11], information processing [12], and of course, speckle reduction [13]-[15].

1.1.2 Non-Gaussian SAR Speckle

Fig.1.5 is a X-band airborne Pi-SAR image of the Tottori dune. The dark area marked "A" is the sand dune and the area "B" is water. There is little radar backscatter from these areas because the surface is smooth. The area marked "C" is lawn on a golf course. Despite the difference in image intensity, the images appear random and statistically uniform, corresponding to Gaussian speckle.

The areas marked "D", "E" and "F" are forests. It can be seen that these images are different from the homogeneous images of sand, water and lawn, as they have certain structures or "texture". This type of image fluctuation is called non-Gaussian speckle or clutter. The statistical properties of non-Gaussian speckle contain information on the scattering objects because the texture is different among different forests. This observation has lead the author to investigate the statistics of Gaussian and non-Gaussian speckle in

SAR images, and their possible applications to information extraction described in this thesis.

For the description of non-Gaussian statistics, the textbooks by Oliver and Quegan [16], and Sekine and Mao [17] provide excellent statistical treatments to extract information from non-Gaussian SAR speckle, speckle suppression, image segmentation and classification.

Figure 1.5: X-band Pi-SAR image of the Tottori dune (courtesy of NICT).

1.2 Outline of Thesis

The outline of this thesis is illustrated in Fig.1.6. In Chapter 1, speckle phenomenon, its origin, applications to SAR systems and the objectives of this research are introduced. In Chapter 2, statistical properties of speckle patterns are described, where Gaussian and non-Gaussian speckles are introduced and explained in detail using simulated images. Chapter 3 presents the SAR system, including the processes through which the point spread function (PSF) also known as the impulse response function (IRF) is produced from SAR raw data, multilook processing, SAR imaging process of extended objects. Chapter 4 presents SAR polarimetry, including the results of alpha-entropy analysis over Pi-SAR Tomakomai forests and 3-component decomposition analysis of Pi-SAR Kojima rice field and Tomakomai forests. The Chapter 5 and

6 present applications of SAR speckle to forestry and oceanography respectively. Finally, the conclusions of this research are given in Chapter 7. In the following, brief summaries of chapters are presented.

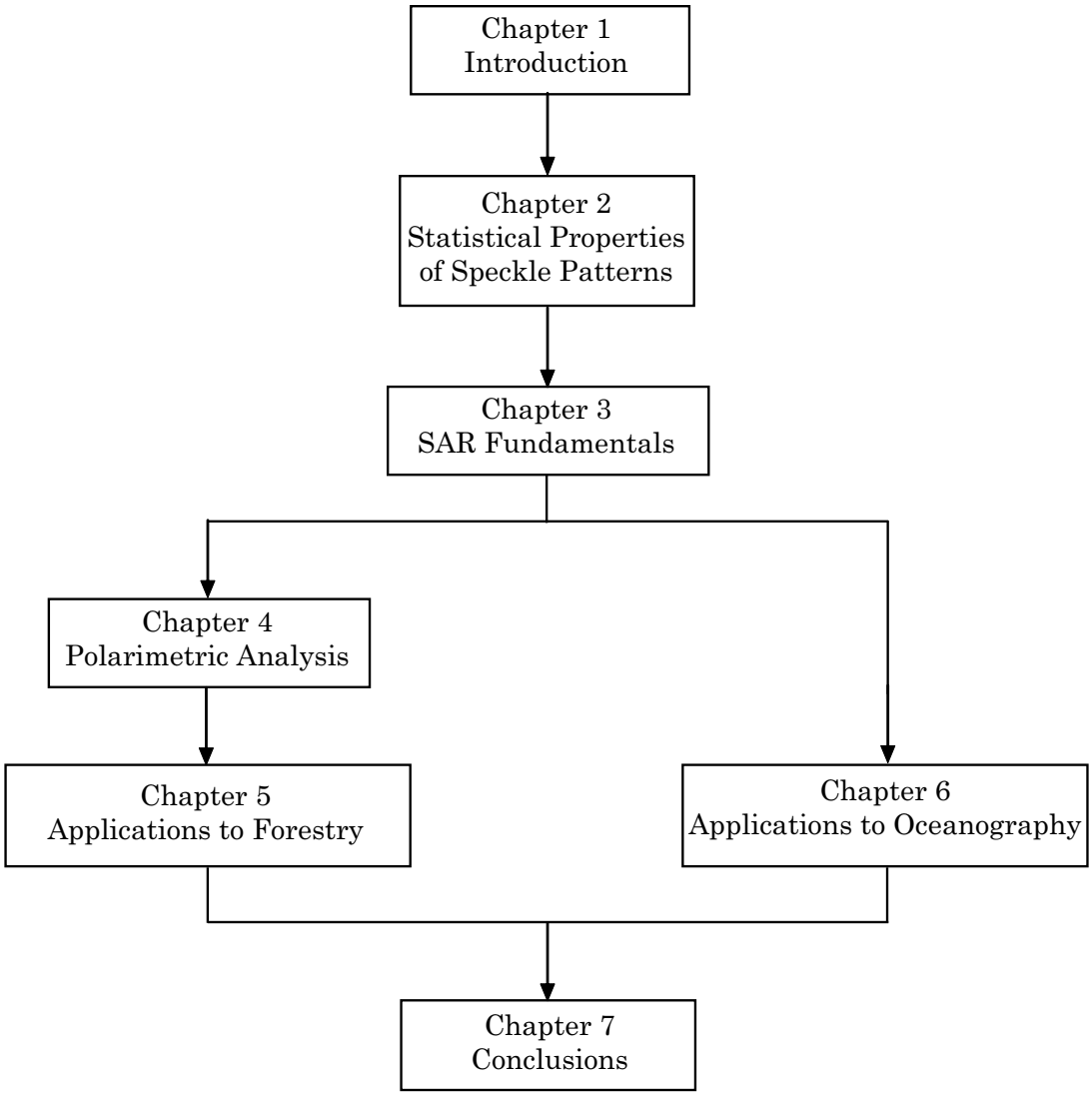

Figure 1.6: Structure of thesis.

1.3 Brief Summary of Each Chapter

1.3.1 Speckle Statistics

In Chapter 2, statistical analysis [5], [6] is used to describe the properties of speckle. Random roughness of a surface and/or randomly distributed scatterers can cause random amplitudes and/or random phases in the scattered complex wave which enters into the image plane. Therefore, this process can be considered as

a "random walk" in the complex plane, and the resultant image complex amplitude is the sum of all the steps. The result of the summation depends on the relative phases of each step and their amplitudes.

Since the phases vary randomly by more than 2π, they are uniformly distributed in the range of $(0, 2\pi]$. If the number of contributions is large enough, the summation of all the contributions leads to the image amplitude to follow the Rayleigh distribution, and the intensity (the module square of amplitude) obeys the negative exponential distribution. This type of speckle is called Gaussian speckle. However, if the number of contributions is not large enough or the mean number follows some distributions, the speckle will be non-Gaussian distributed.

Non-Gaussian speckle also arises from the summation of many contributions of random phases but the amplitude varies in a order of or greater than the resolution scale. The non-Gaussian behaviour of forested areas in Fig.1.5, for example, there may be many backscattered waves within a resolution cell, even if the resolution cell is small (1.5 $\times$1.5m). Their phases are uniformly distributed, but the amplitude variation of individual trees is larger than the resolution cell. The textural appearance of this amplitude variation yields non-Gaussian behaviour of the forest images seen in Fig.1.5.

Detailed descriptions of the random walk problem, PDFs of speckle phase and amplitude is presented in the first part of Chapter 2. The amplitude PDF of non-Gaussian speckle can be described by several statistical models, including the log-normal, Weibull, gamma and K-distribution models, and these PDFs and their moments are described with simulated data [18]-[28]. To estimate the statistical parameters of these PDFs, three frequently used approaches are introduced, including the maximum likelihood method, least square method and moment method [5], [6], [16].

1.4 SAR Systems

In this thesis, the study mainly focuses on speckle in SAR systems, and therefore it is important to understand the principle of SAR imaging process, which is presented in Chapter 3. For a SAR system, its antenna transmits coherent electromagnetic (EM) wave and receives the backscattered echoes from the targets on the Earth. Each pixel of SAR image may be the result of the summation of the backscattering of many scattering elements. Thus, the SAR speckle can also be described by the general theories given in Chapter 2 [16], [29]-[33].

The SAR imaging process is different from that of the conventional imaging radars. A conventional radar is also called the "real aperture radar (RAR)" of which the resolution is determined by the pulse length in the range direction and by the illuminating beam width in the azimuth direction. Much finer spatial

resolution is achieved by SAR by "matched filtering". The processes of forming a point image (PSF) and extended objects by this matched filtering technique are described, followed by multilook processing which can be used for speckle reduction as well as information extraction.

1.4.1 Polarimetric Analysis

Chapter 4 is concerned with SAR polarimetry. With rapid advance of SAR systems, resolution of spaceborne SARs is increased, and most of modern airborne SARs can operate at multiple frequencies and at full polarimetric mode. The information content is increased dramatically, and new techniques rather than using just amplitude or intensity data of a single polarization. Polarimetry is an emerging technique to quantify the scattering process (for example, surface scattering, double-bounce and volume scattering) and to improve the accuracy of image segmentation and classification [34]-[37]. SAR polarimetry is not the main theme of this thesis, but it is used to support to understanding the scattering mechanisms. For this reason, polarimetric analysis is presented for the Pi-SAR images of the Okayama rice fields (typical example of low vegetation) in Japan, and the Tomakomai forests in Hokkaido, Japan.

1.4.2 Forest Information Extraction from Non-Gaussian SAR Speckles

Chapter 5 and 6 are the applications of SAR speckle to forestry and oceanography respectively. SAR data have been widely used in forestry study [38]-[58]. There are 1/3 of lands are covered by forests, and the forests play an important role in carbon dioxide absorption, producing wood and influencing climate. Radar data can be used to monitor forests, detect deforestation and estimate forest biomass.

Using speckle models to estimate the properties of unknown scenes from SAR data is an effective means of extracting information. The scene characteristics can be related to the model parameters. In Chapter 5, the relations between non-Gaussian distributed high-resolution polarimetric SAR images and forest parameters are investigated.

There are substantial members of literatures relating forest parameters, in particular biomass, with radar cross section (RCS). However, RCS is known to saturate with increasing biomass, and the saturation levels vary with different radar parameters and forest species. Dobson et al [44] claimed the saturation limits of 100 tons/ha and 200 tons/ha for L-band and P-band respectively for the AIRSAR data of coniferous forests at 40°-50° incidence angles. While Imhoff [48] stated that the saturation levels are 20 tons/ha, 40 tons/ha and 100 tons/ha for C-, L- and P-band AIRSAR data of mixed forests at 40°-50° incidence angles.

The data we used in this study are Pi-SAR [59] polarimetric data of the Tomakomai forests [60] in Hokkaido, Japan. X- and L-band data with all polarizations are available. Moreover, the ground truth data

collected in 2002, 2003 and 2005 are available, which include tree height, diameter at breast height (DBH), age, biomass and soil moisture. The RCS is estimated as a function of tree biomass estimated in 2002 and 2003, and the results show that at X-band, the RCS is largest for VV-polarization followed by HH- and HV-polarizations; while at L-band it is largest for HH-polarization followed by VV- and HV-polarizations. There are no clear biomass saturation levels at X-band, but the L-band saturation level may be defined approximately as 40 tons/ha for our datasets [54]. This technique of estimating forest biomass from the RCS is well known [43]-[49].

The next step is to search a statistical model that fits best to the forest images, and to find a best statistical parameter which relates the forest parameter(s). As a result, the K-distribution is found to fit best, and the order parameter of the K-distribution has a highest correlation with the forest biomass. The regression curve is then derived to quantify the order parameter as a function of the forest biomass measured in 2003 and 2004. The accuracy of this empirical model is investigated by comparing the biomass predicted by the model and the biomass measured during the summer of 2005, yielding the model accuracy of approximately 85%. This empirical model can be used to estimate the coniferous forest on a fairly flat ground in Hokkaido, Japan. Applicabilities to forests on sloped grounds, forests of mixed species and broadleaf trees and to forests not in Hokkaido are not known, and remain as the subjects of future studies. It should be emphasized that there are some reports that suggest the utilization of non-Gaussian texture in retrieving forest parameters from SAR data [57], [58]. However, there is no work reporting the quantitative relation between the parameters of non-Gaussian SAR images and forest parameters, except the relation of RCS.

1.4.3 Speckle Reduction in SAR Images of Sea Surface

In Chapter 6, multilook processing for dynamic sea surfaces with partially overlapped sub-apertures is investigated. Applications of SAR data to oceanography are very popular topics [61]-[76], since 2/3 of our planet is covered by ocean that plays an important role in the global climate and ecosystem. Since the first spaceborne SAR, SEASAT-SAR, was launched in 1978, SAR data have been used to develop sea monitoring systems. SAR data can be used to estimate ocean wave parameters, such as direction and wavelength. It can also be used to study internal waves and detect oil slicks. Further, ship detection is also an important issue [75].

Speckle makes it difficult to detect edges, objects of small sizes, and objects that have small RCS. To reduce the speckle in SAR image, multilook processing is frequently used. In the previous study [75], a new ship detection algorithm based on multilook processing was proposed. In this technique, ships "invisible" to radar can be detected by calculating the cross-correlation function between the sub-images. Since the

deterministic ships' images are correlated and the random images (speckle) of sea surface are uncorrelated, the CCF of ships' images has larger correlation values than those of uncorrelated speckle sub-images. The sub-apertures used in this study are non-overlapping to each other. However, a theory was proposed that if the scene coherence time shorter than the sub-aperture integration time were to enter the speckle cross-correlation, then a partially overlapped extra look can be obtained, where speckle patterns in all looks are uncorrelated to each other [71]. If this were true, then an extra look can be used for further reduction of speckle, and to improve the accuracy of ship detection. To check this assumption, a theory is developed, and the cross-correlation functions are computed using the JERS-1 [77] and RADARSAT-1 [78] images over the coastal areas of Japan. The result shows that, as predicted by the theory, the CCF of speckle between sub-images processed with partially overlapped sub-apertures is independent of the coherence (decorrelation) time of the sea surface caused by the random motion of small-scale waves [76].

1.5 Publication List

The followings are the publications based the research carried out under this project.

Refereed Papers:

- H.Wang, K.Ouchi, M.Watanabe, M.Shimada, T.Tadono, A.Rosenqvist, S.A.Romshoo, M.Matsuoka, T.Moriyama, and S.Uratsuka, "In Search of the Statistical Properties of High-Resolution Polarimetric SAR Data for the Measurements of Forest Biomass beyond the RCS Saturation Limits," *IEEE Trans. Geosci. Remote Sens. Lett.*, (to be published in October issue, 2006).

- K.Ouchi, H.Wang, N.Ishitsuka, G.Saito, and K.Mohri, "On the Bragg Scattering Observed in L-band Synthetic Aperture Radar Images of Flooded Rice Fields," *IEICE Trans. Commun.*, vol.E89-B, no.8, pp.2218-2225, 2006.

- K.Ouchi and H.Wang, "Interlook cross-correlation function of speckle in SAR images of sea surface processed with partially overlapped subapertures," *IEEE Trans, Geosci. Remote Sens.*, vol.43, pp.695-701, Apr. 2005.

Conference Proceedings:

- H.Wang, K.Ouchi, M.Watanabe and M.Shimada, "Biomass Estimation Algorithm of Coniferous Forests Based on Statistical Texture Analysis Approach of High-Resolution Polarimetric SAR Data and Its Evalution," *Proc. PIERS, Tokyo, Japan*, Aug. 2006.

- H.Wang, K.Ouchi, N.Ishitsuka, G.Saito and K.Mohri, "Analysis of Bragg Scattering Phenomenon Observed in L-band SAR Images of Machine-Planted Rice Paddies," *Proc. PIERS, Tokyo, Japan*, Aug. 2006.

- H.Wang, K.Ouchi, M.Watanabe and M.Shimada, "On the Accuracy of the Empirical Model for Estimating Forest Biomass from *K*-Distributed SAR Image," *IEICE Tech.. Rep., SANE2006-57 (2006-05), Kochi, Japan*, pp.1-6, May, 2006.

- K.Ouchi, H.Wang, N.Ishitsuka, G.Saito and K.Mohri, "Analysis of the Bragg Resonance Scattering in L-band JERS-1 SAR and Pi-SAR Images of Rice Paddies," *Proc. WSANE 2006 (Workshop for Space, Aeronautical and Navigational Electronics), Xi'an, China*, *IEICE Tech.. Rep., SANE2006-20*, vol. 106, no. 1, pp.103-108, Apr., 2006.

- H.Wang, K.Ouchi, M.Watanabe and M.Shimada, "On the Accuracy of Empirical Relation Between Forest Biomass and Order Parameter of K-Distribution in Pi-SAR Images," *Proc. WSANE 2006 (Workshop for Space, Aeronautical and Navigational Electronics), Xi'an, China*, *IEICE Tech.. Rep., SANE2006-21*, vol. 106, no. 1, pp.109-114, Apr., 2006.

- H.Wang, K.Ouchi, M.Watanabe and M.Shimada, "Biomass Estimation Algorithm of Coniferous Forests Using Empirical Relation Between K-distribution in High-Resolution polarimetric SAR Images and Forest Biomass," *Proc. SANE 2006 General Conf., Tokyo, Japan*, Mar. 2006.

- H.Wang, K.Ouchi and M.Watanabe, "Evaluating the Biomass Estimation Algorithm of Coniferous Forests Based on Statistical Texture Analysis Approach of High-resolution Polarimetric SAR Data," *Proc. SAR Workshop 2006, Sendai, Japan*, Jan. 2006.

- H.Wang, K.Ouchi, M.Watanabe, M.Shimada, T.Tadono, A.Rosenqvist, S.A.Romshoo, M.Matsuoka, T.Moriyama, and S.Uratsuka, "The dependence of forest biomass on the order parameter of K-distribution of high-resolution airborne polarimetric SAR images of forests," *Proc. PIERS, Hangzhou, China*, Aug. 2005.

- H.Wang and K.Ouchi, "A study on the relation between ocean surface coherence time and speckle cross-correlation in multilook SAR images produced by partially overlapped subapertures," *Proc. PIERS, Hangzhou, China*, Aug. 2005.

- H.Wang and K.Ouchi, "The Relation Between the Order Parameter of K-Distribution in High-Resolution Polarimetric SAR Data and Forest Biomass," *Proc. IGARSS, Soul, Korea*, Jul. 2005 (DVD).

- H.Wang and K.Ouchi, "Speckle Cross-Correlation in Multilook SAR Images of Dynamic Sea Surface Processed with Partially Overlapped Sub-Reference Signals," *Proc. IGARSS, Soul, Korea*, Jul. 2005 (DVD).

- H.Wang and K.Ouchi, "A study on the invalidation case of partially overlapped multilook processing of the SAR data of sea surface for uncorrelated speckle patterns," *IEICE Tech.. Rep., SANE2005-11 (2005-05), Kochi, Japan*, pp.21-25, May, 2005.

- H.Wang, K.Ouchi, M.Watanabe, M.Shimada, T.Tadono, A.Rosenqvist, S.A.Romshoo, M.Matsuoka, T.Moriyama, and S.Uratsuka, "Estimating tree biomass using the empirical relations between high-resolution polarimetric SAR data and forest parameters," *IEICE Tech.. Rep., SANE2005-12 (2005-05), Kochi, Japan*, pp.27-31, May, 2005.

- K.Ouchi and H.Wang, M.Watanabe, M.Shimada, T.Tadono, A.Rosenqvist, S.A.Romshoo, M.Matsuoka, and S.Uratsuka, "On the Forest Biomass and the Order Parameter of K-Distribution in High-Resolution Airborne Polarimetric SAR Data" *Proc. WSANE 2005 (Workshop for Space, Aeronautical and Navigational Electronics), Daejeon, Korea*, pp.5-10, Mar., 2005.

- K.Ouchi and H.Wang, "On the Cross-Correlation of Speckle Patterns in Multilook SAR Images of Dynamic Sea Surfaces" *Proc. WSANE 2005 (Workshop for Space, Aeronautical and Navigational Electronics), Daejeon, Korea*, pp.11-16, Mar., 2005.

- H.Wang and K.Ouchi, "Relation between the sea surface coherence time and the speckle cross-correlation function in multilook SAR images: theory and validation using JERS-1 L-band and RADARSAT C-band SAR data" *Proc. SAR Workshop 2005, JAXA, Tokyo, Japan*, Jan., 2005 (CD-ROM).

- H.Wang, K.Ouchi, M.Watanabe, M.Shimada, T.Tadono, A.Rosenqvist, S.A.Romshoo, M.Matsuoka, and S.Uratsuka, "Texture analysis of high-resolution Pi-SAR polarimetric images of forests based on non-Gaussian statistics," *Proc. SAR Workshop 2005, JAXA, Tokyo, Japan*, Jan., 2005 (CD-ROM).

- H.Wang, K.Ouchi, M.Watanabe, M.Shimada, T.Tadono, A.Rosenqvist, S.A.Romshoo, M.Matsuoka, and S.Uratsuka, "On the quantitative relation between tree parameters and Pi-SAR polarimetric data over the Tomakomai forests: preliminary results," *Proc. 37th Japanese Conf. Remote Sens., Hitachi, Japan*, pp.61-64, Dec., 2004.

- H.Wang and K.Ouchi, "Derivation of cross-correlation function of SAR speckle processed with partially overlapped sub-apertures and validation using ocean data," *Proc. 36th Japanese Conf. Remote Sens., Chiba, Japan*, pp.15-18, May, 2004.

Chapter 2

Statistical Properties of Speckle Patterns

As mentioned in the previous chapter, speckle plays an important role in many fields where scattering of coherent electromagnetic wave is involved. Before proceeding to the utilization of speckle, it is necessary to understand the fundamental statistical properties of speckle patterns. In this chapter, both Gaussian and non-Gaussian statistics are introduced, and the corresponding speckle patterns are simulated. We mainly focus on first-order statistical properties of speckle amplitude, such as the PDF, variance and moments. Here, the term "first-order" means the statistical properties at a single point in space or for time-varying speckle in the space-time domain. The term "second-order" implies the statistical properties at two points, autocorrelation function (ACF), for example. It is known that the second-order statistics contain more information on scattering objects [16], but to extract information, large areas of same statistics are required as compared with the first-order statistics. The measurement accuracy may be questioned for small areas such as the Tomakomai forests. However, it is an interesting future work to investigate the applicability of the second-order statistics to the Tomakomai Pi-SAR data. The second-order statistics of Gaussian speckle are discussed in Appendix A. The non-Gaussian statistical models introduced in this chapter are the log-normal, Weibull, gamma, and K-distribution, and the latter three distributions can be used to describe both amplitude and intensity speckle, while log-normal distribution is often used to fit amplitude images with strong spatial variation, such as urban areas.

Due to the fact that the physical origin and statistical properties of speckle is are essentially the same in any fields where speckle phenomena occur, the theories described in this chapter can be applied to any of these fields, including SAR.

2.1 Statistics of Gaussian Speckle

The complex speckle images contain both amplitude and phase information, and each pixel can be represented by the complex number $|A|e^{i\phi}$, where A is the amplitude and ϕ is the phase. *Speckle* has noise-like appearance as such it can either be treated as noise or source of information in interferometry. Three assumptions have

to be made for speckle formation. The first is that scatterers in each resolution cell are randomly distributed, the second is that the phase ϕ_k and amplitude A_k of the scattered wave are independent to each other, and the third is that the number of these scatterers satisfies *central limit theorem* [5]. That is, one pixel consists of many random contributions from independent scatterers. For example, these conditions are satisfied when a laser beam of light illuminates a rough surface, and radio wave of a finite width illuminates a terrain or sea surface.

2.1.1 Random Walk

Because the incident beam interacts with randomly distributed scatterers, the scattered field in space and time is also random in amplitude and phase. Then this process can be described by the random walk in a complex plane, which is shown in Fig.2.1, and the resultant vector sum can be given by the following summation [3]

$$A = |A|e^{i\phi} = \frac{1}{\sqrt{N}} \sum_{k=1}^{N} |A_k| e^{i\phi_k} \tag{2.1}$$

where N is the number of phasor components in the random walk, that is, the total number of scatterers falling in a single pixel in the SAR image. $|A_k|/\sqrt{N}$ and ϕ_k are the amplitude and phase of the scattered wave from the kth scatterer, or they can be considered as the length and direction of step k. Because the scatterers are randomly distributed, the amplitude $|A_k|/\sqrt{N}$ is also random, and phase ϕ_k is uniformly distributed in [-π, π).

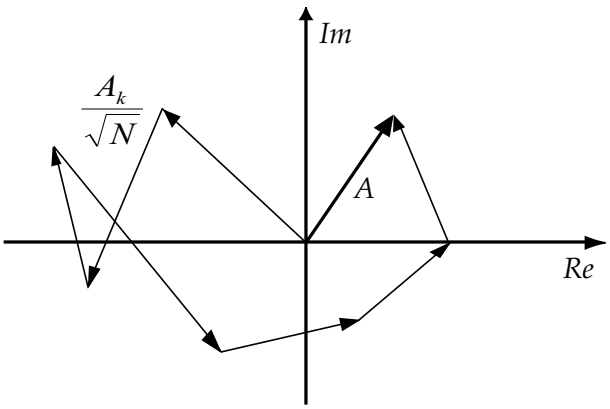

Figure 2.1: Random walk in the complex plane.

2.1.2 First-Order Amplitude Distribution

Let A_r and A_i denote the real and imaginary part of the complex amplitude respectively. Their ensemble averages can then be given by

$$\begin{aligned}\langle A_r \rangle &= \frac{1}{\sqrt{N}} \sum_{k=1}^{N} \langle |A_k| \rangle \langle \cos \phi_k \rangle = 0 \\ \langle A_i \rangle &= \frac{1}{\sqrt{N}} \sum_{k=1}^{N} \langle |A_k| \rangle \langle \sin \phi_k \rangle = 0 \end{aligned} \tag{2.2}$$

respectively. Because the phase ϕ_k is uniformly distributed over the interval [-π, π), the ensemble averages of *sine* and *cosine* are equal to 0. In a similar way, we can also get

$$\left\langle A_r^2 \right\rangle = \frac{1}{N} \sum_{k=1}^{N} \sum_{k'=1}^{N} \langle |A_k||A_{k'}| \rangle \langle \cos \phi_k \cos \phi_{k'} \rangle \tag{2.3}$$

The phases of different scatterers are independent to each other, so that $\langle \cos \phi_k \cos \phi'_k \rangle = 0$ when $k \neq k'$. Then, for the real part,

$$\begin{aligned}\left\langle A_r^2 \right\rangle &= \frac{1}{N} \sum_{k=1}^{N} \left\langle |A_k|^2 \right\rangle \left\langle \cos^2 \phi_k \right\rangle \\ &= \frac{1}{N} \sum_{k=1}^{N} \left\langle |A_k|^2 \right\rangle \frac{1}{2} \langle \cos 2\phi_k + 1 \rangle \\ &= \frac{1}{2N} \sum_{k=1}^{N} \left\langle |A_k|^2 \right\rangle \end{aligned} \tag{2.4}$$

and for the imaginary part,

$$\begin{aligned}\left\langle A_i^2 \right\rangle &= \frac{1}{N} \sum_{k=1}^{N} \sum_{k'=1}^{N} \langle |A_k||A_{k'}| \rangle \langle \sin \phi_k \sin \phi_{k'} \rangle \\ &= \frac{1}{2N} \sum_{k=1}^{N} \left\langle |A_k|^2 \right\rangle \end{aligned} \tag{2.5}$$

The correlation function of real and imaginary part is

$$\begin{aligned}\langle A_r A_i \rangle &= \frac{1}{N} \sum_{k=1}^{N} \sum_{k'=1}^{N} \left\langle |A_k|^2 \right\rangle \langle \cos \phi_k \sin \phi_{k'} \rangle \\ &= 0 \end{aligned} \tag{2.6}$$

Since the central limit theorem is satisfied, A_r and A_i become asymptotically Gaussian as $N \to \infty$. The PDF of the real and imaginary parts can be given by [3]

$$p\left(A_r, A_i\right) = \frac{1}{2\pi\sigma^2} \exp\left(-\frac{A_r^2 + A_i^2}{2\sigma^2}\right) \tag{2.7}$$

where

$$\sigma^2 = \lim_{N\to\infty} \frac{1}{N} \sum_{k=1}^{N} \frac{\left\langle A_k^2 \right\rangle}{2} \tag{2.8}$$

The speckle following this PDF is called Gaussian speckle. As mentioned before, for low resolution imaging data, the images of random rough surfaces tend to have the statistics of Gaussian speckle.

2.1.3 Phase and Intensity Distributions

In this subsection, we will derive the PDFs of the speckle phase and intensity. The intensity and phase are given by

$$I = A_r^2 + A_i^2 \tag{2.9}$$

$$\phi = \arctan\left(A_i / A_r\right) \tag{2.10}$$

respectively. Their joint PDF can be expressed by transformation (2.7)

$$p\left(A_r, A_i\right) = p\left(I, \phi\right) J\left(\frac{I, \phi}{A_r, A_i}\right) \tag{2.11}$$

where J is the Jacobian of the transformation, which is defined by [5]

$$J\left(\frac{I, \phi}{A_r, A_i}\right) = \begin{vmatrix} \partial I/\partial A_r & \partial I/\partial A_i \\ \partial \phi/\partial A_r & \partial \phi/\partial A_i \end{vmatrix} \tag{2.12}$$

In orthogonal coordinate, the relations

$$\begin{aligned} A_r &= \sqrt{I}\cos\phi \\ A_i &= \sqrt{I}\sin\phi \end{aligned} \tag{2.13}$$

are satisfied. By substituting (2.7) in (2.11), we get

$$p\left(I,\phi\right)=\frac{1}{4\pi\sigma^{2}}\exp\left(-\frac{I}{2\sigma^{2}}\right)\mathrm{rect}\left(\frac{\phi}{2\pi}\right)\quad:\quad I\geq0 \tag{2.14}$$

The marginal density function of the phase is deduced from

$$\begin{aligned}p\left(\phi\right)&=\int_{0}^{\infty}p\left(I,\phi\right)dI\\&=\frac{1}{2\pi}\mathrm{rect}\left(\frac{\phi}{2\pi}\right)\end{aligned} \tag{2.15}$$

Similarly, the marginal density function of the intensity is given by

$$\begin{aligned}p\left(I\right)&=\int_{0}^{2\pi}p\left(I,\phi\right)d\phi\\&=\frac{1}{2\sigma^{2}}\exp\left(-\frac{I}{2\sigma^{2}}\right)\end{aligned} \tag{2.16}$$

The nth moment of speckle intensity is defined as

$$\begin{aligned}\left\langle I^{n}\right\rangle&=\int_{0}^{\infty}I^{n}p\left(I\right)dI\\&=n!\left(2\sigma^{2}\right)^{n}\end{aligned} \tag{2.17}$$

Then the variance can be deduced as

$$\begin{aligned}\sigma_{I}^{2}&=\left\langle I^{2}\right\rangle-\left\langle I\right\rangle^{2}\\&=2\left(2\sigma^{2}\right)^{2}-\left(2\sigma^{2}\right)^{2}\\&=\left\langle I\right\rangle^{2}\end{aligned} \tag{2.18}$$

As can be seen from equation (2.18), the standard deviation σ_I of speckle intensity is equal to the mean intensity.

Substituting equation (2.17) with $n=1$ in (2.16), we can get

$$p\left(I\right)=\frac{1}{\left\langle I\right\rangle}\exp\left(-\frac{I}{\left\langle I\right\rangle}\right) \tag{2.19}$$

By changing intensity into amplitude,

$$p\left(|A|\right) = \frac{2|A|}{\langle |A|^2 \rangle} \exp\left(-\frac{|A|^2}{\langle |A|^2 \rangle}\right) \tag{2.20}$$

Equation (2.20) is known as the Rayleigh distribution.

2.1.4 Simulation of Gaussian Speckle

To develop and test algorithms, simulation can be a useful technique, in which the parameters can be changed as we wish. Gaussian speckle is simulated in this subsection.

There are several ways to simulate Gaussian distributed clutter, including, for example, Monte Carlo method [5], or analytically solving some distributions by calculating the inverse function. Furthermore, the Rayleigh and negative exponential distributions can be formed based on the random walk [3]. In this study, the "random walk" approach is used.

Fig.2.2 shows simulation results. In (b) and (c), the amplitude and intensity are normalized by the mean intensity. As can be seen, the distributions of the simulated data are in good agreement with the theoretical values.

2.1.5 Limitations of Gaussian Distribution

Gaussian speckle is formed based on the assumption that there exist more than 5-8 randomly distributed scatterers in a resolution cell. In real situations, however, the number of scatterers N may be small because of very fine spatial resolution of the imaging system. A small number of scatterers within a resolution cell lead to speckle images which do not obey Gaussian statistics. Non-Gaussian speckle may also be formed by many scatterers, but the amplitudes are correlated, varying slowly within a resolution cell. In order to describe such non-Gaussian fluctuations, various statistical models are introduced, and 4 frequently used models are introduced in the following section.

2.2 Statistics of Non-Gaussian Speckle

The non-Gaussian distributions of interest are the log-normal, gamma, Weibull and K-distribution. These distribution functions are often used in the fields of optics, acoustics and radars. With rapid advance of the radar technology, the spatial resolution is increased considerably. The most of airborne SARs today have resolution of order of or smaller than a meter or two, and they can distinguish the structures of scattering

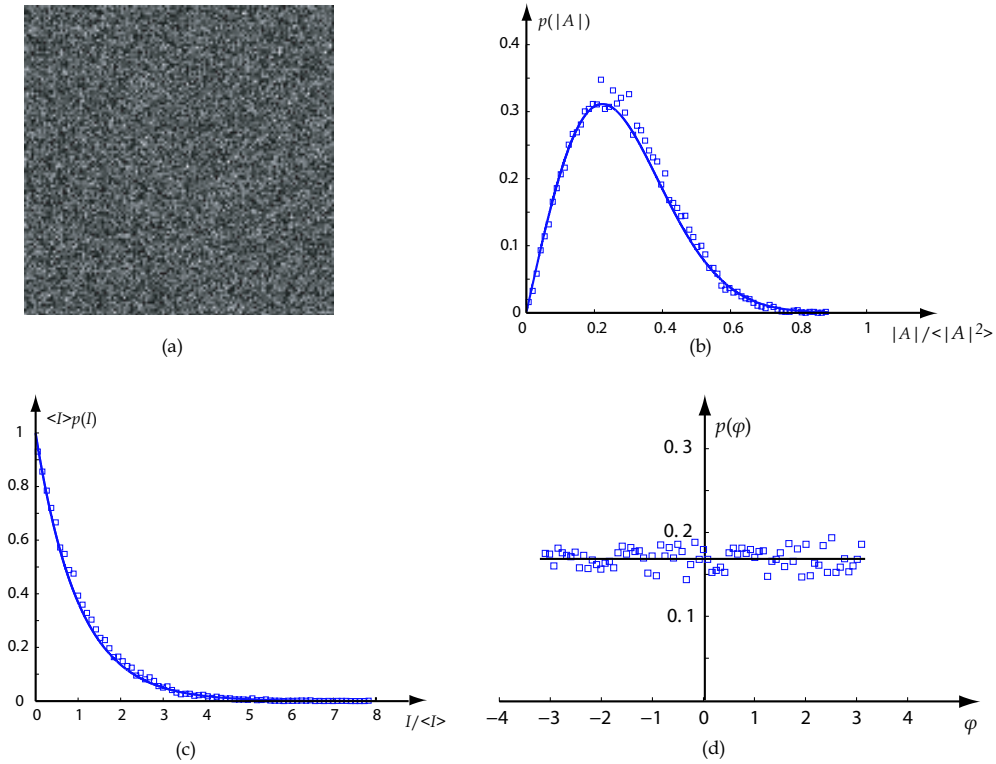

Figure 2.2: Simulated Gaussian speckle and its distributions; (a) is the speckle amplitude image; (b) shows the amplitude distribution and Rayleigh distribution; (c) shows the intensity distribution and negative exponential distribution; (d) shows the phase distribution and the uniform distribution. In (b), (c) and (d), the squares denote the simulated data, while the theoretical distributions are shown by the solid curves.

objects. These structures appear as "texture" in SAR images. To describe these non-Gaussian texture, it is, of course, better to used statistical models of multiple parameters instead of a single parameter. On the other hand, models of a single parameter is attractive for its simplicity. The log-normal and Weibull are the distributions with two parameters that have been widely applied, for example, to land clutter of built up areas and sea clutter [17], [20], [79].

The log-normal distribution is defined by

$$P(x) = \frac{1}{x\sqrt{2\pi V_{ar}}} \exp\left[-\frac{(\ln x - \mu)^2}{2V_{ar}}\right] \tag{2.21}$$

where x is a generic observable, and μ and V_{ar} are the mean and variance of $\ln x$. The expected value and nth normalized moment of log-normal distribution are given respectively by

$$\langle x \rangle = \exp\left[\mu + \frac{V_{ar}}{2}\right]$$
$$x^{(n)} = \frac{\langle x^n \rangle}{\langle x \rangle^n}$$

$$= \exp\left[n(n-1)\frac{V_{ar}}{2}\right] \tag{2.22}$$

The disadvantage of log-normal distribution is that it always has a poor performance to describe intensity clutter, although it is often used to represent areas with strong spatial variation.

The Weibull distribution is given by

$$P(x) = \frac{cx^{c-1}}{b^c}\exp\left[-\left(\frac{x}{b}\right)^c\right] \tag{2.23}$$

where b is a scaling parameter, and c is the shape parameter. The mean and nth normalized moment of this distribution are

$$\begin{aligned}\langle x\rangle &= b\Gamma\left(1+\frac{1}{c}\right)\\ x^{(n)} &= \frac{\Gamma\left(1+n/c\right)}{\Gamma^n\left(1+1/c\right)}\end{aligned} \tag{2.24}$$

when $c = 1$ and $c = 2$, the Weibull distribution becomes identical to a negative exponential and a Rayleigh PDF respectively. Fig.2.3 shows the Weibull distribution for several different shape parameters.

For radar images, the following product model can be used.

$$I = \sigma n \tag{2.25}$$

where I is the observed intensity, σ is the underlying RCS, and n is multiplicative noise. The RCS and noise are statistically independent to each other. For intensity image, the PDF of the noise contribution n is

$$P(n) = \exp\left(-n\right) \tag{2.26}$$

In the previous studies on speckle over sea surface, Ward [19] found that the backscatter from swells of a large spatial scale followed the gamma distribution given by

$$P(\sigma) = \left(\frac{\nu}{\langle\sigma\rangle}\right)^{\nu}\frac{\sigma^{\nu-1}}{\Gamma(\nu)}\exp\left[-\frac{\nu\sigma}{\langle\sigma\rangle}\right] \tag{2.27}$$

where ν is order parameter, and the moments are given by

$$\langle\sigma^n\rangle = \left(\frac{\langle\sigma\rangle}{\nu}\right)^n\frac{\Gamma(n+\nu)}{\Gamma(\nu)} \tag{2.28}$$

By combing the noise PDF with the gamma PDF, the PDF of the resultant image intensity is given by [16]

$$\begin{aligned} P(I) &= \int_0^\infty P(I \mid \sigma) P(\sigma) d\sigma \\ &= \frac{2}{\Gamma(\nu)} \left(\frac{\nu}{\langle I \rangle} \right)^{(1+\nu)/2} \times I^{(\nu-1)/2} K_{\nu-1} \left[2 \left(\frac{\nu I}{\langle I \rangle} \right)^{1/2} \right] \end{aligned} \tag{2.29}$$

where $K_{\nu-1}[\cdot]$ is the modified Bessel function of order $\nu - 1$. The normalized nth moments are given by

$$\frac{\langle I^n \rangle}{\langle I \rangle^n} = \Gamma(1+n) \frac{\Gamma(\nu+n)}{\nu^n \Gamma(\nu)} \tag{2.30}$$

It can be seen that the normalized variance is $\langle I^2 \rangle / \langle I \rangle^2 = 1 + 2/\nu$. The order parameter ν which fits best to data can be estimated by using this relation.

From the relation $A = \sqrt{I}$, the amplitude PDF can be derived, which also follows the K-distribution given by

$$\begin{aligned} P(A) &= \int_0^\infty P(A|\sigma) P(\sigma) d\sigma \\ &= \frac{4}{\Gamma(\nu)} \left(\frac{\nu}{\langle I \rangle} \right)^{(1+\nu)/2} \times A^\nu K_{\nu-1} \left[2A \left(\frac{\nu}{\langle I \rangle} \right)^{1/2} \right] \end{aligned} \tag{2.31}$$

and the moments are:

$$\langle A^n \rangle = \langle I \rangle^{n/2} \Gamma(1 + n/2) \frac{\Gamma(\nu + n/2)}{\nu^{n/2} \Gamma(\nu)} \tag{2.32}$$

The normalized amplitude variance can be deduced from equation (2.32) when $n = 2$.

K-distribution can also be deduced from another view aspect: assuming that the number of scatterers in each resolution cell is a variable which follows Poisson distribution; Further, considering the "expected number of scatterers" as a variable which obeys gamma distribution, the image is then K-distributed [26]. Moreover, as discussed in previous section, if the number of scatterers in each resolution cell is large enough and approximately constant, the image is then Gaussian distributed.

2.2.1 Simulations of Non-Gaussian Speckle

There are many open literatures describing the simulation of non-Gaussian clutter, such as the memoryless nonlinear transformation (MNLT) method which provided an easy way by mapping the Gaussian distribution into non-Gaussian PDFs and then solving the equation numerically [80]. Moreover, Davidson [81] provided

an excellent work in simulating non-Gaussian clutter. Oliver [16] used a method of convolving a gamma-distributed clutter with a band-limited function (PSF for example) to produce a K-distributed clutter. Blacknell [82] presented an approach of using moving average filters to uncorrelated gamma clutter to produce a correlated K-distributed clutter.

The simulation results are given in Fig.2.3-Fig.2.5. Because the PDF of simulated data and the theoretical curves cannot be identified, only the true parameters and estimated parameters are given in each figure.

2.3 Parameter Estimation

Parameter estimation plays a very important role in model fitting, and there are three frequently used methods: maximum likelihood method (MLE), least square method (LSM), and moment method (MOM) to estimate the parameters of Weibull and K-distributions.

2.3.1 Maximum Likelihood

The method of maximum likelihood is a popular approach of probability analysis for parameter estimation. In this section, likelihood method is introduced first, and MLE is then described, followed by parameter estimation for the Weibull and K-distribution.

Likelihood Method

In the likelihood method, given a parameter vector θ, while $x = (x_1, x_2, ..., x_n)$ denotes data set, the likelihood function of θ is the same function as the joint probability distribution $p(x, \theta)$ of x and θ. That is to say, we can write the joint density as [25]

$$L = \prod_{i=1}^{n} p_{x_i}(x_i, \theta) \tag{2.33}$$

With x fixed to the data set and $p(x, \theta)$ is a function of θ, then $p(x, \theta)$ can be called the likelihood function of θ. Usually, likelihood function is denoted as $L(\theta) = p(x, \theta)$. In fact, $L(\theta)$ is also a function of x, because x is the samples from the measurements.

When

$$L(\theta_1) > L(\theta_2) \tag{2.34}$$

We can say θ_1 is better estimation then θ_2, because it has a larger probability for certain x.

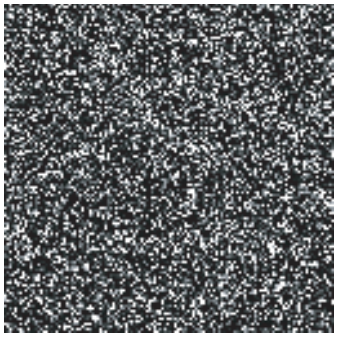

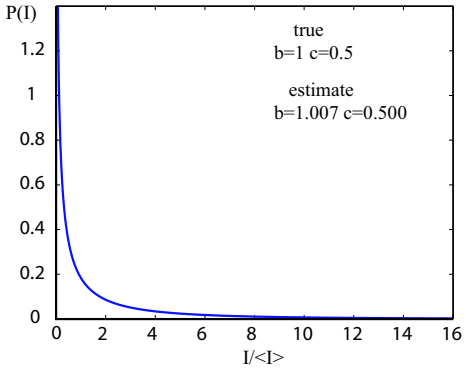

(a)

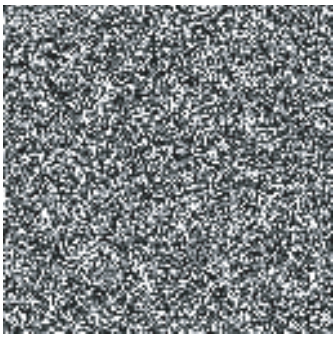

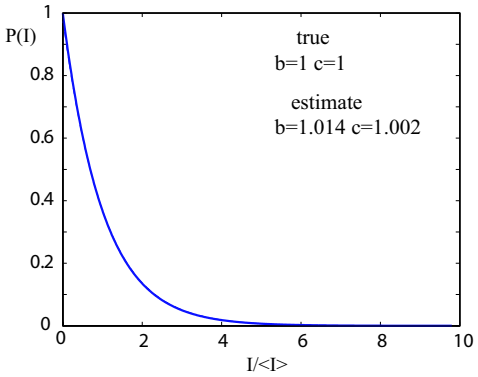

(b)

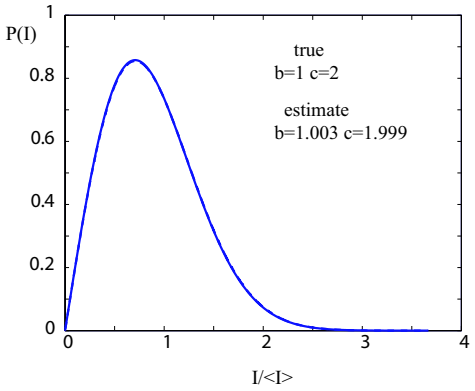

(c)

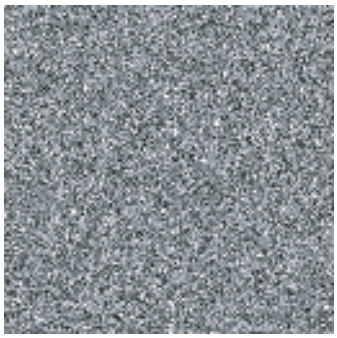

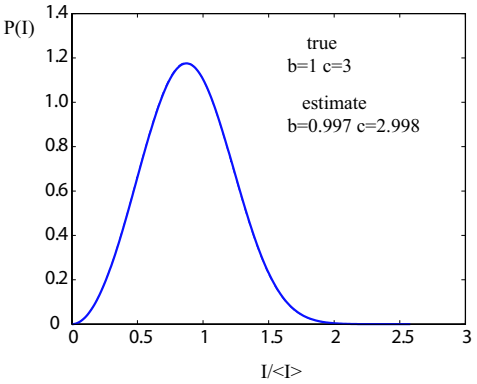

(d)

Figure 2.3: Simulated Weibull distributed clutter and PDF with different parameters.

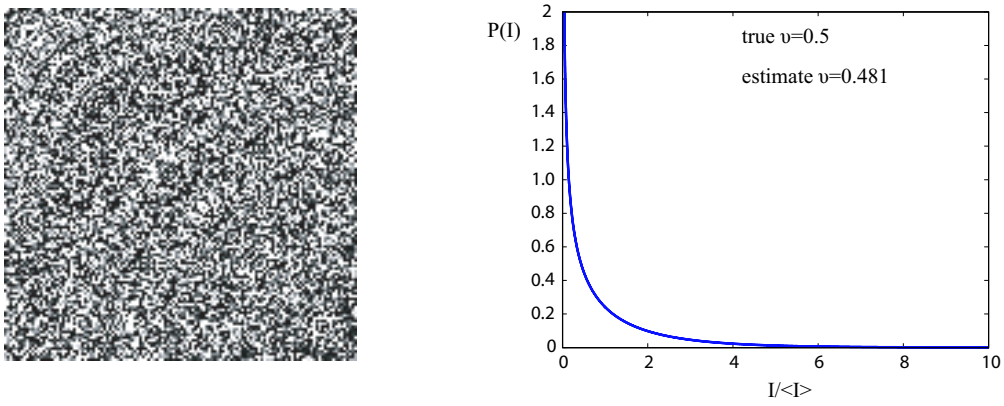

(a)

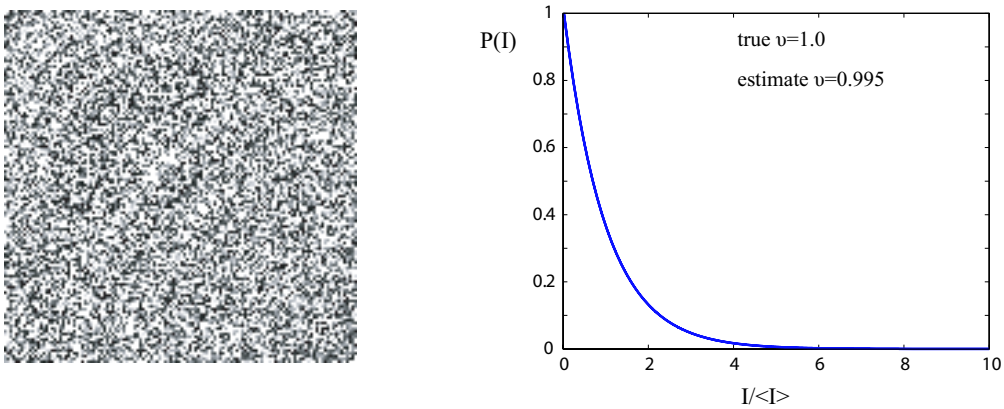

(b)

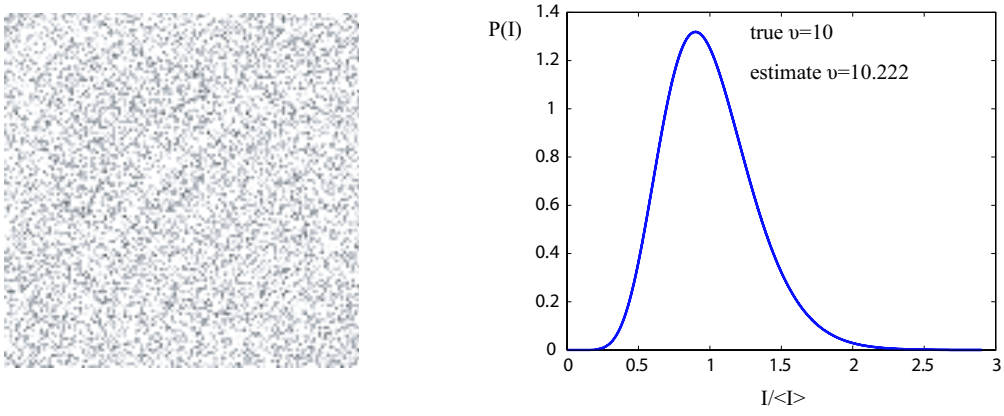

(c)

Figure 2.4: Simulated gamma distributed clutter and PDF with different parameters.

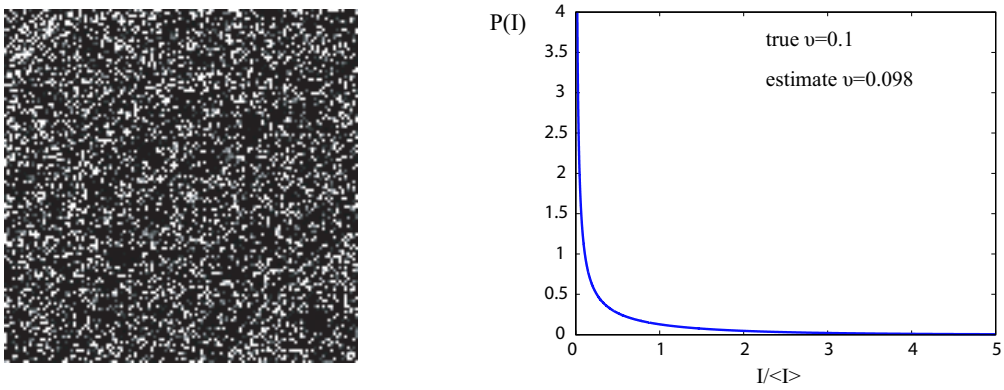

(a)

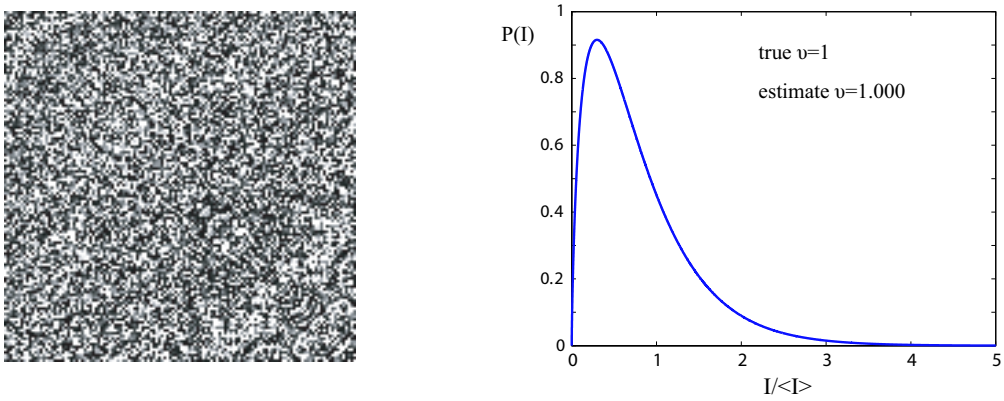

(b)

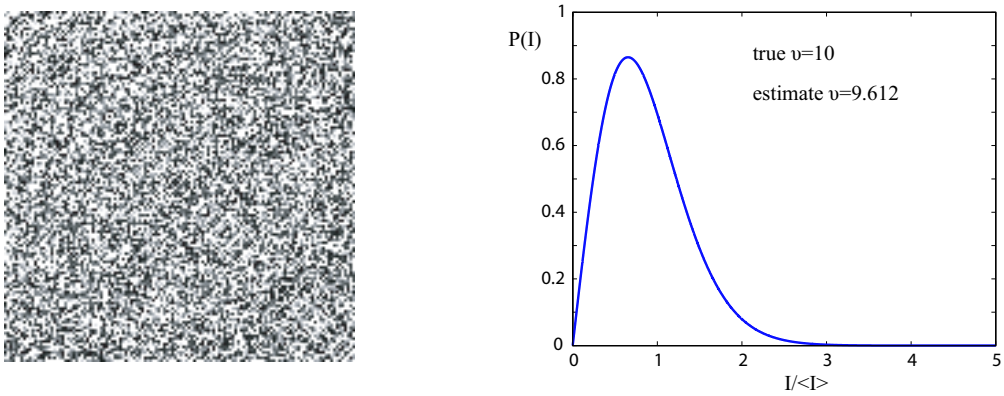

(c)

Figure 2.5: Simulated K-distributed clutter and PDF with different parameters.

Maximum Likelihood

We say $\hat{\theta}$ is a maximum likelihood estimate of $\theta \in \Theta$, if:

$$L(\hat{\theta}) = \max_{\theta \in \Theta} L(\theta) \tag{2.35}$$

That is to say, MLE is given by maximizing the likelihood function. To get a MLE parameter, for one parameter case, we can differentiate the likelihood equation, that is,

$$\frac{d}{d\theta} L(\theta) = 0 \tag{2.36}$$

and also for multi-parameter case,

$$\begin{aligned} \frac{\partial \ln L}{\partial \theta_1} &= 0 \\ \frac{\partial \ln L}{\partial \theta_2} &= 0 \\ &\vdots \\ \frac{\partial \ln L}{\partial \theta_n} &= 0 \end{aligned} \tag{2.37}$$

As given in equation (2.37), for multi-parameter equation, to simplify the operation, logarithm of the equation is used to take partial differentiation.

MLE for Weibull and *K*-Distribution

Consider the Weibull PDF given in equation (2.23). The likelihood function is [83]

$$L(x_1, \ldots, x_n; c, b) = \prod_{i=1}^{n} \frac{c}{b} \left(\frac{x_i}{b}\right)^{c-1} \exp\left(-\left(\frac{x_i}{b}\right)^{c}\right) \tag{2.38}$$

On taking the logarithms of equation (2.38), differentiating with respect to b and c in turn and equating to zero, the estimating equations can be obtained as

$$\frac{\partial \ln L}{\partial c} = \frac{n}{c} + \sum_{i=1}^{n} \ln x_i - \frac{1}{b} \sum_{i=1}^{n} x_i^b \ln x_i = 0 \tag{2.39}$$

$$\frac{\partial \ln L}{\partial b} = -\frac{n}{b} + \frac{1}{b^2} \sum_{i=1}^{n} x_i^b = 0 \tag{2.40}$$

By combining above equation (2.39) and (2.40) and eliminating b, we get

$$\frac{\sum_{i=1}^{n} x_i^c \ln x_i}{\sum_{i=1}^{n} x_i^c} - \frac{1}{c} - \frac{1}{n}\sum_{i=1}^{n} \ln x_i = 0 \tag{2.41}$$

To solve this equation, Newton-Raphson method is used. Once c is determined, b can be estimated using by the following equation.

$$b = \frac{\sum_{i=1}^{n} x_i^c}{n} \tag{2.42}$$

The PDF of K-distribution is given by equation (2.31), by taking the logarithm of the PDF, we can get [25]

$$\ln L = -n \ln \Gamma(\nu) + n \left(\frac{\nu+1}{2}\right) \ln \left(\frac{\nu}{\langle I \rangle}\right) + \nu \sum_{i=1}^{n} \ln A_i + \sum_{i=1}^{n} \ln K_{\nu-1} \left[2A_i \left(\frac{\nu}{\langle I \rangle}\right)^{1/2}\right] \tag{2.43}$$

It is difficult to calculate the differentiation of the modified Bessel function, so that a different approach is adopted. In this approach, the value of ν is changed step by step within one large range, and hence the largest value of equation (2.43) can be easily obtained. Although this algorithm has low computing efficiency, it is simple and works well.

Introduction of Newton-Raphson Method

Given a complicated equation $y = f(x)$, it is generally difficult to finding the root using normal methods such as solving the equation. However, we can use a discrete method known as the Newton-Raphson. In this method, the value of x is given by the previous known value of x subtracted by the function itself normalized by its derivative as follows.

$$x_{n+1} = x_n - \frac{f(x_n)}{f' x_n} \tag{2.44}$$

where, x_n is the current known x value, $f(x_n)$ denotes the value of the function at x_n, and $f'(x_n)$ is the derivative at x_n, while x_{n+1} represents the next x value that you are trying to find. To end this loop, you have to set a certain condition, for example $x_{n+1} - x_n \leq 0.001$.

2.3.2 Least Square

Least square method is a commonly used method in finding a regression curve to fit best to a given set of points by minimizing the sum of the squares of the offset of the points from the curve. The sum of the squares of the offsets is used instead of the offset absolute values because this allows the residuals to be treated as a continuous differentiable quantity. Here we only give the final result of this method for the Weibull distribution, since the detailed derivation can be found in any open literature.

$$\begin{aligned} c &= \frac{\left\{n \cdot \sum_{i=1}^{n} (\ln x_i) \cdot \left(\ln\left\{\ln\left[\frac{1}{1-\frac{i}{n+1}}\right]\right\}\right)\right\} - \left\{\sum_{i=1}^{n} \ln\left(\ln\left[\frac{1}{1-\frac{i}{n+1}}\right]\right) \cdot \sum_{i=1}^{n} \ln x_i\right\}}{\{n \cdot \sum_{i=1}^{n} (\ln x_i)^2\} - \{\sum_{i=1}^{n} (\ln x_i)\}^2} \\ b &= \exp\left(\overline{Y} - \overline{x}/c\right) \\ \overline{x} &= \frac{1}{n}\sum_{i=1}^{n} \ln\left[\ln\left(\frac{1}{1-\frac{i}{n+1}}\right)\right] \\ \overline{Y} &= \frac{1}{n}\sum_{i=1}^{n} \ln x_i \end{aligned} \tag{2.45}$$

where b and c are estimated scaling parameter and shape parameter of Weibull distribution, respectively. $\overline{x}$ and $\overline{Y}$ are used to simply the equation.

2.3.3 Moment Fit

The approach of moment is another technique commonly used in the field of parameter estimation. However, it requires a large sample number to obtain an accurate result. For a set of data $x_1, x_2, \ldots, x_n$, which obey the distribution given by $p(x)$, the nth moment can be given by [5]

$$\langle x^n \rangle = \int_0^\infty x^n p(x) dx \tag{2.46}$$

or, in a discrete form,

$$\langle x_k^n \rangle = \sum_0^\infty x_k^n P_n, \quad k = 1, 2, \ldots \tag{2.47}$$

If the sample number is large ($> 10^4$, for example), the moment approach is a good method to estimate the parameters of the Weibull and K-distributions. The results have been already given in equation (2.24) and equation (2.30) for the Weibull and K-distribution respectively.

2.4 Summary

Gaussian speckle is formed when a resolution cell of an imaging system contains many coherent contributions from randomly distributed scatterers. This process of speckle formation can be considered as a result of the random walk in the complex plan, that is, the resultant vector is the summation of many random steps which have random length (amplitude) and directions (phases). Due to the summation of random vectors, the phase of image complex amplitude is uniformly distributed in $[0, 2\pi)$. The amplitude of such Gaussian speckle is shown to obey the Rayleigh distribution, and the intensity and phase obey negative exponential and uniform distributions respectively. This Gaussian speckle is often seen in the images of uniformly distributed surfaces such as dense rainforests and flat grass fields produced by SAR systems of coarse resolution (order of or larger that 10 m).

With rapid advance of SAR technology in recent years, the resolving power of SAR has improved considerably, and the most of airborne SARs today have resolution capability in the order of or less than a few meters. Consequently, there appear occasions that a single pixel contains small number of scattering elements, and hence the clutter images no longer obey Gaussian statistics. To model such high-resolution SAR clutter, non-Gaussian PDFs are introduced. Among various non-Gaussian models, log-normal, Weibull, gamma and K-distributions are frequently used PDFs. The log-normal distribution has two parameters, mean and variance of the logarithm of image values. The Weibull distribution also has two parameters called the shape parameter and scattering parameter, and the Weibull distribution becomes identical to the negative exponential and Rayleigh PDFs when the shape parameter is equal to 1 and 2 respectively. Thus, the Weibull distribution is a versatile PDF and it has been widely used in the fields of optics, acoustics and radars. The K-distribution can be generated by the product of the gamma distributed speckle and the multiplicative noise. The K-distribution becomes the Rayleigh distribution when its order parameter increases to infinity.

Speckle simulation plays an important role in developing image process algorithm, filtering and image analyses. In this chapter, Gaussian and non-Gaussian speckle are simulated to illustrate their statistical properties. In order fit a model to actual image data, techniques of parameter estimation are discussed, including MLE, least square, and MOM methods.

Chapter 3

SAR Fundamentals

In order to apply the statistical properties of speckle to analysis of and information extraction from SAR images, SAR image forming processes are introduced in this chapter. SAR is an imaging radar which produces high-resolution two-dimensional radar images by synthesizing a large aperture in the azimuth (along-track) direction using a small antenna on board of an aircraft or satellite, and by using a pulse compression technique in the range direction [16], [29]-[33].

Attempts to acquire information on natural resources in the global scale from SAR data started since the launch of the civil SAR system, SESAT-SAR in 1978. Since then, abundance of experiments and research have been carried out and much progress has been made in the fundamental research, algorithm development, image analysis and applications to many fields of geoscience. Synthetic aperture processing is a very mature technique now, but extracting information from SAR data and true practical utilization for benefiting our society are still in developing stage.

In this chapter, radar system parameters are introduced first. Then the techniques of pulse compression and aperture synthesis used in SAR system to achieve high resolution are presented, followed by multilook processing. The image forming processes of a point target are extended to a convolution model to describe the images of extended scenes.

3.1 SAR System Parameters

SAR data are complex images produced from the return echoes interacted between microwave and targets, and as such they are dependent on the system parameters and target characteristics. To extract information from SAR data, the system parameters should be understood first. The common system parameters are described in the following subsections.

3.1.1 Geometry of SAR System

Fig.3.1 shows the basic geometry of a radar system [16], [29], [30]. A platform at an altitude h carries a side-looking radar antenna that illuminates the Earth's surface with pulses of electromagnetic radiation. The direction of platform traveling is known as the *azimuth* direction, and the *slant*-range direction is from the antenna pointing to the target, while *ground*-range direction is the slant-range direction projected on the Earth's surface. The parameter R_0 is the shortest distance from the radar to the target and it is precisely measured from the time interval between pulse transmission and reception. The minimum and maximum ranges are called *near*-range and *far*-range respectively. *Swath width* is the image width corresponding to the width from the near-range to far-range. The *incidence angle* θ_i is defined as the angle between the slant-range direction and a direction perpendicular to the Earth's surface from the platform. The incidence angle varies depending on the image position, and the generally quoted incidence angle (nominal incidence angle) is that at the center of the image swath. The incidence angle is an important parameter for its impact on the radar backscatter and geometrical effects.

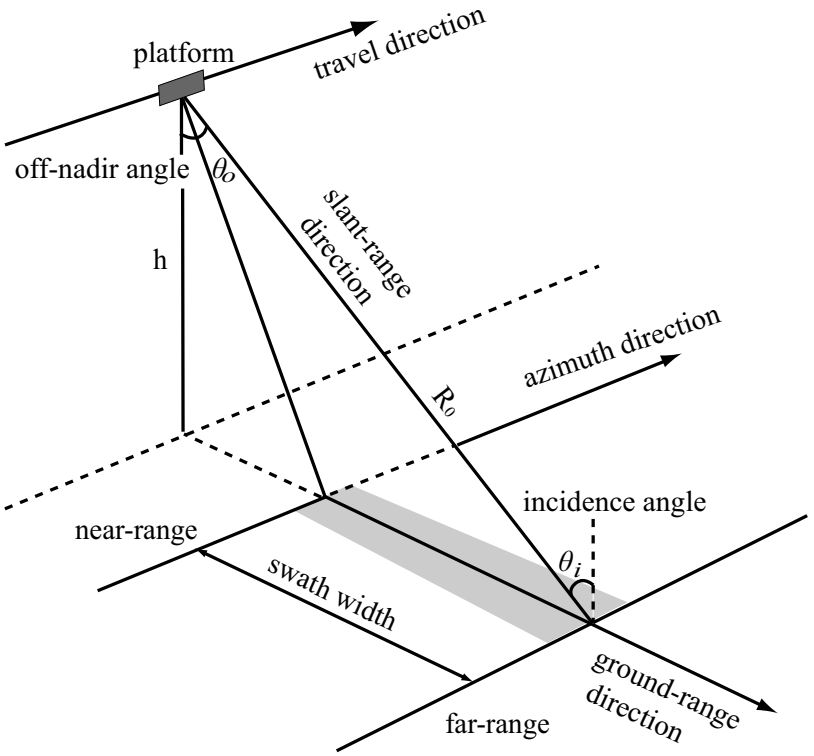

Figure 3.1: Illustration of SAR geometry.

3.1.2 Signal Parameters

There are three important parameters that describe radar transmitted pulses characteristics, and they are *pulse length* τ_p, *bandwidth* B and *pulse repetition frequency* (PRF) [16]. Since the pulse transmission and reception times cannot overlap, the swath width is restricted by the PRF as

$$\text{slant-range swath width} < \frac{c}{2 \times PRF} \tag{3.1}$$

must hold. The other important signal parameter is *wavelength* λ , which is related to the radar carrier frequency f_0 (in Hz) by

$$\lambda f_0 = c \tag{3.2}$$

where c is the speed of light.

Table 3.1 lists the radar bands and corresponding frequencies. Since the interaction between targets and microwave is dependent strongly on the wavelength, a suitable wavelength is selected for a given purpose. For example, longer wavelengths, such as L- or P-band are more useful to study forests than shorter X- and C-bands, because the radio wave of longer wavelengths can penetrate deeper in the forest interior, providing more information on the forests. Further, the surface roughness is, to a given wavelength, is "effective" roughness, that is, it is defined relative to the radar wavelength. For example, for a surface of average undulation of 5 cm is considered as "rough" for X-band microwave of wavelength 3 cm, while it is "smooth" for L-band microwave of wavelength 25 cm. Thus, a same surface may lead to different appearances in radar images.

Table 3.1: Common frequency bands for radar systems (modified from *radar handbook* [33]).

Radar band	Frequency - f_0	Used in ITU region 2
VHF	30∼ 300 MHz	138∼144 MHz 216∼225 MHz
UHF	300∼ 1000 MHz	420∼450 MHz 890∼942 MHz
L	1000∼ 2000 MHz	1215∼1400 MHz
S	2000∼ 4000 MHz	2300∼2500 MHz 2700∼3700 MHz
C	4000∼ 8000 MHz	5250∼5925 MHz
X	8000∼ 12000 MHz	8500∼10680 MHz
K_u	12∼ 18 GHz	13.4∼14.0 GHz 15.7∼17.7 GHz
K	18∼ 27 GHz	24.05∼24.25 GHz
K_a	27∼ 40 GHz	33.4∼36.0GHz

3.2 SAR Imaging of Point Target

3.2.1 Real Aperture Radar

The most imaging radars, including real aperture radars (RAR) and SAR, achieve high resolution in the range direction by using the pulse compression technique. Before the pulse compression technique was invented, conventional rectangular pulses without frequency modulation were used to produce radar images. In this section, the processes through which a point spread function (PSF) and resolution in the range direction are first described.

Consider a side-looking radar transmitting a square pulse of width τ_p toward a point scatterer "A" and "B" separated by a distance ΔY on the ground-range direction as shown in Fig.3.2. The images of the point scatterers, in principle, take the same rectangular form but with reduced amplitude. The image position is the time taken for the pulse to travel the two-way distance between the antenna and the scatterer, and it is given by $2R_A/c$ for the scatterer "A" and $2R_B/c$ for the scatterer "B", where R_A and R_B are the slant-range distances from the antenna to the scatterer "A" and "B" respectively, and "c" is the speed of light. If the two point images are separated by the time longer than the pulse width, they can be distinguished. If they overlap, then the two point scatterers cannot be resolved. The time resolution is defined as the time duration when the two point images are just separated. This time resolution is the pulse duration τ_p, and the ground-range spatial resolution can be deduced from the relation $2\Delta Y \sin\theta_i/c = \tau_p$, where θ_i is the incidence angle as illustrated in Fig.3.2. Thus, the spatial resolution in the ground-range direction is defined as

$$\Delta Y = \frac{c\tau_p}{2\sin\theta_i} \tag{3.3}$$

For example, a RAR with pulse duration $\tau_p = 0.1\,\mu$s operating at an incidence angle $\theta_i = 30°$ has the resolution $\Delta Y = 30$ m, and $\Delta Y = 3$ m with $\tau_p = 0.01\,\mu$s. For radars with square pulses, shorter the pulse duration is, finer the resolution becomes. The resolution also becomes coarse as the incidence angle decreases, and $\Delta Y \to \infty$ in the limit of $\theta_i \to 0$. This is the reason why the imaging radar is side-looking.

In the azimuth direction, the resolution is determined by the beam width. As shown in Fig.3.3, the signal from the scatterer "A" is just separated from the signal from "B" is when the two scatterers are separated by the distance over a half the azimuth beam width L_0. The azimuth resolution of real aperture radars is defined by

$$\Delta X = L_0/2 \tag{3.4}$$

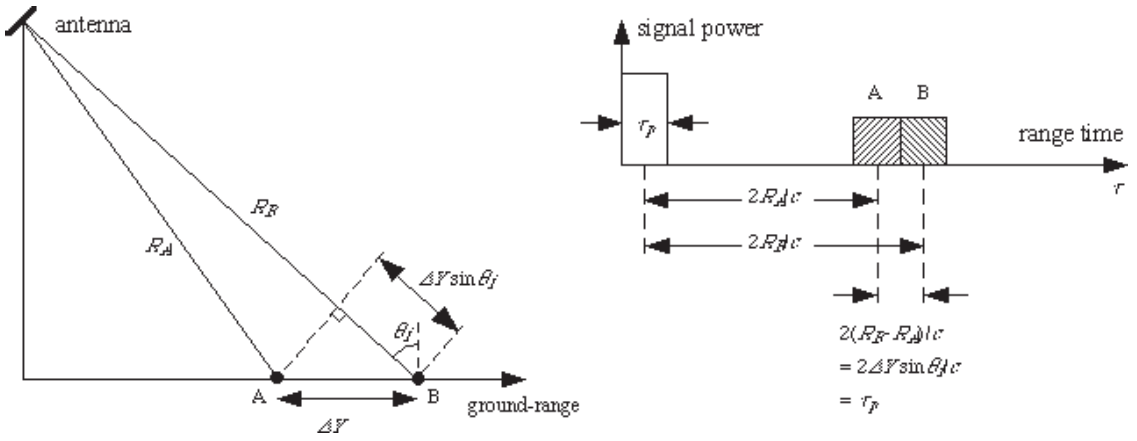

Figure 3.2: Illustrating range imaging process and resolution of a conventional radar with square pulses.

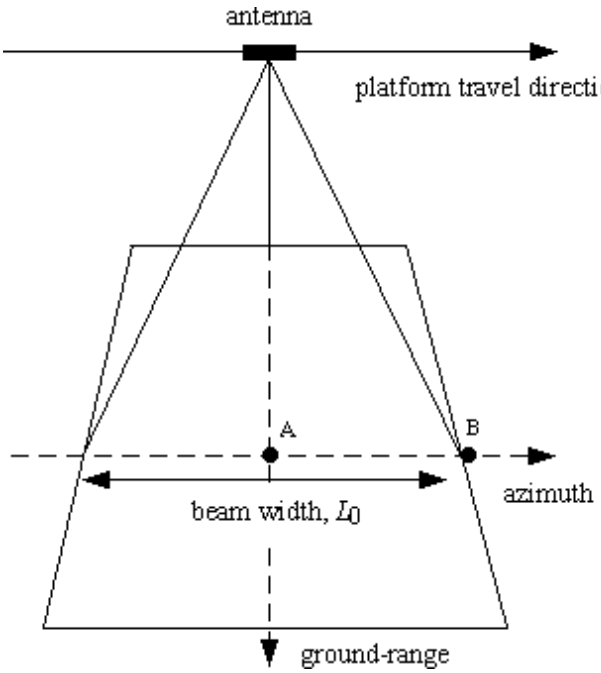

Figure 3.3: Illustrating azimuth resolution of a conventional radar.

For the JERS-1 SAR, the antenna length in azimuth is 12 m, wavelength $\lambda = 0.235$ m, the slant-range distance $R = 750$ km, the azimuth resolution becomes $\Delta X \simeq 15$ km if it is operated as a RAR.

Thus, for real aperture radars operating with square pulses, finer range resolution may be achieved by using pulses of shorter duration. For spaceborne systems, however, the available electric power is limited and it is difficult to transmit series of short pulses of high power to achieve desirable resolution. The overcome difficulty, a technique known as "pulse compression" [84] is used to obtain fine resolution. In this technique,

a sequence of frequency modulated (FM) or "chirp" pulses of long duration is used and the received signals are suitably processed to yield fine range resolution. The most of imaging radars today employ the pulse compression technique, including RAR and SAR.

In the azimuth direction, fairly fine resolution can be achieved for airborne radars by using a long antenna, but spaceborne radars such as JERS-1 SAR cannot be operated as RAR because of the limitation to the antenna size and hence very coarse resolution. In order to obtain fine azimuth resolution, the technique known as "aperture synthesis" [29] is adopted for the modern airborne and spaceborne radars. Indeed, the name "synthetic aperture radar" stems from this technique of synthesizing an imaginary large aperture using a small antenna. In the following, the techniques of pulse compression in the range direction and aperture synthesis in the azimuth direction are described in detail.

3.2.2 SAR Signal and Matched Filtering in Range Direction

In SAR systems, the transmitted microwave has the form [16], [29], [30]

$$s_t(\tau) = s_0 \exp(i\omega_c\tau + i\alpha\tau^2) \quad : \quad |\tau| \leq \tau_p/2 \tag{3.5}$$

where s_0 denotes the amplitude, ω_c denotes the centre radian frequency, α is the FM (chirp) rate, and τ is the time variable in the slant-range direction. Without a loss of generality, a complex expression is used in equation (3.5). In practice, the transmitted and received pulses are in a real form, but after pulse reception the real signal is transformed into a complex signal by filtering. It should be noted that in many fields of science and engineering, complex expressions are adopted and real component is taken from the final expression because of the mathematical complexity of using trigonometric functions. The instantaneous frequency can be derived from

$$\begin{aligned} f(\tau) &= \frac{1}{2\pi}\frac{d(\omega_c\tau + \alpha\tau^2)}{dt} \\ &= f_c + \frac{\alpha\tau}{\pi} \end{aligned} \tag{3.6}$$

and the signal bandwidth can be given as

$$B_R = |\alpha|\tau_p/\pi \tag{3.7}$$

The pulse given by equation (3.6) is known as FM pulse, and it is also referred to as chirp pulse. The frequency of this chirp pulse varies linearly in time with the gradient α/π. Fig.3.4 illustrates the FM pulse

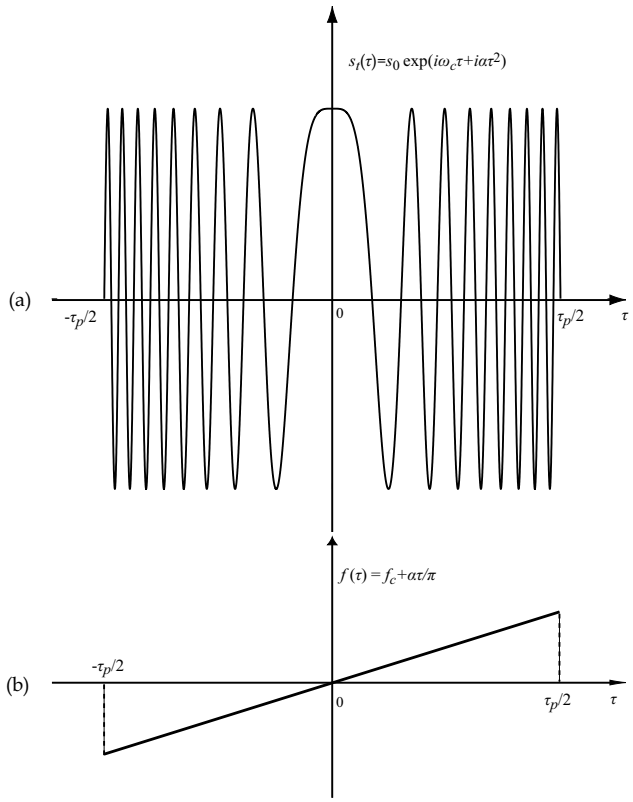

Figure 3.4: Illustrating (a) the real component of the phase of a FM pulse and (b) instantaneous frequency with $\omega_0 = 0$.

when the center frequency is 0 Hz.

The received signal from a point scatterer takes a same form as the transmitted signal but with reduced amplitude. The signal received from a point scatterer at the distance R_0 can be written as

$$\begin{aligned} s(\tau) &= S_0 s(\tau - 2R_0/c) \\ &= S_0 \text{rect}\left((\tau - 2R_0/c)/\tau_p\right) \exp\left(i\omega_c(\tau - 2R_0/c) + i\alpha(\tau - 2R_0/c)^2\right) \end{aligned} \tag{3.8}$$

where $2R_0/c$ is the two-way delay time, and

$$\begin{aligned} \text{rect}(\frac{\tau}{\tau_p}) = 1 \quad &: \quad \text{when} -\frac{\tau_p}{2} \leq t \leq \frac{\tau_p}{2} \\ 0 \quad &: \quad \text{otherwise} \end{aligned} \tag{3.9}$$

The term $\exp(-i\omega_c\tau)$ is mixed down to zero at the pre-processing stage, so that the received signal becomes

$$s(\tau) = S_0 s(\tau - 2R_0/c)$$

$$= \quad S_0 \text{rect}\left((\tau - 2R_0)/\tau_p\right) \exp\left(-i2kR_0 + i\alpha(\tau - 2R_0/c)^2\right) \tag{3.10}$$

where $k = 2\pi/\lambda$ is the wavenumber. The received signal is then correlated with a reference signal which is a complex conjugate of the transmitted signal,

$$s_r(\tau) = \text{rect}(\tau/\tau_p) \exp(-i\alpha\tau^2) \tag{3.11}$$

The complex amplitude of the point image is give by the correlation integral

$$s_R(\tau') = \int_{-\infty}^{\infty} s_r(\tau' + \tau) s_r(\tau) d\tau \tag{3.12}$$

where τ' is the time variable in the image plane. Because the phase of the reference signal is "matched" to that of the transmitted signal, the correlation process of equation (3.12) is called "matched filtering" in time domain. In real SAR processors, the matched filtering is carried out in the frequency domain, *i.e.*, the received signal is Fourier transformed, multiplied by the reference spectrum which is the Fourier transform of the reference signal, and finally the resultant image spectrum is inverse Fourier transformed to produce the image in time (or equivalent space) domain.

Equation (3.12) for $\tau > 0$ can be evaluated readily to obtain [30]

$$s_R(\tau') = S_0 \exp(-i2kR_0)(\tau_p - |\tau' - 2R_0/c|)\text{sinc}\left(\alpha(\tau' - 2R_0/c)(\tau_p - |\tau' - 2R_0/c|)\right) \tag{3.13}$$

where $\text{sinc}(z) = \sin(z)/z$. The image coordinate of equation (3.13) is centered at the antenna (the time of pulse transmission). It is convenient to change the center to the center of the slant-range as

$$\tau_R = \tau' - 2R_0/c \tag{3.14}$$

Equation (3.13) can then be written in a simple form

$$s_R(\tau_R) = S_0 \exp(-i2kR_0)(\tau_p - |\tau_R|)\text{sinc}\left(\alpha\tau_R(\tau_p - |\tau_R|)\right) \tag{3.15}$$

This is the complex amplitude of a point image, called the *point spread function* (PSF) or *impulse response function* (IRF). The intensity PSF is given by

$$|s_R(\tau_R)|^2 = |S_0|^2(\tau_p - |\tau_R|)^2\text{sinc}^2\left(\alpha\tau_R(\tau_p - |\tau_R|)\right) \tag{3.16}$$

Fig.3.5 shows the intensity PSF.

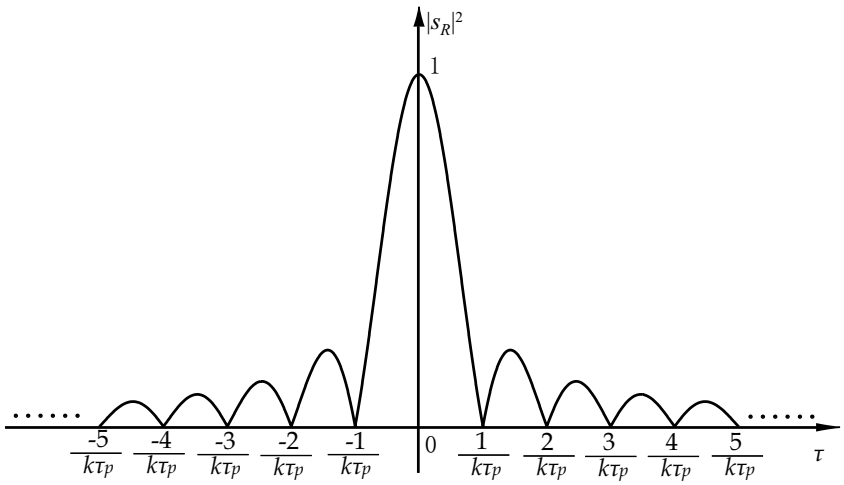

Figure 3.5: Intensity point spread function in the range direction.

3.2.3 Range Resolution

The generally accepted definition for SAR resolution is the -3 dB criterion for two-point resolution. The two-point resolution defines the ability of distinguishing the images of two neighbouring point scatterers. According to the -3 dB criterion, the size of the resolution cell $\Delta\tau_R$ is defined as the distance between two PSFs when the peak of the sum of the two PSFs equals the peak value of a single PSF. In equation (3.16), this distance corresponds to that from the center of the PSF to the position where the PSF has the -3 dB value if the peak value is set to 0 dB. The Rayleigh criterion defines the two point resolution as the distance between the two PSFs when the center of a PSF is at the first zero of the other PSF. In practice, the -3 dB resolution is often approximately by the Rayleigh resolution. The resolution cell $\Delta\tau_R$ based on the Rayleigh criterion can be deduced by solving

$$\alpha\Delta\tau_R(\tau_p - |\Delta\tau_R|) = \pi \tag{3.17}$$

and assuming $\tau_p B_R \ll 1$ ($B_R = |\alpha|\tau_p/\pi$). The result is

$$\Delta\tau_R = 1/B_R \tag{3.18}$$

and in terms of the ground-range variable Y in the image plane ($Y = c\tau_R/(2\sin\theta_i)$), the range PSF is expressed as

$$|s_R(Y)|^2 = |S_0|^2 \mathrm{sinc}^2(\pi Y/\Delta Y) \tag{3.19}$$

and the resolution cell is defined by

$$\Delta Y = \frac{\pi c}{2|\alpha|\tau_p \sin\theta_i} \tag{3.20}$$

For the JERS-1 SAR, the range resolution cell is 16 m. For the airborne Pi-SAR, the range resolution is 1.5 m and 3 m at X-band and L-band respectively.

3.2.4 Aperture Synthesis in Azimuth Direction

In the preceding subsection, the range PSF is derived for a point scatterer at a fixed range R_0. However, the SAR antenna transmits and receives series of pulses as it travels in the azimuth direction. As shown in Fig.3.6, consider that the antenna on board of the satellite or aircraft platform at an arbitrary azimuth time t transmits and receives signals from a point scatterer at the distance R, where v_a is the platform velocity. The distance R_0 is the slant-range distance when the antenna is nearest to the scatterer.

The recieved signal given by equation (3.8) is

$$s(\tau) = S_0 \mathrm{rect}\left((\tau - 2R_0)/\tau_p\right) \exp\left(i\omega_c(\tau - 2R_0/c) + i\alpha(\tau - 2R_0/c)^2\right) \tag{3.21}$$

The last exponential term is used to process the range component of the signal from a scatterer at a fixed position R_0. For azimuth aperture synthesis, the azimuth time dependence of the first exponential term of equation (3.21) is used. The azimuth component of the received signal can be written as

$$s_r(t) = S_0 \exp(-i2kR(t)) \tag{3.22}$$

where $k = 2\pi/\lambda = \omega_c/c$ as before, and unnecessary terms have all been absorbed in S_0. Note that the received signal is now a function of t. The slant-range distance $R(t)$ can be deduced from

$$R(t) = (R_0^2 + x^2)^{1/2} \tag{3.23}$$

where the azimuth spatial variable x is given by

$$x = v_a t \tag{3.24}$$

Here, we assume the Earth is flat. This assumption is valid for airborne SARs, but it is not for spaceborne

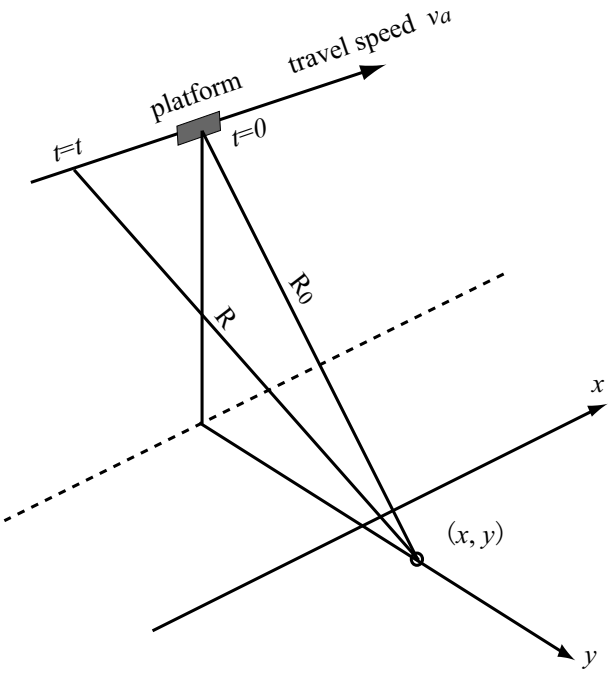

Figure 3.6: Illustrating a geometry of a point scatterer and the platform at different azimuth times.

SARs as described in [30]. In general, $R \gg x$ then equation (3.23) can be approximated as

$$\begin{aligned} R(t) &= [R_0^2 + x^2]^{1/2} \\ &\approx R_0 \left[1 + \frac{x^2}{2R_0^2}\right]^{1/2} \\ &= R_0 \left[1 + \frac{(v_a t)^2}{2R_0^2}\right]^{1/2} \end{aligned} \tag{3.25}$$

The recieved signal then becomes

$$s(t) = S_0 \exp\left(-i2kR_0 - ik\frac{(v_a t)^2}{R_0}\right) \tag{3.26}$$

Then the instantaneous frequency of the return signal can be given by differentiating the Doppler phase $\phi(t) = -2kr(t)$ as

$$\begin{aligned} f(t) &= \frac{1}{2\pi}\frac{d\phi(t)}{dt} \\ &= \frac{2v_a^2}{\lambda R_0}t \\ &= \frac{\beta}{\pi}t \end{aligned} \tag{3.27}$$

where β is the Doppler constant, and β/π is the Doppler rate given by

$$\beta = -\frac{2\pi v_a^2}{\lambda R_0} \tag{3.28}$$

In a same way as for the range processing, the image complex amplitude in the azimuth direction is given by correlating the received signal of equation (3.26) with a reference signal $s_r(t)$. This reference signal is the complex conjugate of the received signal defined by

$$s_r(t) = \text{rect}(t/\tau_A) \exp\left(ik\frac{(v_a t)^2}{R_0}\right) \tag{3.29}$$

where the constant term is ignored, and

$$\begin{aligned} \text{rect}(\frac{t}{\tau_A}) = 1 \quad &: \quad \text{when} -\frac{\tau_A}{2} \leq t \leq \frac{\tau_A}{2} \\ 0 \quad &: \quad \text{otherwise} \end{aligned} \tag{3.30}$$

Equation (3.30) is the weighting function for the synthesized aperture, and τ_A is the integration time taken to synthesize the aperture. The time of aperture synthesis is related to the synthetic aperture length L_A by

$$L_A = v_a \tau_A \tag{3.31}$$

The correlation integral is

$$s_A(t') = \int_{-\infty}^{\infty} s(t'+t) s_r(t)\, dt \tag{3.32}$$

where t' is the time variable in the image plane. The integral can easily be evaluated to yield the complex PSF in the azimuth direction of the form

$$s_A(t') = S_0 \exp\left(-i\beta t'^2\right) \text{sinc}\left(\pi B_D t'\right) \tag{3.33}$$

where S_0 is a constant, and B_D is effective Doppler bandwidth which is given by

$$\begin{aligned} B_D &= |\beta|\tau_A/\pi \\ &= \frac{2v_a^2}{\lambda R_0}\tau_A \end{aligned} \tag{3.34}$$

The intensity PSF is

$$|s_A(t')|^2 = |S_0|^2 \text{sinc}^2(\pi B_D t') \tag{3.35}$$

3.2.5 Azimuth resolution

The intensity PSF can be expressed in terms of the image spatial variable $X = v_a t'$ in the azimuth direction as

$$|s_A(X)|^2 = |S_0|^2 \text{sinc}^2(\pi X/\Delta X) \tag{3.36}$$

where ΔX is the spatial resolution cell defined as

$$\Delta X = \frac{\lambda R_0}{2L_A} \tag{3.37}$$

and the time resolution can be given by

$$\Delta t_A = \frac{1}{B_D} \tag{3.38}$$

Further, as a rule of thumb, the angle of -3 dB beam width of an antenna with length D_A is

$$\Psi \simeq \lambda / D_A \tag{3.39}$$

the corresponding distance or the synthetic aperture length can be given by

$$v_a \tau_A = L_A = \lambda R_0 / D_A \tag{3.40}$$

by substituting equation (3.40) into (3.37), the azimuth resolution can also be given by

$$R_a = \frac{D_A}{2} \tag{3.41}$$

Thus, in principle, the nominal azimuth resolution cell is half the azimuth antenna length. The antenna length of JERS-1 SAR is 12.0 m, and therefore the resolution cell is 6.0 m. The same resolution value can be obtained by substituting the radar parameters into equation (3.37).

3.3 Examples of SAR Systems Parameters

The successful launch of SEASAT in 1978 opened a spaceborne SAR era, and many satellite SARs were launched providing abundant information of the Earth. Table 3.2 lists several satellite SAR systems parameters. In this thesis, among the satellite SAR systems, JERS-1 SAR and RADARSAT-1 data are used to verify the theory proposed in chapter 6.

Table 3.2: Examples of system parameters of spaceborne SARs (modified from [30]).

Satellite	SEASAT	JERS-1	RADARSAT-1	ENVISAT	ALOS
Country/Organization	NASA	Japan	Canada	ESA	Japan
Launch year	1978	1992	1995	2002	2006
Altitude (km)	790	568	800	800	691
Az antenna length (m)	10.7	12.0	15.0	10.0	8.9
Rg antenna length (m)	2.2	2.2	1.6	1.3	3.1
Center frequency (GHz)	1.275	1.275	5.3	5.331	1.27
Wavelength (cm)	23.5	23.5	5.7	5.6	23.6
Band	L	L	C	C	L
Polarization	HH	HH	HH	VV or HH	full
Off-nadir angle	23°	35°	20°-50°	14°-45°	21°, 34°, 43°
Rg resolution (m)	25	18	30	30	7-100
Swath width (km)	100	75	45-500	100-400	20-350

In addition to spaceborne SAR systems, airborne SARs are developed by many countries. Spaceborne SARs are useful for covering large areas (order of 100 km) with intermediate resolution (order of 6-20 m), while airborne SARs can cover smaller areas (order of 10 km swath) with higher resolution (order of 1 m). The airborne Pi-SAR data are also used in this thesis and applied to estimate forest parameters. The Pi-SAR was developed jointly by NICT (National Institute of Information and Communications Technology) and JAXA (Japan Aerospace Exploration Agency) [59]. It is equipped with fully polarimetric and interferometric X-band (frequency 9.55 GHz, wavelength 3.14 cm), and polarimetric L-band (frequency 1.27 GHz, wavelength 23.6 cm) antennas, capable of producing imagery with nominal spatial resolution of 1.5×1.5 m at X-band and 3×3 m at L-band for 4 looks in the azimuth direction as listed in Table 3.2 .

3.4 Multilook Processing

3.4.1 Concept of Multilook Processing

In the azimuth imaging process described in the previous section, the synthetic aperture length is taken as a maximum available length, and the image is termed as a “single-look” or “full-look” image. As a result, the

resolution in the azimuth direction is generally finer than that in the ground-range direction. For example the resolution cell of JERS-1 SAR is 18 m in the range direction, while the full-look azimuth resolution cell is 6 m. The single-look image may be inconvenient for visual display and image analysis. To equalize the azimuth resolution to range resolution, a technique called "multilook processing" is used. In this processing scheme, a full synthetic aperture is divided into two or more sub-apertures and the corresponding sub-images are produced individually. Because the full aperture is divided, the resolution is reduced by the same factor, *e.g.*, the resolution cell of N-look sub-images is $1/N$ times the full-look resolution.

Other purpose of multilook processing is speckle reduction. Since the sub-images are produced by non-overlapping sub-apertures independently, speckle is uncorrelated between looks. Addition of multilook images on an intensity basis, therefore, reduces speckle noise by the factor $1/\sqrt{N}$. Because N-look images require processing the raw SAR data by N times, the computing time is longer than the single-look processing. The same effects can be obtained by averaging azimuth pixels in a single-look intensity image. This multilook by "pixel averaging" is adopted for general SAR image formats. Multilook processing also affects the statistical properties of SAR images. The amplitude and intensity PDFs of K-distribution of multilook processed image are given in Appendix B. The effects on speckle reduction and resolution degradation are same for both the processing schemes only for stationary surfaces. If the surface is moving, then the multilook images may differ from the speckle-averaged images. To distinguish the two, multilook processing by sub-apertures is called "split-look" processing. In this thesis, multilook or split-look processing is used to examine the inter-look speckle cross-correlation in the images of dynamic ocean surface, and therefore, it is useful to summarise the imaging process of a point scatterer by multilook processing.

3.4.2 Multilook Point Spread Function

For N-look processing, the reference signal is set as

$$s_r(t) = \mathrm{rect}[(t-\tau_n)/(\tau_A/N)] \exp\left(ik\frac{(v_a t)^2}{R_0}\right) \tag{3.42}$$

where

$$\begin{aligned} \mathrm{rect}[(t-\tau_n)/(\tau_A/N)] &= 1 : -\tau_A/(2N) \le t-\tau_n \le \tau_A/(2N) \\ &= 0 : \text{otherwise} \end{aligned} \tag{3.43}$$

In these equations, τ_n is the center time of look n sub-aperture, given by

$$\tau_n = \frac{\tau_A}{2N}(2n - N - 1) \tag{3.44}$$

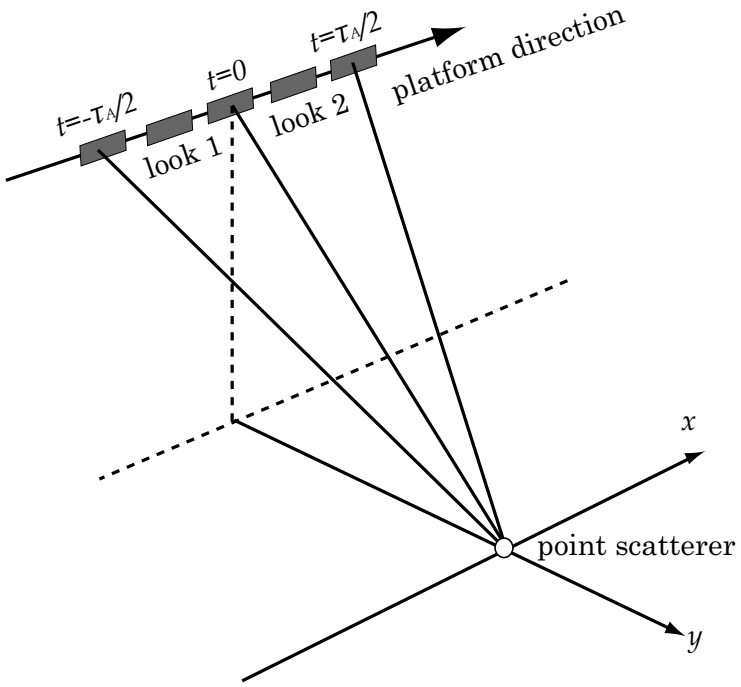

Figure 3.7: Illustrating multilook processing by dividing a full synthetic aperture into 2 sub-apertures.

Fig.3.7 is a illustration of 2-look processing, where the raw data in [$-\tau_A/2$, 0] is selected by the look 1 sub-aperture to form a look 1 image and look 2 image is formed by the raw data in [0, $\tau_A/2$] selected by the look 2 sub-aperture. As shown in Fig.3.7, if $N = 2$ for example, the integration time of each sub-aperture is $\tau_A/2$, the center time $\tau_n = (\tau_A/4)(2n - 3)$, and therefore $\tau_1 = -\tau_A/4$ and $\tau_2 = \tau_A/4$ for look 1 and look 2 respectively.

The PSF of multilook can be deduced by the correlation between the received signal of equation (3.26) and the sub-reference signal of equation (3.42) in the same way as for the single-look PSF.

$$\begin{aligned} s^{(n)}(t') &= S_0 \int_{-\tau_A/(2N)+\tau_n}^{\tau_A/(2N)+\tau_n} \exp(i2\beta t' t)dt \\ &= S_0 \exp(i2\beta\tau_n t')\mathrm{sinc}(\pi B_{DN} t') \end{aligned} \tag{3.45}$$

where B_{DN} is N-look Doppler bandwidth given by

$$\begin{aligned} B_{DN} &= (|\beta|/\pi)\left(\frac{\tau_A}{N}\right) \\ &= \frac{2v_a^2}{\lambda R_0}\left(\frac{\tau_A}{N}\right) \end{aligned} \tag{3.46}$$

and the spatial resolution is

$$\Delta X_N = \frac{\lambda R_0}{2v_a(\tau_A/N)} \tag{3.47}$$

It can be seen from equation (3.46) and (3.47) that the multilook processing splits the full bandwidth into equal N pieces, and therefore the spatial resolution N-look image is reduced to $1/N$ times the resolution of the single look image.

Fig.3.8 shows simulated single and multilook (2×2, 3×3, 4×4) images. In each image, the lower one is a speckle image only, and the upper one includes periodic intensity variation. As can be seen, as the look number increases, the speckle is reduced but at the expense of loss of resolution.

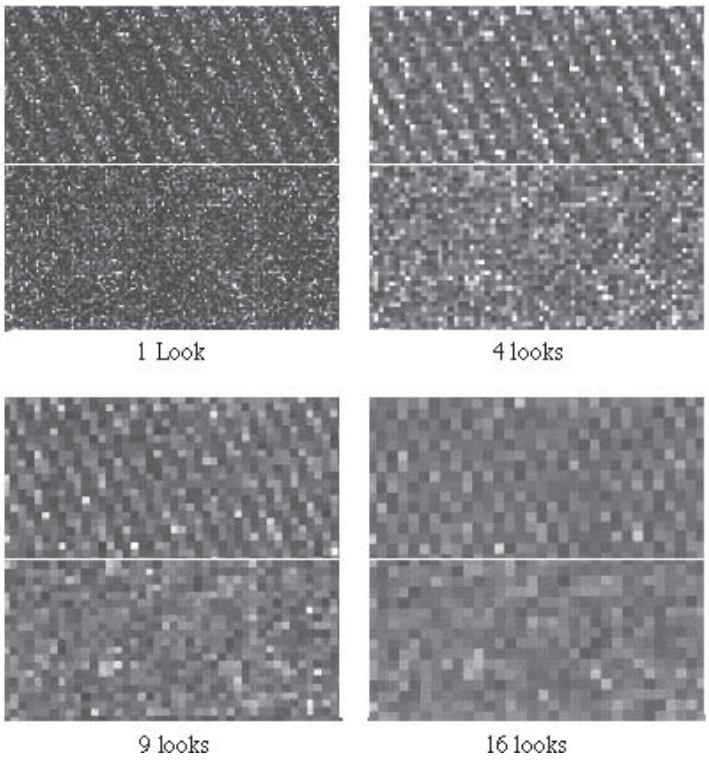

Figure 3.8: Simulated speckle images in different looks.

3.5 SAR Imaging of Extended Objects

The response of an isolated point target and system resolution were discussed in the previous sections. We now consider how the two dimensional SAR image is formed, that is, how the backscattered field of a scattering object is translated into image complex amplitude.

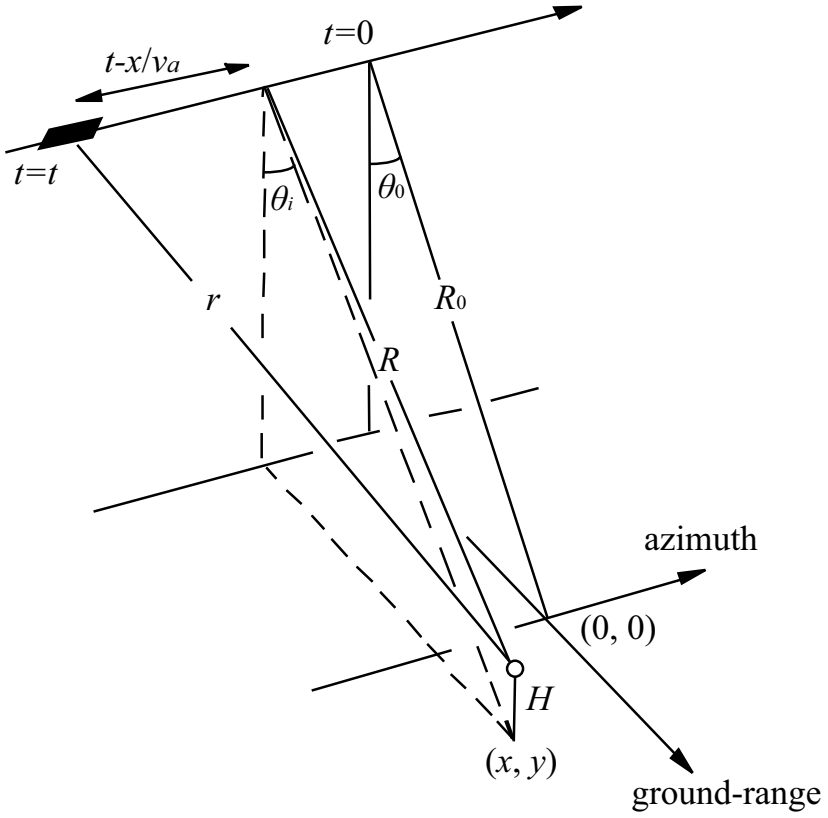

Figure 3.9: Illustrating a point scatterer of height H at a surface position (x, y).

3.5.1 Convolution Model

The image complex amplitude of an extended surface can be regarded as an assembly of many PSFs of different heights and scattering amplitudes. Let $\sqrt{\sigma(x,R)}$ be the scattering amplitude of a point scatterer of height H at the surface position (x, R) as in Fig.3.9. Thus, for a continuous scattering surface, the two-dimensional image complex amplitude is given by the convolution of the two-dimensional PSFs and the complex backscattered field as

$$A(t',\tau') = A_0 \iint_{-\infty}^{\infty} \sqrt{\sigma(x,R)}\exp(-i2kR)s_A(t'-x/v_a)s_R(\tau'-2R/c)\,dxdR \tag{3.48}$$

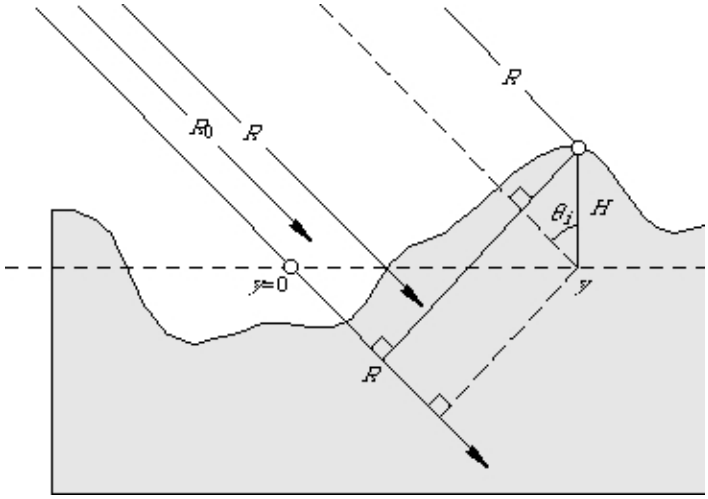

Figure 3.10: Approximation for the slant-range distance.

where A_0 is normalized constant, and

$$s_A(t' - x/v_a) = \exp(i\beta(t' - x/v_a)^2)\text{sinc}(\beta T_A(t' - x/v - a)) \tag{3.49}$$

$$s_R(\tau' - 2R/c) = \exp(i\alpha(\tau' - 2R/c)^2)\text{sinc}(\alpha\tau_0(\tau' - 2R/c)) \tag{3.50}$$

are the complex PSFs in the azimuth and slant-range directions respectively. It is convenient to express the image complex amplitude in terms of spatial variables rather than temporal variables. Using the transformation

$$\begin{aligned} X &= v_a t' \\ Y \sin\theta_i &= c\tau'/2 - R_0 \end{aligned} \tag{3.51}$$

the image complex amplitude can be expressed in a simple convolution integral

$$A(X,Y) = A_0 \iint_{-\infty}^{\infty} a(x,y) E_{AR}(X-x, Y-y)\, dx\, dy \tag{3.52}$$

where a is the complex backscattered field

$$a(x,y) = \sqrt{\sigma(x,y)}\exp(i\psi(x,y)) \tag{3.53}$$

where ψ is the phase that can be approximated as (see Fig.3.10)

$$\psi(x,y) = -2k[H(x,y)\cos\theta_i - y\sin\theta_i] \tag{3.54}$$

and E_{AR} is the two-dimensional PSF defined by

$$E_{AR}(X,Y) = s_A(X)s_R(Y) \tag{3.55}$$

It should be noted that all unwanted terms are absorbed in the constant term A_0. Equation (3.52) is the fundamental convolution model to describe the SAR image complex amplitude in terms of the backscattered field.

3.5.2 Image Intensity and Ensemble Average

The image intensity is simply the modulus square of the complex amplitude of equation (3.52) as follows.

$$\begin{aligned} I(X,Y) &= |A(X,Y)|^2 \\ &= I_0 \iiiint_{-\infty}^{\infty} a(x_1,y_1)a^*(x_2,y_2)E_{AR}(X-x_1,Y-y_1) \\ &\quad \cdot E_{AR}^*(X-x_2,Y-y_2)\,dx_1dx_2dy_1dy_2 \end{aligned} \tag{3.56}$$

In practice, the intensity image contains speckle. To describe such randomly fluctuating image intensity, equation (3.56) is not adequate, and it is convenient to express the image structure by an ensemble average.

The backscattered field can be considered as composed of the deterministic and random components. An example of the deterministic component is the scattering amplitude and height of large-scale ocean waves, where "large-scale" implies "large compared with a resolution cell". The random component arises from small-scale capillary waves that are distributed randomly in space (and in time). In order to evaluate the random component statistically, the following assumptions are made.

1 the scattering amplitude $\sqrt{\sigma(x_1,y_1)}$ and phase $\psi(x_1,y_1)$ at a position (x_1,y_1) are statistical independent. This implies that the phase changes irrespective with the amplitude change.

2 the scattering amplitude $\sqrt{\sigma(x_1,y_1)}$ and phase $\psi(x_1,y_1)$ are statistically uncorrelated with $\sqrt{\sigma(x_2,y_2)}$ and $\psi(x_2,y_2)$. This implies that the backscattered field is δ-correlated.

3 there are many randomly distributed scatterers within a resolution cell and phases are uniformly distributed over $[-\pi,\pi)$. This assumption is used to describe speckle formation in the previous chapter.

The scattering model that satisfies these conditions is known as "(Gaussian) white noise model".

The ensemble average of the backscattered field is then given by

$$\langle a(x_1, y_1)a^*(x_2, y_2)\rangle = \langle\sqrt{\sigma(x_1, y_1)}\sqrt{\sigma(x_2, y_2)}\rangle\, \delta(x_1-x_2, y_1-y_2) \tag{3.57}$$

The ensemble average of the image intensity is given by

$$\langle I(X, Y)\rangle = I_0 \iint_{-\infty}^{\infty} \langle\sigma(x, y)\rangle\, |E_{AR}(X-x, Y-y)|^2\, dx\, dy \tag{3.58}$$

Thus, the speckle-averaged ensemble average of image intensity is given by the convolution of the ensemble average of the backscatter radar cross section, σ, with the two-dimensional intensity point spread functions.

3.6 Summary

In this chapter, the processes through which the PSF is produced from SAR raw data are summarised. The pulse compression technique using a matched filter for frequency modulated pulses is used to achieve fine resolution in the range direction. In the azimuth direction, the technique of aperture synthesis is used to construct am imaginary long aperture to produce fine azimuth images. Multilook processing is also described for it is applied to the speckle analysis from moving sea surfaces in Chapter 6. This processing technique is applied to image formation in the azimuth direction for the two purposes: to equalize the finer azimuth resolution to the resolution in the range direction, and to reduce speckle noise. In the final part, the principal theory of the convolution model is illustrated to describe the image complex amplitude of an extended surface. The SAR fundamentals given in this chapter serve as a foundation for understanding and analysing SAR images.

Chapter 4

Polarimetric Analysis

Conventional SAR systems use the microwave of only single polarization for transmitting and receiving signals. This type of SAR systems is called "non-polarimetric SAR". For example, a HH polarized system means that the antenna used for transmission and reception is linearly horizontally polarized. For non-polarimetric SAR, only a single scattering coefficient is measured for a specific combination of transmitted and received polarization. Therefore, the target information which can be attained from the polarization properties is unavailable. To find the polarimetric information of the scattered wave, polarimetric SAR systems are developed and most of modern airborne SARs today are in a full polarimetric mode. Among spaceborne SARs, the ENVISAT-ASAR is operating at a dual-polarization mode (HH and VV), and the ALOS-PALSAR has a single-, dual- and full polarimetric mode. The Pi-SAR data are fully polarimetric for both X- and L-bands [59].

SAR polarimetry is a popular emerging technique for extracting potential information contained in the polarimetric data, which cannot be attained from single-polarization data. It is certainly useful in analysing different scattering processes and image classification. Although the study reported in this thesis is not directly related SAR polarimetry, polarimetric analyses are presented in this chapter because it can help to understand the scattering mechanisms from vegetated and forested scenes. The data used for polarimetric analyses are the Pi-SAR images of the rice fields in Okayama, and Tomakomai forests in Hokkaido, Japan.

In the first part of this chapter, the fundamentals of electromagnetic wave polarization is introduced, followed by the description of the well known techniques of the alpha-entropy and three-component decomposition analyses, and finally the results and discussions are presented for the Pi-SAR data of the rice fields and forests.

4.1 Polarization of Electromagnetic Wave

Electromagnetic (EM) wave is a transversal wave whose electric and magnetic fields are perpendicular to the propagation direction. Since the magnetic field vector is orthogonal to electric filed, and can be calculated

from the electric field vector easily, we will only focus on electric field vector. To illustrate the polarization states of EM waves, *plane wave* is introduced. A plane wave is a constant-frequency wave whose wavefronts are infinite parallel planes normal to the phase velocity vector. In general case, the trace of the tip of the electric field within a plane is an ellipse, which means the EM wave is elliptically polarized, and the special cases are linearly and circularly polarizations [34].

To describe the EM wave polarization, a coordinated system and a reference propagation direction are needed. Since most of the fully polarized radars use two orthogonal linear polarized antennas, the Cartesian coordinate system is used as in Fig.4.1, where z is the direction of propagation. The corresponding electric field is located in $x-y$ plane, where $\vec{E}_x$ and $\vec{E}_y$ are the x-component and y-component of the electric vector respectively. The complex amplitudes are $\hat{E}_{x/y} = E_{x0/y0} \cdot e^{i\delta_{x/y}}$. Fig.4.1 shows the propagating EM wave whose electric field combined by two orthogonal components, and the EM wave can be represented by [16]. The electric field vector can be written as

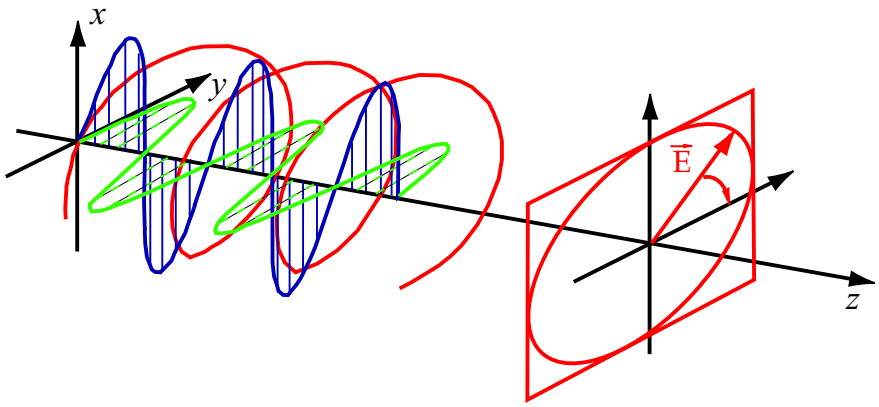

Figure 4.1: Illustrating the propagation of an electromagnetic plane wave. The trace of the tip of the electric field is also shown.

$$\vec{E}(z) = E_x(z)\vec{e}_x + E_y(z)\vec{e}_y \tag{4.1}$$

where $\vec{e}_x$ and $\vec{e}_y$ are unit vectors parallel to x- and y-axis respectively, and

$$\begin{aligned} \vec{E}_x(z) &= \vec{E}_x e^{ikz} = E_{x0} e^{ikz} e^{i\delta_x} \vec{e}_x \\ \vec{E}_y(z) &= \vec{E}_y e^{ikz} = E_{y0} e^{ikz} e^{i\delta_y} \vec{e}_y \end{aligned} \tag{4.2}$$

Therefore, the instantaneous values of $\vec{E}_x(z,t)$, $\vec{E}_y(z,t)$ are

$$\vec{E}_x(z,t) = E_{x0}\cos(\omega t - kz + \delta_x)$$

$$\vec{E}_y(z,t) = E_{y0}\cos(\omega t - kz + \delta_y) \tag{4.3}$$

respectively. The general case is elliptical polarization, where $E_{x0} \neq 0$, $E_{y0} \neq 0$ and $\delta_y - \delta_x = \delta_0 \neq 0$. Then we may rewrite (4.3) as

$$\begin{aligned} \vec{E}_x(z,t) &= E_{x0}\cos(\omega t - kz) \\ \vec{E}_y(z,t) &= E_{y0}\cos(\omega t - kz + \delta_0) \end{aligned} \tag{4.4}$$

To eliminate the term $(\omega t - kz)$, expand (4.4) into

$$\begin{aligned} \frac{\vec{E}_x(z,t)}{E_{x0}}\cos(\delta_0) &= \cos(\omega t - kz)\cos(\delta_0) \\ \frac{\vec{E}_y(z,t)}{E_{y0}} &= \cos(\omega t - kz)\cos(\delta_0) + \sin(\omega t - kz)\sin(\delta_0) \end{aligned} \tag{4.5}$$

By using the relation of trigonometric functions, the result can be given as

$$\left(\frac{E_x(z,t)}{E_{x0}}\right)^2 + \left(\frac{E_y(z,t)}{E_{y0}}\right)^2 - 2\left(\frac{E_x(z,t)E_y(z,t)}{E_{x0}E_{y0}}\cos(\delta_0)\right) = \sin^2(\delta_0) \tag{4.6}$$

which is an ellipse equation with an inclination angle ψ_e such that

$$\tan(2\psi_e) = \frac{2E_{x0}E_{y0}}{E_{x0}^2 - E_{y0}^2}\cos(\delta_0) \tag{4.7}$$

Up to here, it can be seen that the polarization parameters can be represented by the ellipse parameters. This ellipse is called "polarization ellipse" as shown in Fig.4.2 The ellipticity angle is given by

$$\chi = \arctan\left(\pm\frac{a_\xi}{a_\eta}\right) \tag{4.8}$$

where a_ξ and a_η are the major and minor semi-axes of the ellipse. χ specifies the direction of rotation. Assuming that the observation is in the propagation direction, the polarization is called the *left handed* elliptical polarization for $x > 0$ and *right handed* elliptical polarization for $x < 0$. Moreover, the following relations exist,

$$\begin{aligned} \sin(2\xi) &= \sin(2\alpha_e)\sin(\delta) \\ \sin(2\psi_e) &= \tan(2\alpha_e)\cos(\delta) \end{aligned} \tag{4.9}$$

where the auxiliary angle α_e is defined as

$$\tan(\alpha_e) = \frac{E_{y0}}{E_{x0}} \tag{4.10}$$

As mentioned before, there are two limiting cases of elliptical polarization and they are *circular polarization* and *linear polarization*. If major and minor axes of the ellipse are equal, that is, $E_{x0} = E_{y0}$ and the phase difference $\delta_0 = \pm\pi/2 + 2n\pi$, where $n = 0, \pm1, \pm2, \ldots$, then elliptical polarization become *circular polarization*. If the phase angle difference is 0 ($\delta_0 = 0$), then the trace of the tip of the electric field will be a straight line, that is, the wave is linearly or plane polarized. The modulus of $\vec{E}_x(z,t)$ is then given by

$$|\vec{E}_x(z,t)| = \sqrt{E_{x0}^2 + E_{y0}^2} \cdot \cos(kz + \omega t - \delta_0) \tag{4.11}$$

In this case, equation (4.7) can be simplified as

$$\tan(\psi) = \frac{E_{y0}}{E_{x0}} \tag{4.12}$$

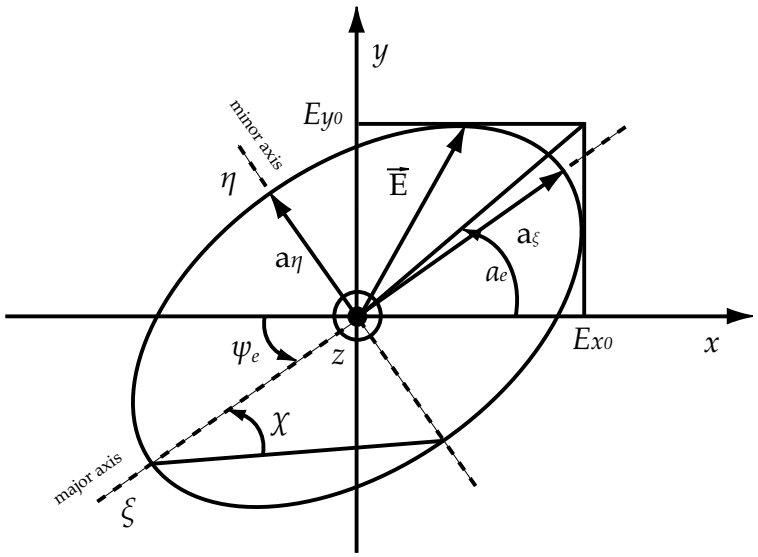

Figure 4.2: Polarization ellipse in $x - y$ plane and EM wave propagates along $z-$axis direction, with inclination angle ψ_e, ellipticity angle χ, and auxiliary angle α_e.

4.2 Parameters in Polarimetry

4.2.1 Scattering Matrix

When the EM wave is linearly polarized, the two orthogonal components are horizontal (H) and vertical (V) polarization. By using $S_{mn} = |S_{mn}|e^{i\phi_{mn}}$, where $m, n \in \{h, v\}$ to denote the complex scattering amplitude, where m is the polarization state of transmitted wave and n means the received polarization state. S_{hh} and S_{vv} are called co-polar and S_{hv} and S_{vh} cross-polar components. Since *reciprocity theorem* will hold for monostatic systems and reciprocal media, $S_{hv} = S_{vh}$. The received field with a distance R can be considered as a linear transformation, and the backscattered wave is then given by [16], [34]

$$\begin{pmatrix} E_{sh} \\ E_{sv} \end{pmatrix} = \frac{e^{ikR}}{R} \begin{pmatrix} S_{hh} & S_{hv} \\ S_{vh} & S_{vv} \end{pmatrix} \begin{pmatrix} E_{ih} \\ E_{iv} \end{pmatrix} \tag{4.13}$$

The second term in the right part of the above equation is named as scattering ([S]-) matrix, and sometimes it is also referred as *Johnes* matrix. The scattering matrix contains 8 independent parameters, including 4 different polarization combinations and their phases. The phases are relative and hence they are expressed with respect to the phase of a particular polarization signal. In general, this reference phase is taken as that of the HH-polarization signal. In this thesis, we assume that all the targets are reciprocal ($S_{hv} = S_{vh}$) because SAR is a monostatic radar. Therefore, there are five independent parameters in the [S]-matrix. They are three complex amplitudes S_{hh}, S_{vv}, S_{hv} and two phase differences $\phi_{hh} - \phi_{hv}$ and $\phi_{hh} - \phi_{vv}$.

4.2.2 Scattering Vector

We can use one complex vector $\vec{q}$ which contains complete information of [S]-matrix to describe the scattering process. It is given by

$$[S] = \begin{bmatrix} S_{hh} & S_{hv} \\ S_{vh} & S_{vv} \end{bmatrix} \rightarrow \vec{q} = \frac{1}{2}\text{Trace}([S]\Psi) = [k_0, k_1, k_2, k_3]^T \tag{4.14}$$

where Trace$(\cdot)$ means the sum of the diagonal elements of the matrix, T means a transpose of a matrix, and Ψ is a 2×2 complex basis matrix under a Hermitian inner product. There are widely used two bases,

Borgeaud basis and *Pauli* basis. The *Borgeaud* basis is given by [34]

$$\Psi_B = 2\left\{\begin{bmatrix}1 & 0\\ 0 & 0\end{bmatrix}, \begin{bmatrix}0 & 1\\ 0 & 0\end{bmatrix}, \begin{bmatrix}0 & 0\\ 1 & 0\end{bmatrix}, \begin{bmatrix}0 & 0\\ 0 & 1\end{bmatrix}\right\} \tag{4.15}$$

The corresponding complex vector $\vec{q}_B$ is straightforward, and it is given by

$$\vec{q}_B = [S_{hh}, S_{hv}, S_{vh}, S_{vv}]^T \tag{4.16}$$

Pauli basis is

$$\Psi_P = \sqrt{2}\left\{\begin{bmatrix}1 & 0\\ 0 & 1\end{bmatrix}, \begin{bmatrix}1 & 0\\ 0 & -1\end{bmatrix}, \begin{bmatrix}0 & 1\\ 1 & 0\end{bmatrix}, \begin{bmatrix}0 & -i\\ i & 1\end{bmatrix}\right\} \tag{4.17}$$

The corresponding vector $\vec{q}_P$ is then

$$\vec{q}_P = \frac{1}{\sqrt{2}}[S_{hh} + S_{vv}, S_{hh} - S_{vv}, S_{hv} + S_{vh}, i(S_{vh} - S_{hv})]^T \tag{4.18}$$

The coefficients in the above two bases, 2 and $\sqrt{2}$, are used to normalize their corresponding vectors. Moreover, according to the reciprocity assumption, $S_{hv} = S_{vh}$, and the vector $\vec{q}_P$ can be simplified as

$$\vec{q}_P = \frac{1}{\sqrt{2}}[S_{hh} + S_{vv}, S_{hh} - S_{vv}, 2S_{hv}]^T \tag{4.19}$$

4.2.3 Coherence Matrix

The scattering matrix is used to describe the scattering process of individual targets. However, for SAR system, the resolution cell is always larger than the radar wavelength, leading to the [S]-matrix in one resolution cell consisting of many $[S]_i$. Therefore, a coherence matrix is introduced to deal with the statistical effects. The coherent matrix is given by the product of the vector $\vec{q}$ and its conjugate of the transposed vector $\vec{q}^*$ [16]. For the latter use, only the coherence matrix corresponding $\vec{q}_P$ is given here. Using equation (4.19), the coherent matrix is given by

$$[T] = \left\langle \vec{q}_P \vec{q}_P^{*T} \right\rangle = \frac{1}{2}\begin{bmatrix} \langle |A|^2 \rangle & \langle AB^* \rangle & \langle AC^* \rangle \\ \langle A^*B \rangle & \langle |B|^2 \rangle & \langle BC^* \rangle \\ \langle A^*C \rangle & \langle B^*C \rangle & \langle |C|^2 \rangle \end{bmatrix} \quad \text{where} \begin{cases} A = S_{hh} + S_{vv} \\ B = S_{hh} - S_{vv} \\ C = 2S_{hv} \end{cases} \tag{4.20}$$

where $\langle\cdot\rangle$ denotes a spatial ensemble average as before.

4.2.4 Alpha-Entropy Analysis

The alpha-entropy approach is based on the eigenvector analysis of the coherency matrix (4.20), where the *alpha* angle is related to the target scattering type with $0° \leq \alpha \leq 90°$, and the entropy describes the randomness of a scattering process. Because the coherency matrix is Hermitian, positive and semidefinite, it can always be diagonalized by using unitary similarity transformation. Thus, the coherency matrix can be diagonalized as [35]

$$\langle[T]\rangle = [U_3][\Lambda][U_3]^{*T} = [U_3]\begin{bmatrix} \lambda_1 & 0 & 0 \\ 0 & \lambda_2 & 0 \\ 0 & 0 & \lambda_3 \end{bmatrix}[U_3]^{*T} \tag{4.21}$$

where [Λ] is the diagonal eigenvalue matrix of [T] and the real eigenvalues satisfy $\lambda_1 \geq \lambda_2 \geq \lambda_3$, and the unitary matrix [U_3] is given by

$$[U_3] = \begin{bmatrix} \cos(\alpha_1) & \cos(\alpha_2) & \cos(\alpha_3) \\ \sin(\alpha_1)\cos(\beta_1)e^{i\delta_1} & \sin(\alpha_2)\cos(\beta_2)e^{i\delta_2} & \sin(\alpha_3)\cos(\beta_3)e^{i\delta_3} \\ \sin(\alpha_1)\cos(\beta_1)e^{i\gamma_1} & \sin(\alpha_2)\cos(\beta_2)e^{i\gamma_2} & \sin(\alpha_3)\cos(\beta_3)e^{i\gamma_3} \end{bmatrix} \tag{4.22}$$

The polarimetric scattering entropy H is defined by

$$H = \sum_{i=1}^{n}(-P_i \log_n P_i) \quad \text{where} \quad P_i = \frac{\lambda_j}{\sum_{j=1}^{n}\lambda_j} \tag{4.23}$$

where $n = 3$, and $0 \leq H \leq 1$. For example, if $H = 0$, it means that only $\lambda_1 \neq 0$ and the scattering type is deterministic, while all the eigenvalues are equal when $H = 1$.

The alpha angle is always given by the average

$$\bar{\alpha} = P_1\alpha_1 + P_2\alpha_2 + P_3\alpha_3 \tag{4.24}$$

Since the alpha angle and entropy describe the scattering mechanism, this approach can be used in practical remote sensing applications, such as the classification of targets based on different scattering mechanisms. The $\alpha - H$ plane is often used for image classification as shown in Fig.4.3, where the data always fall within the inner curve (left side of the curve). The divided zones correspond to the following scattering processes

[35].

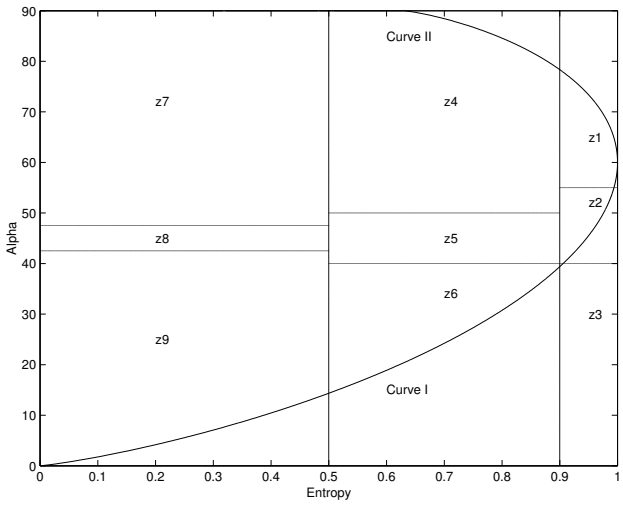

Figure 4.3: Feasible region in $\alpha - H$ plane for random media scattering problems [35].

- **Zone 1: High Entropy Multiple Scattering**

  Double bounce mechanisms in a high entropy environment can still be distinguished in this region. This mainly occurs in forests and vegetation with well developed branches and crown structure.

- **Zone 2: High Entropy Vegetation Scattering**

  Scattering from forest canopies lies in this region, and the scattering from some types of vegetated surfaces with random highly anisotropic scattering elements as well.

- **Zone 3: High Entropy Surface Scatter**

  The surface scattering mechanism cannot be identified when $H > 0.9$, and this zone is not within the feasible region in the $\alpha - H$ plane.

- **Zone 4: Medium Entropy Multiple Scattering**

  This zone accounts for dihedral scattering with moderate entropy. For example, double bounce mechanisms occur when P- or L-band EM propagation through forest canopy.

- **Zone 5: Medium Entropy Vegetation Scattering**

  Scattering from vegetation surfaces with anisotropic scatterers and moderate correlation of scatterer orientations occurs in this zone.

- **Zone 6: Medium Entropy Surface Scatter**

  The change of the surface roughness leading to the increase in entropy is shown in this zone. For example, surface scattering from low vegetation.

- **Zone 7: Low Entropy Multiple Scattering Events**

  Low entropy double or 'even' bounce scattering events occur in this zone, arising from isolated dielectric and metallic dihedral scatterers like buildings and man-made structures.

- **Zone 8: Low Entropy Dipole Scattering**

  Strongly correlated mechanisms having a large imbalance between hh- and vv-polarizations occur in this zone.

- **Zone 9: Low Entropy Surface Scatter**

  In this zone, low entropy surface scattering, such as scattering from water surface, sea ice as well as smooth land surface, dominates the scattering process.

4.2.5 Application to Pi-SAR Data of Tomakomai Forests

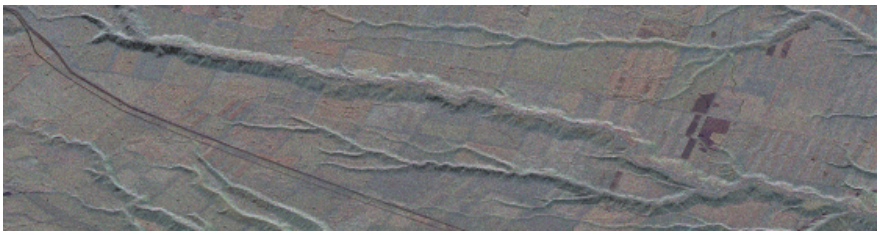

Figure 4.4: Pi-SAR L-band color composite image of Tomakomai forests acquired on the 7th of November, 2002. The red, green and blue colors correspond respectively to the HH-, HV- and VV-polarization data

Fig.4.4 is the Pi-SAR composite color image of the Tomakomai forests located in Hokkaido, Japan, acquired in November the 7th, 2002. The red, green and blue colors represent respectively to the HH-, HV- and VV-polarization data. In Fig.4.4, the illuminating (range) direction is from bottom to top, and the flight (azimuth) direction is from left to right. The alpha-entropy analysis is applied to the data with the moving window size of 9×9 and 20×20 pixels. The results are given in Fig.4.5.

It can be seen from Fig.4.5 that the pixels fall into the region 1, 2, 4, 5 and 6, and region 1, 2, 5 and 6 for 9×9 and 20×20 pixels moving window size respectively. It is because most of this area is dominated by forests with some roads and clear-cut areas. As the moving window size becomes large, the pixels belonging to non-forests tend to be smoothed out. From the results, it can be concluded that the $\alpha - H$ analysis can be a useful technique to distinguish different scattering mechanisms, such as those from forest, water or urban areas. However, it is difficult to quantify the amount of the scattering within a same scattering mechanism.

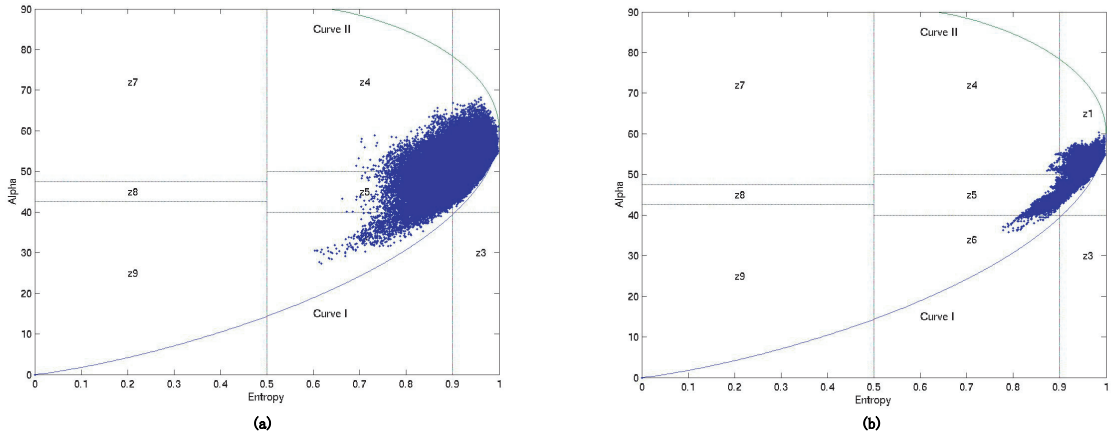

Figure 4.5: The results of $\alpha - H$ analysis of the Pi-SAR Tomakomai forests data with the moving window size (a) 9×9 pixels, (b) 20×20 pixels.

4.2.6 Three-Component Decomposition

Another polarimetric analysis is the three-component decomposition proposed by Freeman and Durden [36]. In this technique, image pixels are decomposed into 3 scattering mechanisms, namely, surface (single-bounce) scattering, double-bounce and volume scattering (the 4th component of helix scattering is included in the recent work [37]). Briefly, the analysis is carried out in the following manner.

The three-component decomposition analysis states that under the condition $\langle S_{HH}S_{HV}^{*}\rangle \simeq \langle S_{VV}S_{HV}^{*}\rangle \simeq 0$, the following 3 equations with 4 unknown parameters a, b, f_s, f_d can be deduced.

$$\begin{aligned}\langle|S_{HH}|^2\rangle &= f_s|b|^2+f_d|a|^2+f_v\\ \langle|S_{VV}|^2\rangle &= f_s+f_d+f_v\\ \langle S_{HH}S_{VV}^{*}\rangle &= f_s\,b+f_d\,a+f_v/3\end{aligned} \tag{4.25}$$

where the angular brackets indicates taking an ensemble average. In equation (4.25), f_s and f_d are the surface and double-bounce contributions, and f_v is the volume scattering contribution given by $f_v = 3\langle|S_{HV}|^2\rangle$. Equation (4.25) cannot be solved unless one of the unknown parameters is known. It is possible to assume that the surface scatter is dominant and put $a=-1$, if the real term of $\langle S_{HH}S_{VV}^{*}\rangle$ is positive. If the real term of $\langle S_{HH}S_{VV}^{*}\rangle$ is negative, then the double-bounce is dominant with $b=1$. Once the values of a, b, f_s, f_d are known from equation (4.25), the power of surface scattering, double-bounce and volume scattering can

be estimated from

$$P_s = f_s(1+|b|^2)$$
$$P_d = f_d(1+|a|^2)$$
$$P_v = 8f_v/3 \tag{4.26}$$

where P_s and P_d are the powers of the surface and double-bounce scattering respectively, and the power of the volume scattering P_v can be estimated directly from the cross-polarization contribution $f_v = 3\langle|S_{HV}|^2\rangle$.

4.2.7 Application to Kojima Rice Fields [85]

Color composite L-band (left) and X-band (right) Kojima images shown in Fig.4.6 were acquired on the 13th of July 1999, where red, green and blue denote HH-, HV- and VV-polarizations respectively. The results of the decomposition analysis are shown in Fig.4.7. The double-bounce, volume and surface scatterings are represented by red green and blue respectively. The azimuth and range directions are from top to bottom and from right to left respectively, and the incidence angle at the scene center is 38.4°. At the time of data acquisition in July, the rice plants were grown to their height approximately 50 cm with irrigation water underneath.

Figure 4.6: Pi-SAR L-band (left) and X-band (right) image of Kojima district, Okayama, Japan. The azimuth direction is from top to bottom and the range direction is from right to left. The image of size approximately 4 km in both directions was acquired on the 13th of July 1999, and the rice plants were almost fully grown with irrigation water underneath.

In the L-band result, the vertical red lines in the district marked “A” correspond to irrigation canals and

narrow roads with canals alongside as shown in Fig.4.8. These lines are at right angles to the radar illumination direction, so that the strong double-reflection, similar to the double-reflection by corner reflectors, occurs between the water surface and canal banks. There are several blue linear features along irrigation canals indicating the surface scattering from the canal banks with their sides facing toward the radar. The surface scattering can also be seen along the canals in the district "B". These canals are closely, but not exactly, at right angles to the radar illumination direction. The canals and roads in the districts "C" and "D" are not at right angles to the radar illumination direction, and hence the double-bounce is not a dominant scattering mechanism in these districts. Small red images along the roads are the result of double-bounce between house flanks and ground, and between the water surface and the bridge connecting the district "A" and "C" at lower left.

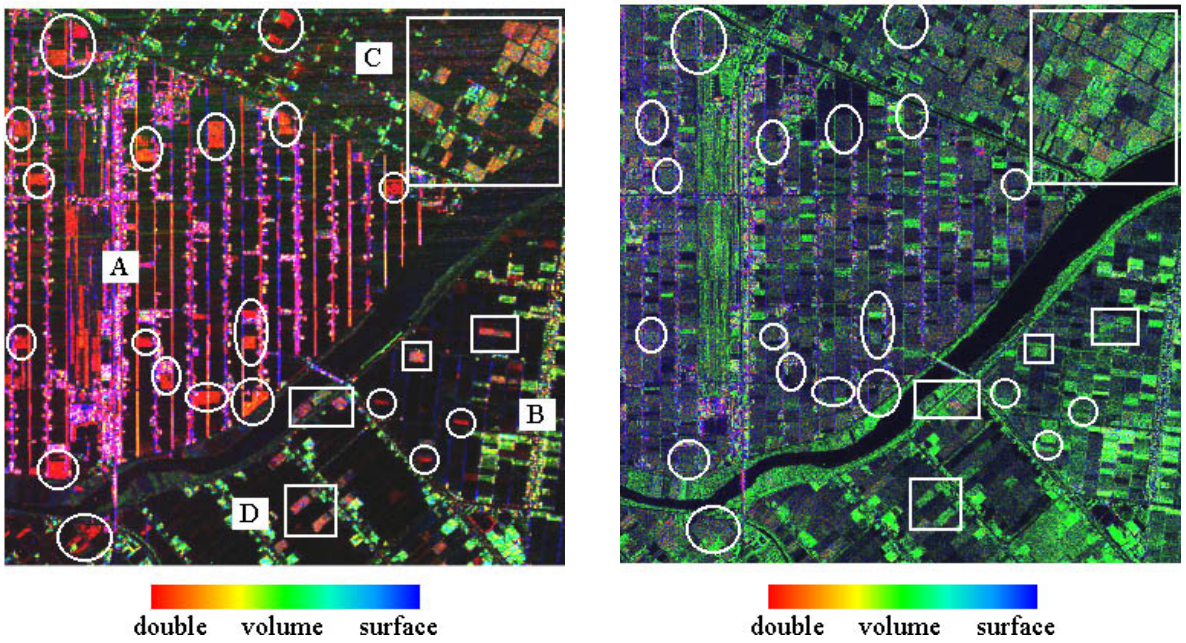

Figure 4.7: The decomposition analysis of L- (left) and X-band (right) Pi-SAR image of the Kojima district in Fig.[4.6].

The bright red areas inside the white circles indicate the double-bounce scattering which gives rise to the Bragg scattering. The backscattered power from the branches that do not satisfy the Bragg condition is very weak. The white square areas indicate lotus ponds as shown in Fig.4.9. In July, lotus plants are almost fully grown to their height of 150-170 cm with stalk diameter of 2-3 cm and circular leaves of diameter about 70 cm. They are cultivated in ponds, and stalks are distributed randomly. The backscatter from the lotus ponds is a result of the double-bounce between the water surface and stalks, and between leaves and/or stalks.

Figure 4.8: Irrigation canal and a narrow road alongside in the Kojima district.

Figure 4.9: Lotus ponds in the Kojima district.

The L-band decomposition result can be compared with the X-band decomposition result shown in the right part of Fig.4.7. Fig.4.10 shows the regularly planted rice plants in Kojima district. At X-band, the backscattering from rice fields is dominated by the surface scattering from the leaves of rice plants on the crown part. The volume scattering is caused mainly from tall vegetation including shrubs, reeds and lotus plants. The double-bounce scattering is only due to the house flanks and ground, and also the bridge at lower left. The effect of double-bounce from the canals is reduced considerably, because plants on the canal banks are "rough" for X-band microwave, yielding diffuse scattering (but they are "smooth" at L-band).

From the above results, the applicability of the 3-component decomposition analysis is clear. For polarimetric data containing different objects such as houses, canals, roads and low vegetation of rice plants, the

images can be classified based on the different scattering mechanisms. However, for the case of a single scattering mechanism, for example, forests, it becomes difficult to use the decomposition analysis as described in the following subsection.

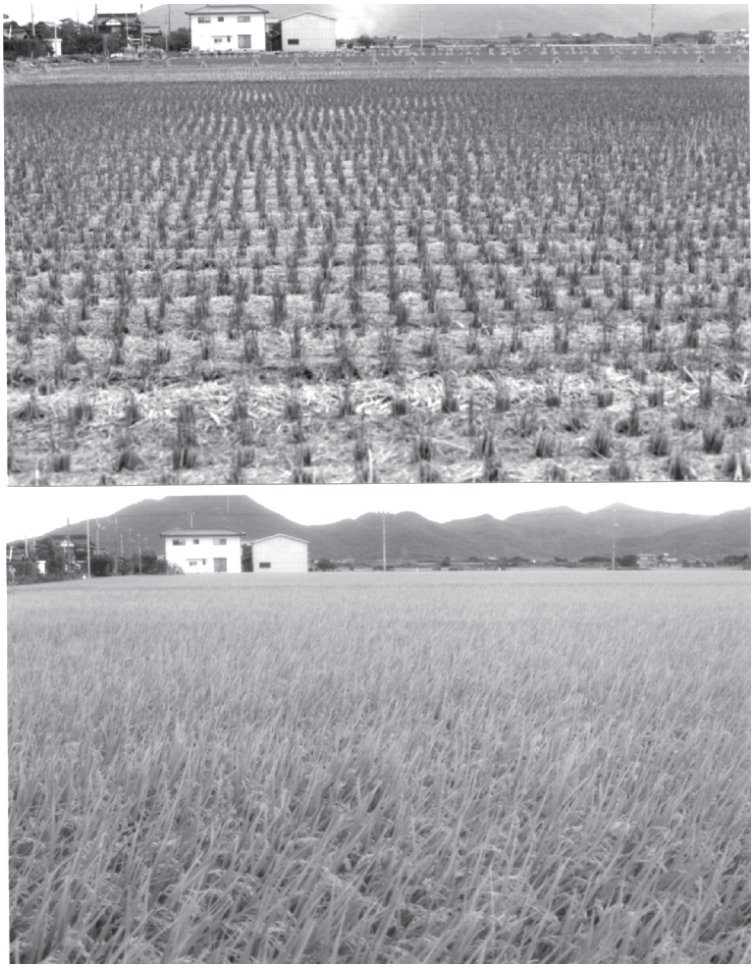

Figure 4.10: Regularly planted rice plants in the Kojima district. The upper image shows bunches of plants after harvesting. The lower image shows fully grown rice plants in the same field.

4.2.8 Application to Tomakomai Forests

The 3-component decomposition analysis is applied to the Pi-SAR L- and X-band data over the Tomakomai forests. Fig.4.11 shows the decomposition result of the L-band data shown in Fig.4.4. In the composite color image shown in Fig.4.11 and the right image of Fig.4.12, the double-bounce, volume and surface scattering mechanisms are represented by red, green and blue respectively. It can be seen from Fig.4.11 that the image appears green in most of the areas, indicating that the volume scattering is the dominating scattering mechanism for L-band data. The surfaces of clear-cut areas and roads are smooth in comparison with the

radar wavelength, and the backscattered energy is very little. Hence, both the intensity image and the decomposed image appear dark. There are 3 very bright point-like images in the dark clear-cut areas on the center right of Fig.4.11. These small areas appear as red in the decomposition analysis, they are corner reflectors.

The X-band color composite image and the decomposed image are shown in Fig.4.12. Color designation in these images is same as that in the L-band data. The size of the X-band image is smaller than that of the L-band image. It can be seen from the right image of Fig.4.12 that volume scattering is the dominant scattering mechanism in most of the areas, but some areas indicate surface scattering. The Pi-SAR images were acquired in November, so that the leaves of deciduous trees such as larch and broadleaf already had fallen, leaving only branches and trunks. The X-band microwave can then penetrate into the interior of forests, and volume or more precisely multiple scattering among branches (and/or trunks) occur. For non-deciduous trees, the X-band microwave cannot penetrate into the forests, and surface scattering is dominant in these forests. It appears, therefore, that although the decomposition analysis is not useful in extracting forest parameters of a same type, it may be possible to distinguish the difference between deciduous and non-deciduous forests from the X-band data in winter.

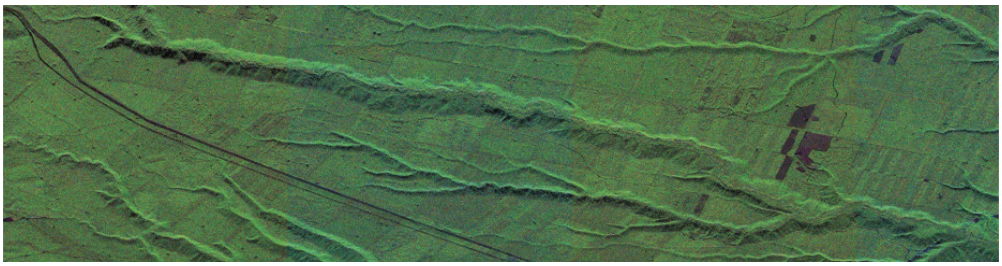

Figure 4.11: The 3-component decomposition analysis of L-band Pi-SAR image of the Tomakomai forests in Fig.[4.4], where the color is designated as "double : volume : surface = R : G : B".

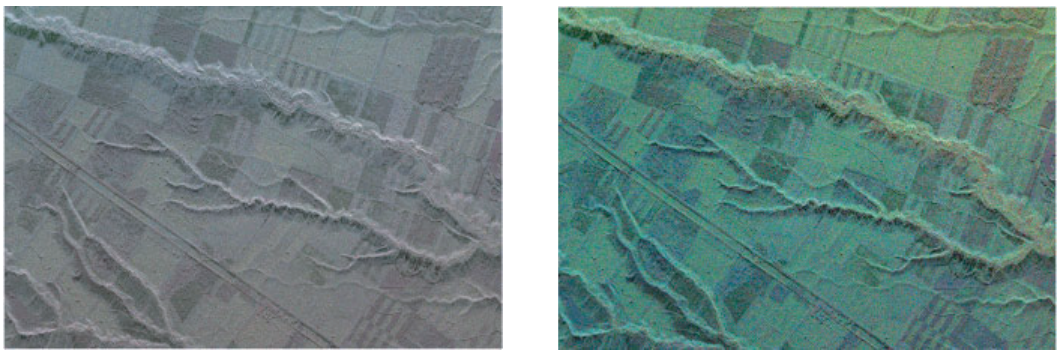

Figure 4.12: Pi-SAR X-band RGB image (left) and the decomposition result (right) of the Tomakomai forests. The HH-, HV- and VV-polarization images are represented by red, green and blue respectively in the left RGB image, and the color designation in the right image is same as Fig.[4.11].

4.3 Summary

A full polarimetric SAR has become very popular in recent years because the fully polarimetric data contain more information than the single polarization data. In this chapter, the basic theory of polarimetry, alpha-entropy analysis and 3-decomposition analysis are described. The polarimetric analysis is not the main theme of this thesis, but the technique can certainly be useful for classifying the different scattering mechanisms.

After summarising the principle of polarization, the α-entropy analysis is developed, based on the eigenvector analysis of coherence matrix. The α-entropy analysis is used to Pi-SAR data over the Tomakomai forests, but this technique is found to be not very useful to extract the physical parameters of forests. The three-component decomposition analysis is then introduced and used for the Pi-SAR data over the Okayama rice fields and Tomakomai forests. For the Okayama data, double bounce scattering is observed in some rice fields for L-band data, but X-band backscatter is dominated by the surface scattering. For the Tomakomai forests, volume scattering is the main scattering mechanism at L-band. Since X-band microwave can not penetrate deep inside the forests, X-band backscatter is dominated by surface scattering. Initially, we made the polarimetric approach to extracting forest information. In conclusion, we found that the polarimetric analyses are not useful to extract the quantitative values of the forest parameters such as biomass. However, there appear a new result that deciduous and non-deciduous forests may be classified using the 3-component analysis in polarimetric SAR data in winter.

Chapter 5

Applications to Forestry

The applications of non-Gaussian SAR speckle statistical properties to forestry are discussed in this chapter. The data used here is high-resolution polarimetric Pi-SAR images over the Tomakomai forests in Hokkaido, Japan. Before analyzing the data, the study areas description and the ground truth data collection are presented. The location of the study areas and the climate of Sapporo are briefly introduced, followed by the introduction of the main tree species in the study areas. Then, the approach of measuring ground truth data is presented, and the formulae of calculating tree biomass in Hokkaido and the calculated biomass results are given. The ground truth data include 2002, 2003 and 2005 measurements.

The quantitative relations between high-resolution Pi-SAR data and forest parameters are then investigated. The regression curve of forest biomass and the order parameter of K-distribution is derived, where the ground truth data collected in 2002 and 2003 are used. To evaluate the accuracy of this regression curve, the ground truth data collected in 2005 are used to compare with the model prediction. The regression is then updated by using all the ground truth data, and the updated regression is used to classify the biomass around the test sites. Finally, summary and further work are given.

5.1 Study Area Description

5.1.1 Location

The study areas are in Tomakomai located in Hokkaido, Japan. Hokkaido is in the northernmost part of Japan, extending from 139°20' E to 148°53' E, 41° 21' N to 45°33' N, and it is the largest island surrounded by the Sea of Ohotsk, the Japan Sea, and the Pacific Ocean, as shown in Fig.5.1. Further, Hokkaido is the largest prefecture of Japan, and its area is 83,452 km^2 (including 5,036 km^2 of the Northern Territories), accounting for 22% of Japan's total area.

Tomakomai is marked by red solid circle in Fig.5.1. The forests used for this study in Tomakomai are located in a part of the well-managed national forests. Fig.5.2 shows the 4-look Pi-SAR L-band image of a part of the Tomakomai national forests (scene center: 42°44' N, 141°30' E) acquired in November the 7th

2002. The incidence angles are respectively 38.4°, 44.1°, and 48.6° at the near-range, center, and far-range of Fig.5.2, and the image size is approximately 8.9 km in azimuth (from left to right) and 4.3 km in range (from bottom to top) directions. In the present analysis, the single-look images in full resolution of 3 (range) × 0.75 (azimuth) m are used. The multi-look image shown in Fig.5.2 is only for the purpose of visualization in a map scale. The marked areas in Fig.5.2 are the test sites where the ground truth data were measured in 2002 and 2004 [53].

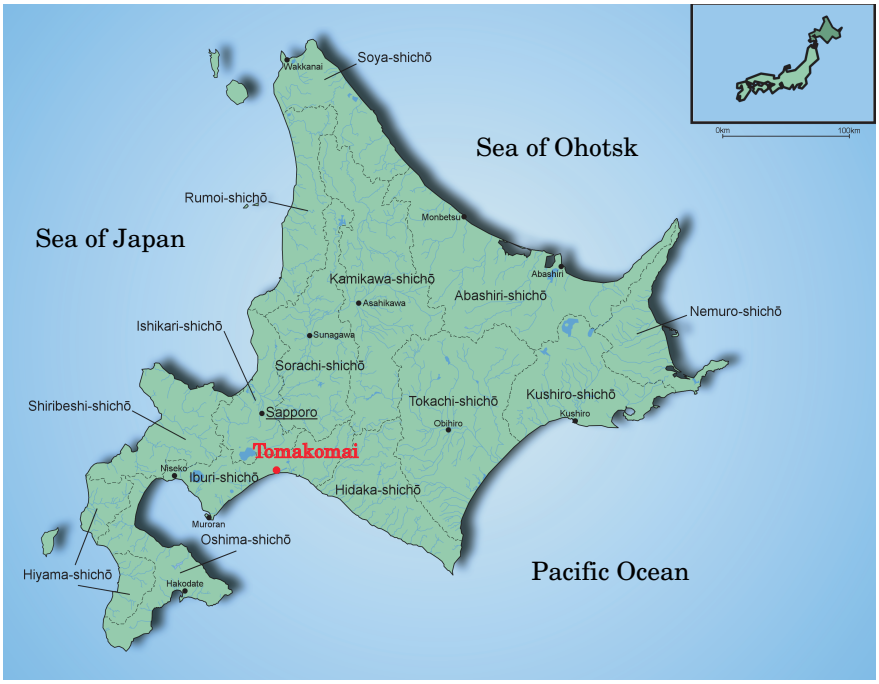

Figure 5.1: The map of Hokkaido which is the northernmost part of Japan and surrounded by Sea of Japan, Sea of Ohotsk and Pacific Ocean, and Tomakomai is marked by the red solid circle.

5.1.2 Climate

The climate of Hokkaido is located in the temperate zone and the sub-arctic zone. Though there is difference between each part of Hokkaido, the difference is not so large and Tomakomai is close to Sapporo, which is the capital of Hokkaido prefecture. Thus, the monthly average temperature, relative humidity, and rainfall of Sapporo from year 1961 to 1990 are given in Table 5.1. Due to the fact that it is the northernmost part of Japan, it is generally cooler in summer (20.2°C and 21.7°C in July and August, respectively) and cold, snowy and blustery in winter (-4.6°C average in January). It can be seen from Table 5.1 that the rainfall is abundant with annual average 1129.6mm, and the monthly average rainfall is over 90mm from August to the next year February, where August and September are the peak months of rainfall. Furthermore, the snow starts from middle of October to April with sub-freezing average temperatures from December to March,

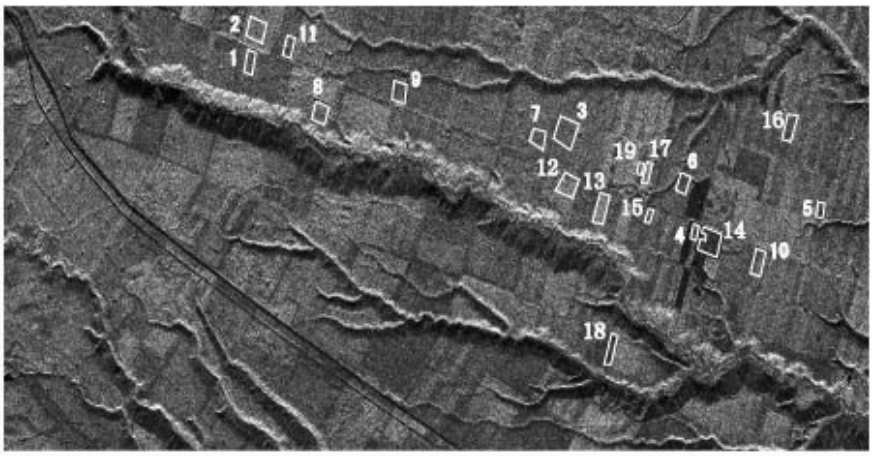

Figure 5.2: Pi-SAR L-band image of the Tomakomai forest acquired in November the 7th 2002, and 19 test sites as marked. The illuminating (range) direction is from bottom to top, and the flight (azimuth) direction is from left to right. Enlarged images of a part of each site are shown in Appendix C.

and the depth of the snow in Japan sea side may reach three meters. The average rainfall of November, December and January is 102mm, which also means that the snowfall is abundant. Table 5.1 also shows that the annual average relative humidity is 71%, which is not so high as in the other parts of Japan.

Table 5.1: Monthly average meteorologic parameters of Sapporo from year 1961 to 1990. (modified from [86]).

parameters	Jan.	Feb.	Mar.	Apr.	May	Jun.	Jul.	Aug.	Sept.	Oct.	Nov.	Dec.
temperature (°C)	-4.6	-4.0	-0.1	6.4	12.0	16.1	20.2	21.7	17.2	10.8	4.3	-1.4
relative humidity(%)	72	71	69	64	67	75	78	78	74	69	68	71
rainfall (mm)	107.6	94.1	81.8	62.3	54.8	66.4	68.7	142.0	137.7	115.6	98.5	100.1

5.2 Ground Truth Data

Ground truth data play a crucial role in relating remote sensed data to practical application. The ground truth data used in this thesis were collected in 2002, 2003, and in August and September of 2005. The biomass results are given in Table 5.3 and Table 5.4.

5.2.1 Tree Species

Due to cold weather and heavy snow lasting long time in Hokkaido, the conifer is the dominating tree species. The main conifer species are Japanese larch (in Japanese “karamatsu”), Todo-fir (in Japanese “todomatsu”),

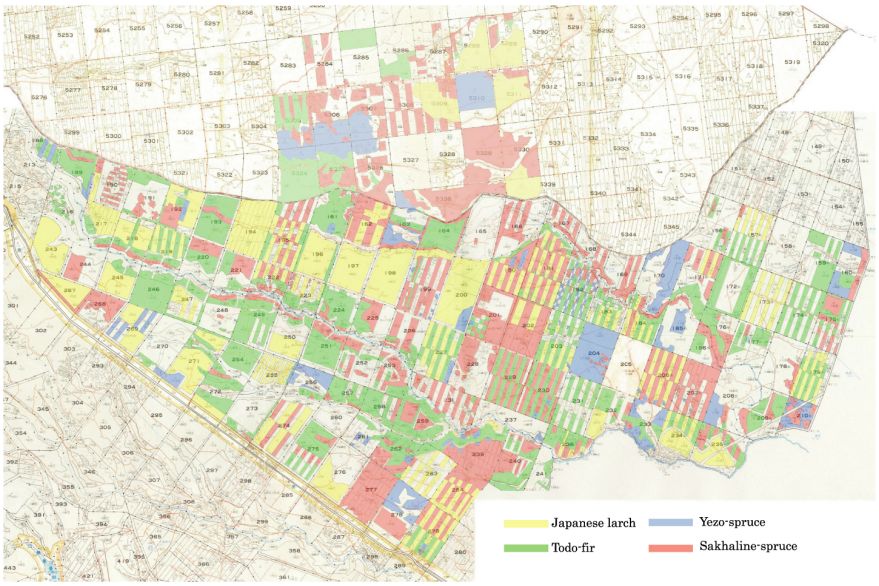

Figure 5.3: The map of compartments in the Tomakomai forests, showing planting times and tree species with yellow (Japanese larch), green (Todo-fir), blue (Yezo-spruce) and red (Sakhalin-spruce).

Figure 5.4: The pictures of Todo-fir and its leaves, trunk, flowers, and fruits [87].

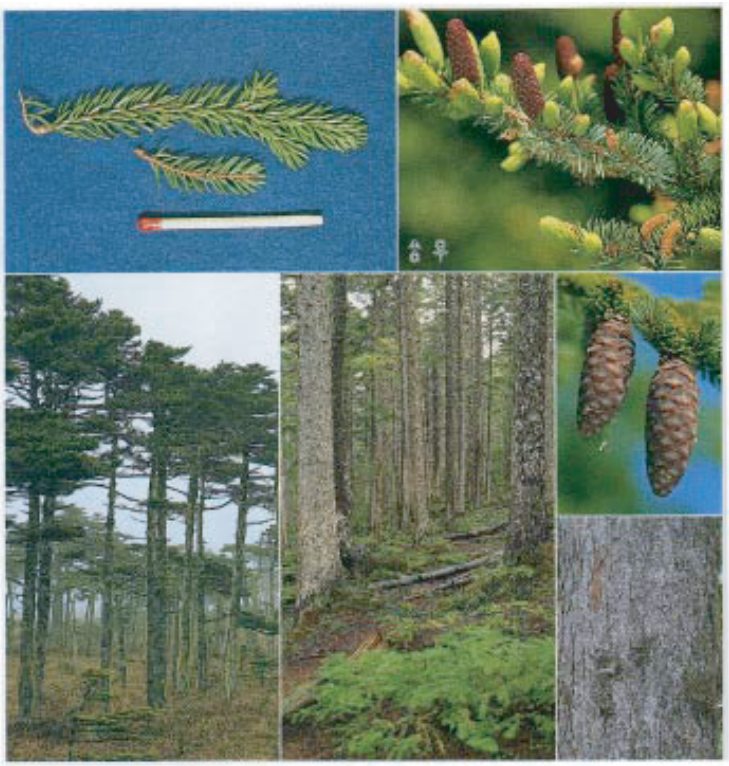

Figure 5.5: The pictures of Sakhalin-spruce and its leaves, trunk, flowers, and fruits [87].

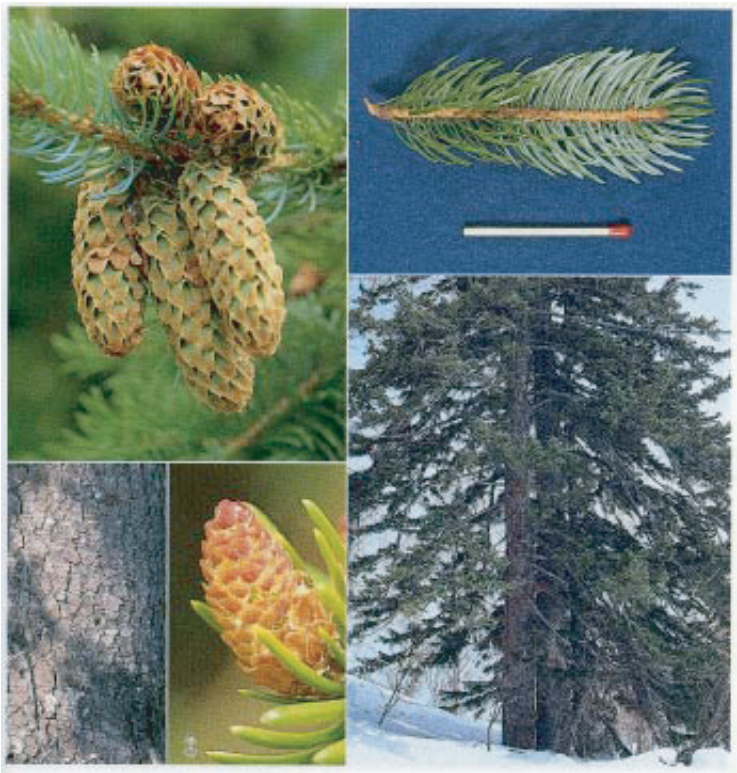

Figure 5.6: The pictures of Yezo-spruce and its leaves, trunk, flowers, and fruits [87].

Figure 5.7: The pictures of Japanese larch and its leaves, trunk, flowers, and fruits [87].

Table 5.2: Characteristics of main coniferous species in Tomakomai. (modified from [87]), where GBH means girth at the breast height; L is the length; W is the width; M means male, while F denotes female.

	Sakhalin/Todo-fir	Sakhalin-spruce	Yezo-spruce	Japanese larch
Japanese name	Todomatsu	Akaezomatsu	Ezomatsu	Karamatsu
general characteristics	evergreen, H: 20∼30m, GBH: 60∼100cm	evergreen, H: 30∼40m, GBH: 80∼100cm	evergreen, H: 30∼40m, GBH: 100∼150cm	deciduous, H: 20∼30m, GBH: 60∼100cm
leaf	L: 1.5∼3cm, W: 2∼3mm, bifurcate tip, reverse white stoma	L: 0.5∼1.2cm, W: about 1mm, rhombus cross section, sharp tip	L: 1∼2cm, W: 1.5∼2mm, flat cross section, two white stoma	L: 2∼4cm, W: about 2mm, 20∼40 leaves spiral cluster
trunk	hoary, smooth	deep brown, thin scale	dust color thin scale	dust color vertical crack
flower	M: oval, ≈7mm F: vertical, 2∼3cm	M: ≈1.5cm F: fuchsia, ≈3cm vertical	M: oval, 1.5∼2cm F: vertical, 2∼2.5cm, magenta	M: oval, adown F: vertical or horizontal
fruit	cylinder, L: 5∼8cm girth: 2∼3cm	column, L: 5∼8cm girth ≈ 2.5cm	column, L: 4∼8cm girth: 2∼3cm	oval, L: 2∼3cm

Sakhalin-spruce (in Japanese "akaezomatsu") and Yezo-spruce (in Japanese "ezomatsu") [87]. Fig.5.3 shows the map of compartments in the Tomakomai forests. In the map, the "age" (planting time) of trees are quoted, and yellow, green, blue, and red colors indicate Japanese larch, Todo-fir, Yezo-spruce and Sakhalin-spruce respectively. Fig.5.4-Fig.5.7 show the images of leaves, trunks, flowers, and fruits of these tree species. Moreover, Table 5.2 shows the general characteristics and common features of leaf, trunk, flower, and fruit of the four major species. The tree species can be distinguished from Fig.5.4-Fig.5.7 or from Table 5.2, and the summaries are given as follows.

- Todo-fir: leaves are soft and with two branches at the tip, and it can also be distinguished by the cortex.
- Sakhalin-spruce: leaves are short with rhombus-like cross section, and its trunk is in deep brown.
- Yezo-spruce: leaves are long compared to Sakhalin-spruce, and leaf cross section is flat. Trunks are in dust color.
- Japanese larch: leaves are 20∼40 pieces cluster together with spiral shape.

5.2.2 Ground Truth Data

The marked areas in Fig.5.2 are the test sites where the tree parameters including height, basal area and GBH were measured in 2002 and 2003, while the tree parameters in the 23 marked areas in Fig.5.8 were measured in August and September, 2005. At each test site, a sample stand of size 20 × 20m was selected, and all trees of diameter greater than 5 cm within the stand were measured. Further, in each sample stand, one sub-sample stand with the size of 10 × 10m was selected, and the number of branches, diameters and height of small trees of diameter less than 5 cm were measured. Soil moisture was also measured at the four corners of each stand, four points between corners and at the center.

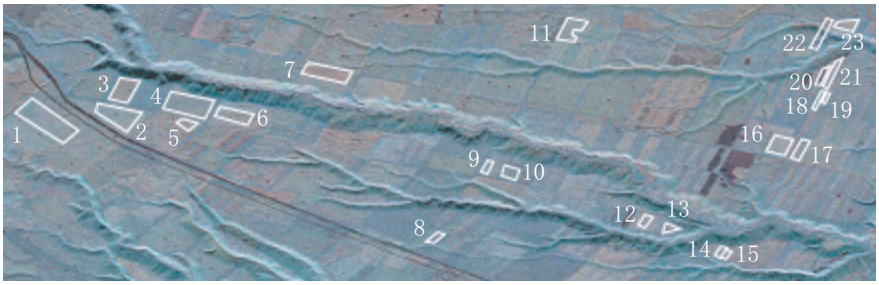

Figure 5.8: The marked areas are the 23 test sites measured in August and September, 2005, and the image was acquired in November 7th, 2002.

Fig.5.9 shows the measurement of tree height and GBH. Usually, one group consists of three people, and one measures the tree height by using the laser distance measure, and the other measures the GBH, while the 3rd person records the data. As can be seen from Fig.5.9, the true tree height is the sum of the measured height and the height of the person up to eyes. There is another traditional method to measure tree height from the distance to the trunk and the corresponding angle to the tree top. This method was used in the first half of data collection in August, 2005.

Figure 5.9: Measuring tree height and girth at the breast height. The laser distance measure shown in the right top corner is used to measure tree height.

5.2.3 Biomass Calculation

For computing the tree biomass, the GBH of each tree was first converted to the diameter at breast height (DBH). Then the trunk volume of each tree was calculated by using the empirical formulas derived for the forests in Tomakomai area [60]. The conversion formulas are given as follows.

For Yezo-spruce and Sakhalin-spruce:

$$\begin{aligned} \log V &= -4.0744 + 1.824080 \log DBH + 0.934568 \log H_t \quad (DBH < 50cm) \\ &= -4.5137 + 1.568947 \log DBH + 0.842787 \log H_t \quad (50cm \leq DBH) \end{aligned} \tag{5.1}$$

For Todo-fir:

$$\log V = -4.0971 + 1.681121 \log DBH + 1.131348 \log H_t \tag{5.2}$$

For Japanese larch and broadleaf tree:

$$\begin{aligned}
\log V &= -4.068644 + 1.756152 \log DBH + 0.906210 \log H_t \qquad (DBH < 10cm) \\
&= -4.335395 + 1.903051 \log DBH + 1.025410 \log H_t \quad (10cm \leq DBH < 20cm) \\
&= -4.441199 + 1.853014 \log DBH + 1.166956 \log H_t \quad (20cm \leq DBH < 30cm) \\
&= -4.332596 + 1.848675 \log DBH + 1.088954 \log H_t \qquad (30cm \leq DBH)
\end{aligned} \tag{5.3}$$

In these formulas, $V(m^3)$ is the trunk volume, and H_t denotes the tree height.

Table 5.3: Main tree species and average biomass of the test sites. Measurements at sites 1-12 were made in 2002, and those at sites 13-19 in 2003. The numbers in the brackets are the percentage of dominant species.

site	species	biomass	site	species	biomass
1	Japanese larch (75.4)	83.7	11	Japanese larch (94.0)	57.4
2	Yezo-spruce (97.9)	64.2	12	scots pine (98.0)	70.4
3	Japanese larch (86.0)	57.2	13	Sakhalin-spruce (73.3)	99.5
4	Todo-fir(55.2)	40.5	14	Sakhalin-spruce (100.0)	0.9
5	conifer	47.6	15	Japanese larch (72.2)	40.1
6	Japanese larch (83.4)	65.2	16	Sakhalin-spruce (89.9)	66.7
7	Japanese larch (95.9)	83.6	17	Sakhalin-spruce (100.0)	30.5
8	Sakhalin-spruce (94.2)	84.4	18	Sakhalin-spruce (100.0)	5.1
9	Todo-fir(90.0)	83.5	19	Sakhalin-spruce (100.0)	13.4
10	Sakhalin-spruce (63.9)	34.0		totoal	1027.9

To compute the above-ground tree volume, the calculated trunk volume V is multiplied by the expansion factor of 1.36 defined by the ratio of total above-ground biomass to the trunk biomass. Finally, the above-ground volume is converted to the above-ground biomass by using tree density of each species, and they are 0.391 g/cm^3 for Sakhalin-spruce, 0.314 g/cm^3 for Yezo-spruce, 0.329 g/cm^3 for Todo-fir, 0.444 g/cm^3 for Japanese larch, and 0.453 g/cm^3 for broadleaf trees. Furthermore, in the Tomakomai forests, the tree height increases 25 cm/year on average and the annual biomass increase is approximately 1.3 tons/ha. Thus, the final results were subtracted 3.9 tons/ha from the 2005 measurements to yield the biomass at the time of Pi-SAR data acquisition in 2002.

Table 5.3 shows the tree species and calculated biomass results of the 2002 and 2003 measurements, where the 2003 data are the measured data subtracted annual average biomass increment 1.3 tons/ha, and

Table 5.4: Ground truth data collected in August and September, 2005.

site	species	biomass	site	species	biomass
1	Japanese larch	50.8	13	Sakhalin-spruce	36.5
2	Japanese larch	107.9	14	Sakhalin-spruce	79.3
3	Sakhalin-spruce	85.6	15	Sakhalin-spruce	97.2
4	Japanese larch	111.8	16	Sakhalin-spruce	97.4
5	Sakhalin-spruce	71.9	17	conifer	52.4
6	Todo-fir	43.8	18	Japanese larch	121.0
7	Sakhalin-spruce	161.3	19	Sakhalin-spruce	66.8
8	Sakhalin-spruce	67.5	20	Yezo-spruce	0.1
9	Todo-fir	71.6	21	Sakhalin-spruce	56.9
10	Todo-fir	79.6	22	Sakhalin-spruce	46.1
11	Sakhalin-spruce	126.7	23	Sakhalin-spruce	125.3
12	Sakhalin-spruce	97.5		totoal	1855.1

the percentage of the main tree type in each test site is also given. Table 5.4 gives the results of the ground truth collection in August and September, 2005.

5.3 RCS and Forest Parameters

5.3.1 RCS and Tree Biomass

The relation between RCS and forest parameters have been reported by several authors, and the results show that the RCS increases with forest biomass and saturates at certain biomass values. The saturation levels change with tree species and radar wavelength [44], [45], [48]. Dobson *et.al.* [44] show that for coniferous forests the RCS saturation levels at L- and P-bands are in the regions of 100 and 200 tons/ha respectively at radar incidence angles of 40°-50°, and Imhoff [48] indicates the saturation levels of 20, 40 and 100 tons/ha at C-, L- and P-bands respectively for both the Hawaii broadleaf forests and combined forests of conifer and broadleaf.

The RCS is first estimated as a function of tree biomass as shown in Fig.5.10 for the X- and L-bands data. Despite the limited number of test sites, a clear trend can be observed. At X-band, the RCS is largest for VV-polarization followed by HH- and HV-polarizations. The solid lines are the regression curves fitted using third-order polynomial to the corresponding data. The correlation coefficients are -0.02, 0.32 and 0.36 for the HH-, VV- and HV-polarizations respectively. At L-band the RCS is largest for HH-polarization followed by VV- and HV-polarizations, and the corresponding correlation coefficients are 0.52, 0.79 and 0.82 respectively. The X-band RCS does not show strong correlation with biomass at all polarizations. While the L-band RCS has higher correlation, in particular, at HV-polarization with steady increase in RCS with

biomass up to certain levels. These trends are in agreement with some previous results [41], [44], [45], [48]. There are no clear biomass saturation levels at X-band, but the L-band saturation level may be defined approximately as 40 tons/ha for the Pi-SAR data of the Tomakomai forests [54]. The forest biomass beyond this saturation limit cannot be estimated from the RCS values.

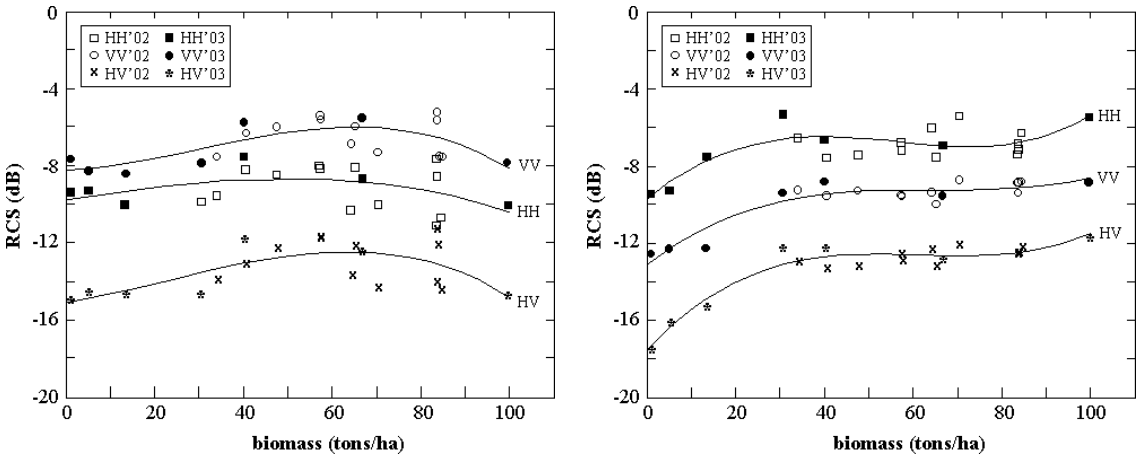

Figure 5.10: The RCS as a function of forest biomass for X-band (left graph) and L-band (right graph) data. The curves are fitted using third-order polynomial to the corresponding polarization data points.

5.3.2 RCS and Tree Age

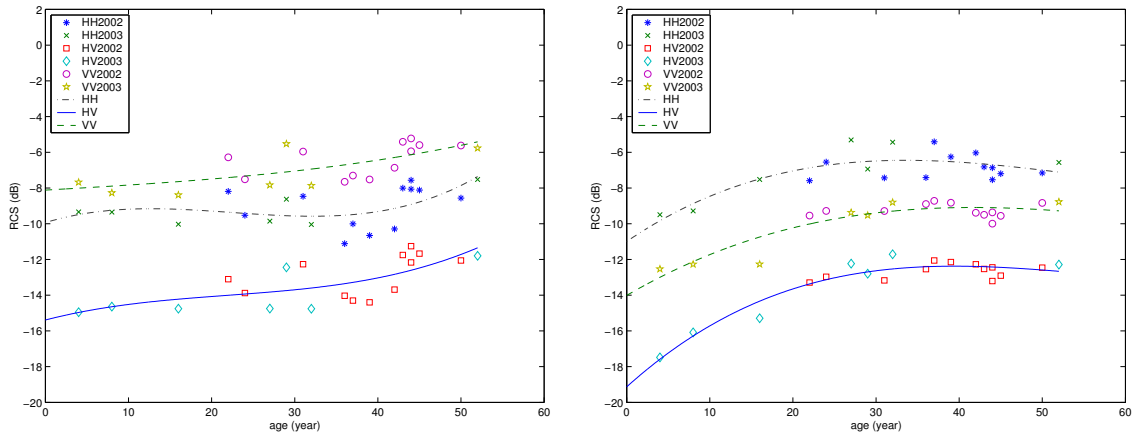

Figure 5.11: The RCS as a function of forest age for X-band (left graph) and L-band (right graph) data. The curves are fitted using third-order polynomial to the corresponding polarization data points.

The RCS is also estimated as a function of tree age as shown in Fig.5.11 for the X-band and L-band data. Third order polynomial fitting is also used here. At X-band, the correlation coefficients are 0.55, 0.68 and 0.72 for HH-, VV- and HV-polarizations respectively, showing no clear trend for X-band data. At L-band, the RCS increases with the tree age up to about 30 years old, and beyond this age the RCS saturates.

The correlation coefficient for HH-, VV- and HV-polarizations are 0.79, 0.89 and 0.95, respectively. Again, L-band data show stronger correlation than X-band data, and HV-polarization has the highest correlation coefficient at both X- and L-bands. Thus, age of trees can be estimated from L-band RCS at HV-polarization up to around 30 years old with certain accuracy.

5.3.3 RCS and Basal Area

The relations of X- and L-band RCS and basal area are shown in Fig.5.12, and the data are also fitted using third order polynomial. The correlation coefficients are 0.57, 0.58, and 0.62 for X-band HH-, VV- and HV-polarizations respectively, and the corresponding L-band correlation coefficients are 0.77, 0.94 and 0.95 respectively. L-band data again show stronger correlation with the saturation level at around $30\text{m}^2/\text{ha}$.

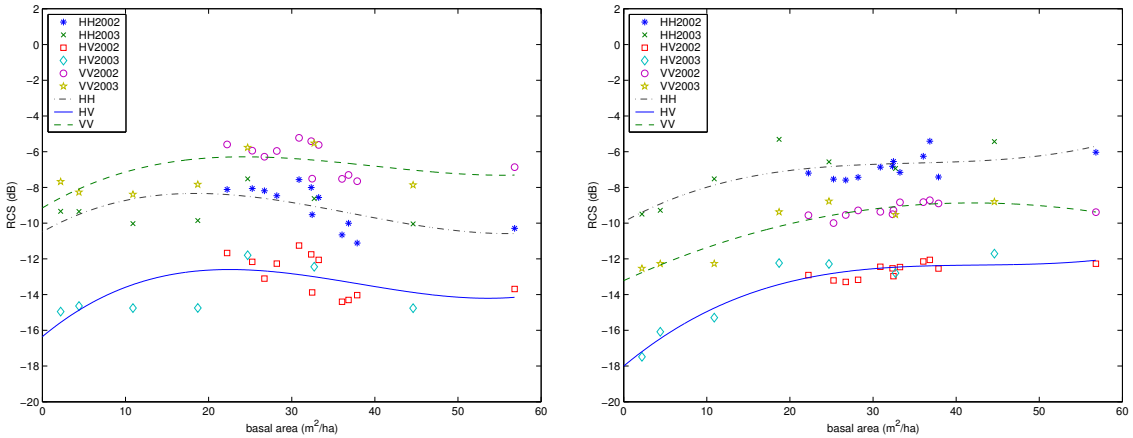

Figure 5.12: The RCS as a function of the basal area for X-band (left graph) and L-band (right graph) data. The curves are fitted using third-order polynomial to the corresponding polarization data points.

5.3.4 RCS and Tree Height

Fig.5.13 shows the relations of X- and L-band RCS and mean tree height with the regression curves fitted using third order polynomial. At X-band, the correlation coefficients are 0.20, 0.40 and 0.47 for HH-, VV- and HV-polarizations, and at L-band the corresponding correlation coefficients are 0.64, 0.76 and 0.83. Yet again, L-band data have higher correlations and HV-polarization dataset correlates best for both bands. The saturation level of L-band data can be defined approximately as 8 m for all polarizations.

5.3.5 The Limitations of RCS and X-band Data

As can be seen from the above relations between RCS and forest parameters, X-band data do not have strong correlations, for the reason that X-band microwave cannot penetrate the interior of forests and backscattering

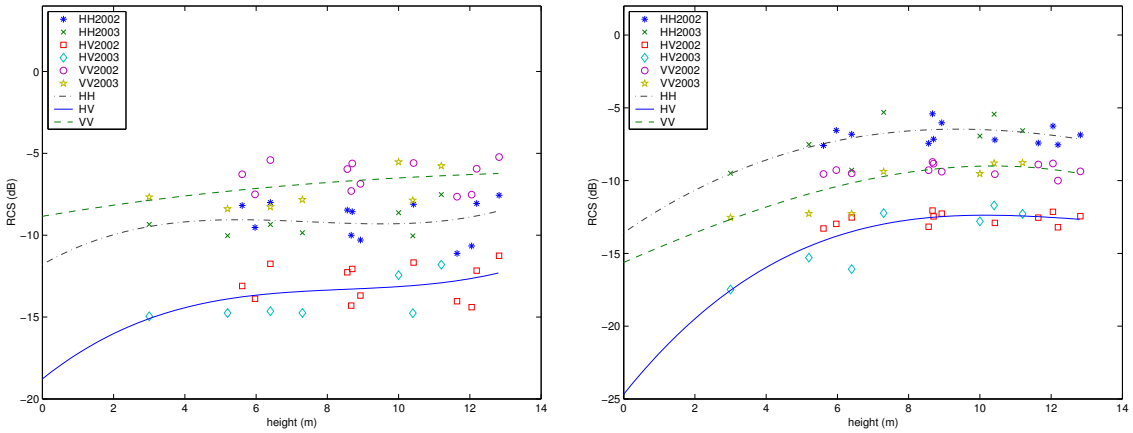

Figure 5.13: The RCS as a function of mean forest height for X-band (left graph) and L-band (right graph) data. The curves are fitted using third-order polynomial to the corresponding polarization data points.

is dominated by surface scattering from the crown part of trees. An evidence of surface scattering from the Tomakomai forests is already shown by the 3-component decomposition analysis of polarimetric data shown in Fig.4.12. The surface of tree crowns are rough for X-band microwave, and therefore the RCS does not depend strongly on the tree parameters.

There is a certain trend of increasing RCS at L-band with increasing values of all tree parameters. Unlike X-band microwave, L-band microwave with longer penetration depth can enter into the interior of forests, and therefore volume scattering dominates as proven by the decomposition analysis shown in Fig.4.11. With increasing tree biomass, the forests become dense, and surface scattering become dominant at the saturation level. Thus, beyond this saturation limit the forest parameters cannot be retrieved from the RCS data. Since the L-band data contain more information on the forests as compared with X-band data [54], only the L-band polarimetric data are used for statistical analysis in this thesis.

5.4 Texture Analysis

As mentioned before, a high-resolution SAR can resolve targets characteristics to some extent. Reflecting the structure of forests, for example, the SAR images of forests appear "textured", *i.e.*, the images show fluctuations associated with tree structures, and the scales of fluctuations are longer than the SAR resolution cell as illustrated in the Pi-SAR image of the Tottori dune in Fig.1.5. The utilization of texture information for forest information extraction has previously been suggested by several authors [16], [24], [27], [28], [57], [58]. However, no detailed analysis has been reported to show the quantitative relation between the parameters of texture and ground-truth data as reported in this thesis.

In Chapter 2, both Gaussian and non-Gaussian models were introduced, and texture can be described

by non-Gaussian models. When the dataset is fitted by the models, it is necessary to select a model to fit best to the data. In this thesis, the Akaike information criterion (AIC) [17], [79], [88] is used to select the best fitted model.

5.4.1 Model Selection by AIC

For a given model, AIC is defined by [88]

$$AIC = -2 \times (maximum\ logarithmic\ likelihood) + 2 \times (number\ of\ free\ parameters) \tag{5.4}$$

The model which minimizes the AIC (MAICE) is regarded as the optimal one to fit a given dataset.

Equation (5.4) is applied to the Rayleigh, log-normal, Weibull and *K*-distributions for all the polarization data of all the selected test sites, and the results are shown in Table 5.5-Table 5.7.

Table 5.5 shows the AIC results of HH-polarization data. The AIC values of *K*-distribution are the smallest in each test site group, that is, *K*-distribution is the best model among 4 models for HH-polarization datasets of all test sites. The AIC results of Weibull distribution are close to those of *K*-distribution, followed by the Rayleigh distribution. The log-normal distribution does not fit the data.

Table 5.6 and Table 5.7 show the AIC results of VV- and HV-polarizations data, respectively. It can be seen from both tables that the *K*-distribution is the optimum PDF in 18 of 19 test sites, and the Weibull distribution only fits best to the data of test site 4. Again, the log-normal distribution does not fit the datasets. The differences of AIC between the Weibull distribution and *K*-distribution are not large for several datasets, such as test site 6, 11 and 15.

Fig.5.14 shows an example, where the PDF of the test site 6 is plotted as a function of image amplitude normalized by the mean. The upper left, upper right and lower graphs correspond respectively to the HH-, VV- and HV-polarizations, and the scale of the vertical axes is the (natural) logarithm of relative number of pixels. As can be seen, the difference of the PDFs lies in their tail parts [30]. It can be seen from Fig.5.14 that the *K*-distribution fits best to the data. However, it should be emphasized that the Weibull distribution also shows good fit as can be seen in Fig.5.14. These results are in agreement with the results of AIC analysis.

5.5 *K*-Distribution and Forest Parameters

As shown in the preceding section, the *K*-distribution is the best model among the 4 models considered in the study for all the polarization datasets, and therefore, only the parameter of *K*-distribution is related

Table 5.5: AIC results of Rayleigh, log-normal, Weibull and K-distributions of HH-polarization

	probability density functions					probability density functions			
site	Rayleigh	log-normal	Weibull	K	site	Rayleigh	log-normal	Weibull	K
1	18507	20205	18446	18396	11	11281	11985	11155	11067
2	30006	33172	29963	29927	12	8634	9222	8578	8534
3	21346	23573	21258	21235	13	17255	18964	17226	17285
4	6127	6520	6027	6004	14	37018	38874	36466	36139
5	7229	7743	7138	7111	15	4255	4623	4257	4230
6	13079	13968	13006	12932	16	6321	6915	6315	6287
7	19081	21060	19028	19018	17	5283	5778	5274	5296
8	16776	18216	16735	16669	18	9100	9568	9006	8925
9	13598	15020	13558	13538	19	3678	3897	3632	3604
10	17948	19055	17778	17653					

Table 5.6: AIC results of Rayleigh, log-normal, Weibull and K-distributions of VV-polarization

	probability density functions					probability density functions			
site	Rayleigh	log-normal	Weibull	K	site	Rayleigh	log-normal	Weibull	K
1	18074	19974	18055	18021	11	10816	11796	10774	10741
2	30092	33502	30034	30009	12	8238	9147	8229	8227
3	21360	23178	21289	21227	13	17089	18851	17075	17053
4	6049	6599	5970	5985	14	34291	37457	34227	34127
5	7274	7716	7179	7157	15	4311	4750	4304	4296
6	12662	13931	12633	12614	16	6340	6902	6335	6324
7	19037	21006	18990	18987	17	5487	6028	5441	5435
8	16662	18351	16623	16601	18	8742	9510	8702	8669
9	13443	14734	13427	13400	19	3485	3702	3484	3446
10	16951	18448	16935	16870					

Table 5.7: AIC results of Rayleigh, log-normal, Weibull and K-distributions of HV-polarization

	probability density functions					probability density functions			
site	Rayleigh	log-normal	Weibull	K	site	Rayleigh	log-normal	Weibull	K
1	18035	19822	18026	18000	11	10762	11769	10728	10713
2	30179	33290	30121	30096	12	8394	9126	8371	8332
3	21227	23127	21170	21103	13	17113	19074	17093	17088
4	5989	6693	5929	5950	14	37348	38931	36723	36352
5	7048	7578	7000	6970	15	4451	4807	4425	4410
6	12864	14183	12806	12798	16	6245	6837	6247	6225
7	18939	20889	18901	18873	17	5393	5897	5364	5345
8	16531	18217	16507	16478	18	9052	9507	8971	8868
9	13497	14849	13472	13449	19	3701	3810	3662	3611
10	17491	18877	17399	17314					

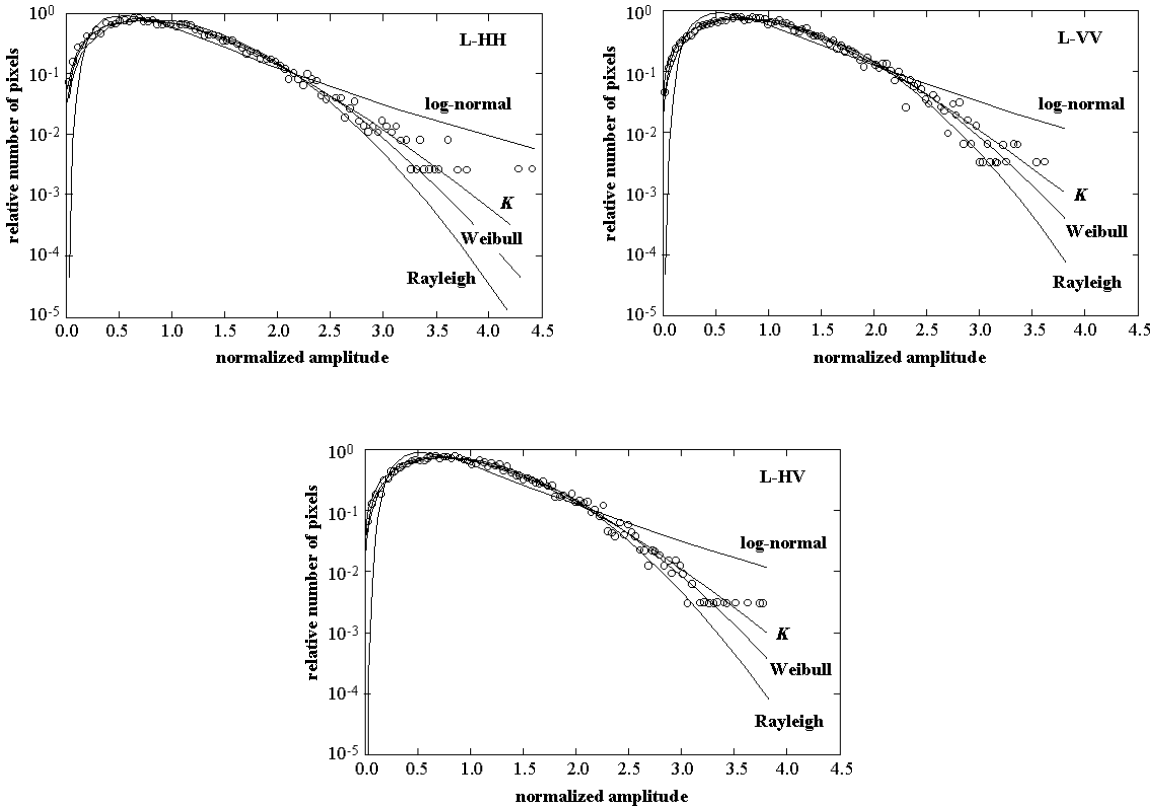

Figure 5.14: The estimated PDFs of L-HH (upper left graph), L-VV (upper right graph) and L-HV (bottom graph) image amplitudes of the test site 6 as a function of the amplitude normalized by the mean. The vertical axis is the relative number of pixels in the logarithmic scale. The PDF which fits best to the data is sought among the Rayleigh, log-normal, Weibull and K-distributions.

to the forest parameters here. A mention should be made that the reason why the Weibull distribution is not considered is because the Weibull distribution has two parameters and they only vary in a small range. Nevertheless, this can be an interesting future research subject.

In Chapter 2, the approaches to estimate the model parameters, including the Weibull and K-distributions, were given. In this thesis, the moment method is used to estimate the order parameter of the K-distribution. The nth moment of the K-distribution given by equation (2.30) for single-look data can be written as

$$\frac{\langle I^n \rangle}{\langle I \rangle^n} = \frac{n!\,\Gamma(n+\nu)}{\nu^n \Gamma(\nu)} \tag{5.5}$$

The bias and variance of the estimated ν need to be considered when K-distributed texture is described. The most convenient way to present the results is in the form of relative bias and variance of equation (5.5) when n is equal to 2. The relative bias and variance are given respectively by [16]

$$\frac{\langle \Delta\nu \rangle}{\nu} = \frac{\nu}{N}\left(1+\frac{1}{\nu}\right)\left(1+\frac{6}{\nu}\right) \tag{5.6}$$

and

$$\frac{\langle \delta\nu^2 \rangle}{\nu^2} = \frac{\nu^2}{N}\left(1+\frac{1}{\nu}\right)\left(1+\frac{4}{\nu}\right)\left(1+\frac{5}{\nu}\right) \tag{5.7}$$

Since there are a large number of image pixels in each test site, both the relative bias and variance take very small values. For the errors or uncertainties of estimates, the square root of $\langle \delta\nu^2 \rangle$ is used for the error bar in the regression curve shown in Fig.5.17.

5.5.1 Order Parameter and Biomass

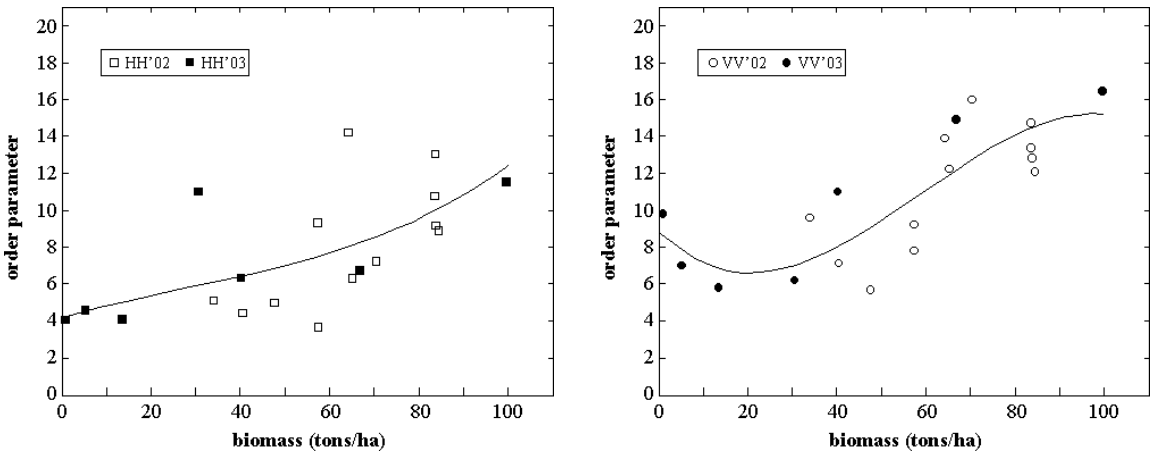

Figure 5.15: Order parameter of K-distribution as a function of tree biomass for the HH- (left) and VV- (right) polarizations data. The correlation coefficient is 0.64 and 0.75, respectively. The lines are fitted by third-order polynomial to the corresponding data points.

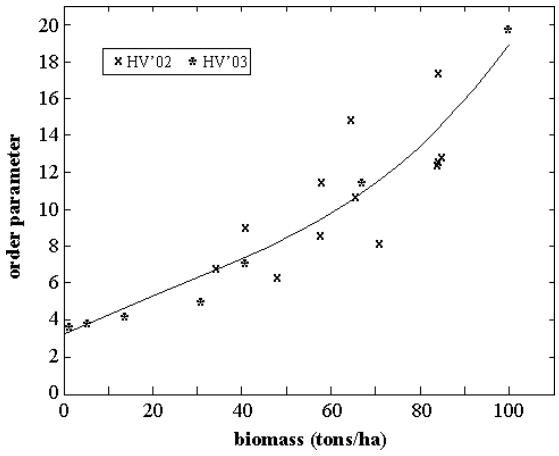

Figure 5.16: Order parameter of K-distribution as a function of tree biomass for the HV-polarization data. The correlation coefficient is 0.89. The lines are fitted by third-order polynomial to the corresponding data points.

Fig.5.15 and Fig.5.16 illustrate the order parameter of the K-distribution as a function of tree biomass

for the L-band co- and cross-polarization data. As can be seen from the figures, the general trend is that the order parameter increases with increasing biomass for all polarization data. The HH-polarization data in Fig.5.15 are rather scattered, and the VV-polarization data are less scattered. The correlation coefficients for the HH- and VV-polarization data are 0.64 and 0.75 respectively.

The best relation between the order parameter of the K-distribution and the tree biomass can be seen in the HV-polarization data in Fig.5.16 with the correlation coefficient of 0.89. A significant feature of Fig.5.16 is that the order parameter increases with biomass well beyond the RCS saturation limit keeping high correlation. As can be seen in the right graph of Fig.5.10, RCS saturates at about 40 tons/ha for the L-band co- and cross-polarization data. While, the order parameter shown in Fig.5.16 increases to approximately 100 tons/ha and possibly beyond. Thus, the order parameter of the K-distribution for high-resolution SAR images, in particular cross-polarization images, of forests can be an effective parameter to estimate the tree biomass in a wide range of values. Another advantage of using the order parameter is that it does not require absolute RCS values since the statistical distribution depends on the amplitude relative to the mean. The disadvantage is that the approach based on the non-Gaussian statistics requires high-resolution SAR images. As the size of SAR resolution cell increases, it becomes difficult to image fine features of forests, and the amplitude statistics tend to become Gaussian. The order parameters and regression curves computed in Fig.5.15 and Fig.5.16 are certainly dependent on the SAR resolution as well as the tree biomass (and species), but their dependence on resolution is not known at this stage.

The order parameter of the K-distribution in the cross-polarization data has higher correlation with the tree biomass than the co-polarization data, because the L-band microwave with relatively long wavelengths can penetrates into the interior of forests, and substantial amount of backscatter is caused by multiple (volume) scattering by branches and trunks. The high sensitivity of the cross-polarization data to the forest parameters, particularly biomass, has also been known for some time [40], [43], [45], [50]. The cross-polarized backscatter at L-band comes from the volume scattering by multiple reflection, giving rise to strong dependence on the associated forest biomass. Accordingly, the order parameter of the K-distribution is more sensitive to the forest biomass at HV-polarization than co-polarization data.

Fig.5.17 is same as Fig.5.16 but for two different tree species. Errorbars are added to show the confidence of estimates and also because only the regression model based on the HV-polarization data is used for estimating the biomass of other plots. In the figure, Sakhalin-spruce is represented by black circles, and crosses correspond to other conifers. It can be seen from Fig.5.17 that the order parameters for the single species of Sakhalin -spruce is less scattered than for the mixed species of conifers. For Sakhalin-spruce alone, a higher correlation coefficient of 0.92 is obtained. It appears, therefore, the species and structural difference

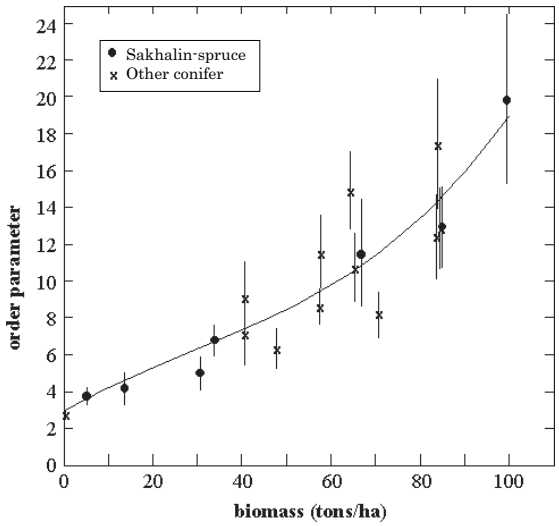

Figure 5.17: Order parameter of *K*-distribution as a function of forest biomass for the HV-polarization data. The correlation coefficient is 0.89. The black circles are the order parameters of Sakhalin-spruce forests. The correlation coefficient is 0.92. Third-order polynomial is used to fit the regression curve.

are the important factors in radar backscatter from coniferous forests, and they may well be the source of uncertainties in the regression curve.

The regression curve shown in Fig.5.17 takes a form

$$\nu = a_0 + a_1 B + a_2 B^2 + a_3 B^3 \tag{5.8}$$

where a_j $(j = 0, 1, 2, 3)$ are found to be 3.1574, 0.1248, -0.0011 and 1.4124×10^{-5}, respectively. ν is order parameter, and B denotes biomass.

5.5.2 Order Parameter and Tree Age

Fig.5.18 shows the scatter diagram of the order parameters of HH-, VV- and HV-polarizations data and the tree age of each test sites (the regression curves are again fitted using third-order polynomial) with the correlation coefficient 0.60, 0.58 and 0.65 respectively. The HV-polarization data has the highest correlation coefficient among all the datasets. However, the results shown here are quite scattered.

5.5.3 Order Parameter and Basal Area

Fig.5.19 is the scatter diagrams for the order parameter of HH-, VV-, and HV-polarizations data as a function of basal area with the correlation coefficients 0.71, 0.79 and 0.78 respectively. The VV- and HV-polarization data have higher correlation coefficients than the HH-polarization.

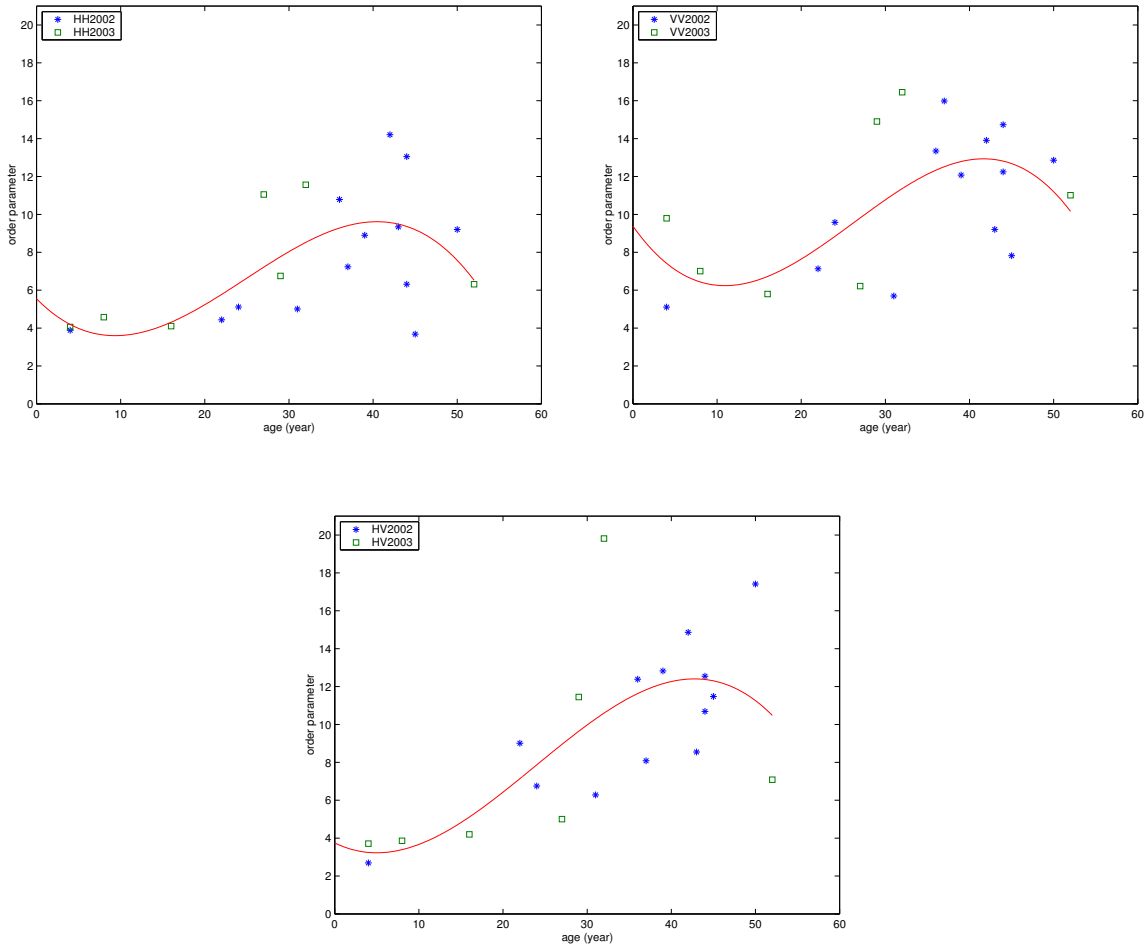

Figure 5.18: Order parameter of K-distribution as a function of tree age for the HH- (upper left graph), VV- (upper right graph), and HV- (bottom graph) polarizations data. The correlation coefficients are respectively 0.60, 0.58 and 0.65. The lines are fitted by third-order polynomial to the corresponding data points.

It can also be seen that Fig.5.19 is less scattered than Fig.5.18. This may be because the basal area is strongly correlated with forest biomass which shows the highest correlation coefficient among all forest parameters.

5.5.4 Order Parameter and Tree Height

Fig.5.20 shows the relations of order parameter of HH-, VV-, and HV-polarizations data and mean tree height with the corresponding correlation coefficients 0.49, 0.64 and 0.66 respectively. Again, the HV-polarization data has the highest correlation coefficient. Since the tree height dose not contribute much to the RCS fluctuation, it is not surprising that the order parameter does not correlate strongly with the mean tree height.

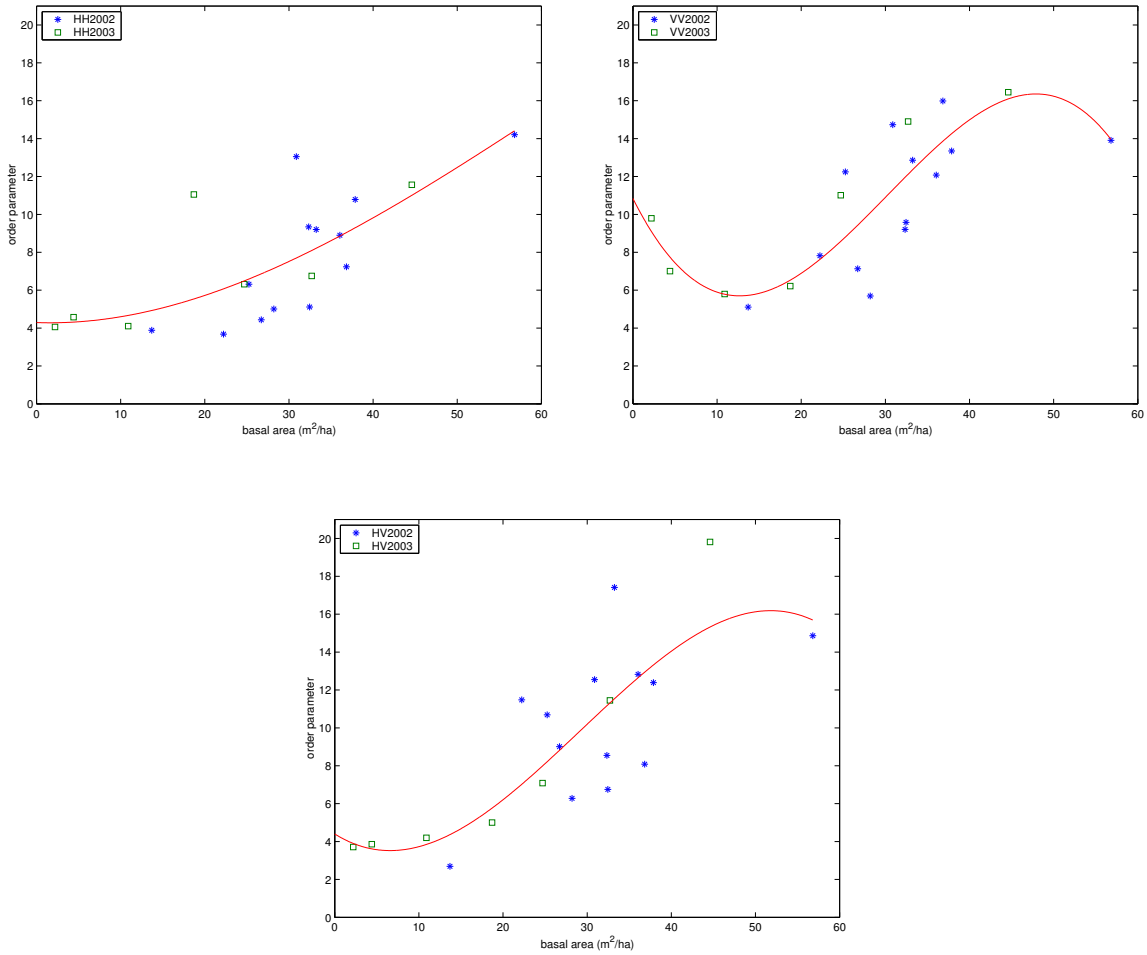

Figure 5.19: Order parameter of K-distribution as a function of basal area for the HH- (upper left graph), VV- (upper right graph), and HV- (bottom graph) polarizations data. The correlation coefficients are respectively 0.71, 0.79 and 0.78. The lines are fitted by third-order polynomial to the corresponding data points.

Summary of the Section

The relations of order parameter of K-distribution and forest biomass were investigated in this section. The results show that the order parameter correlates best with the forest biomass for HV-polarization dataset, and it does not saturate as the tree biomass increases. It can be said that the regression curve shown in Fig.5.17 can be used to estimate the forest biomass beyond the RCS saturation level.

5.6 Interpretation of Order Parameter and Biomass

Fig.5.21 illustrates the scattering mechanisms from forests at X-, C-, L- and P-bands, where surface scattering is the dominant contribution to the radar backscatter at X/C-bands, while various contributions are considered to arise from forest interior at L/P-bands. It has been known that longer wavelengths can

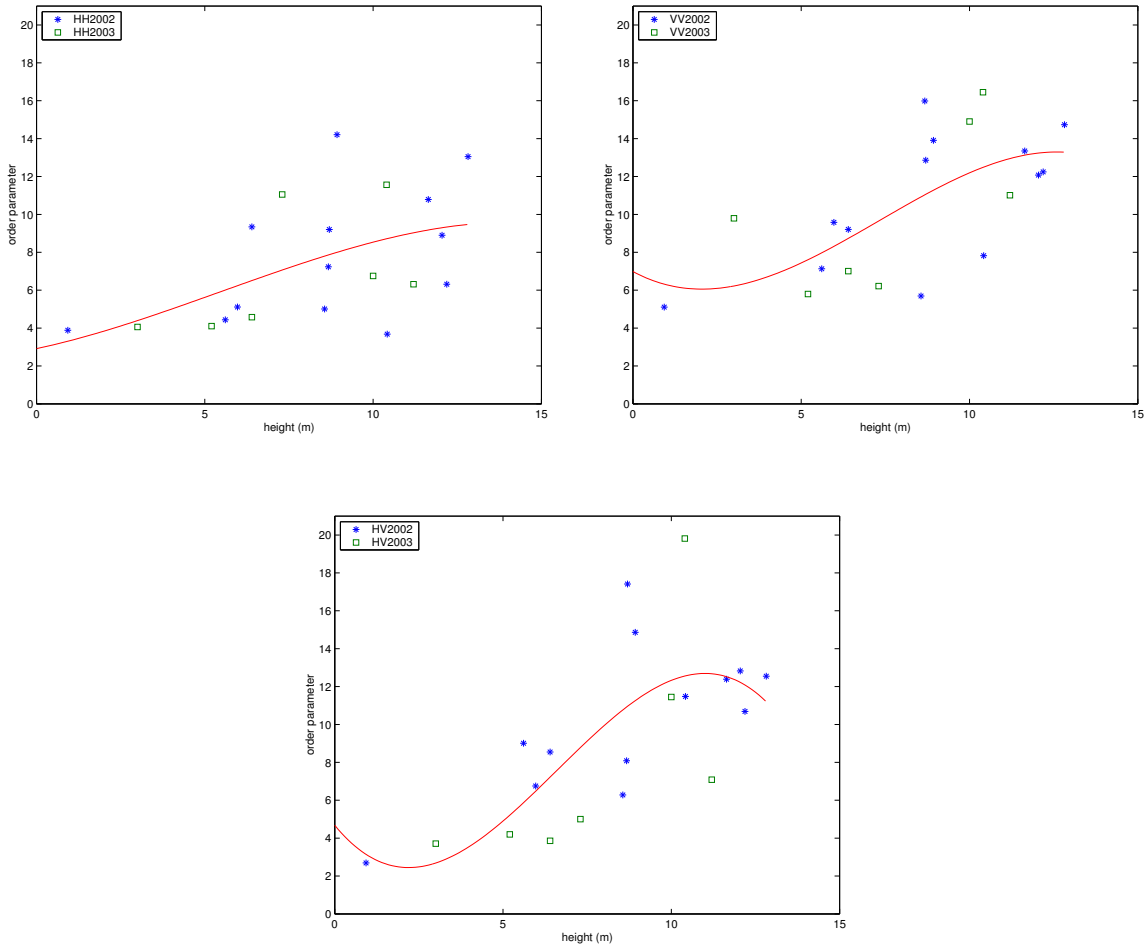

Figure 5.20: Order parameter of K-distribution as a function of mean tree height for the HH- (upper left graph), VV- (upper right graph), and HV- (bottom graph) polarizations data. The correlation coefficients are respectively 0.49, 0.64 and 0.66. The lines are fitted by third-order polynomial to the corresponding data points.

penetrate deeper in forests [39]-[41], [44]-[46], [48], [49]. At L-band, the incident microwave penetrates into the interior of forests, and the dominant radar backscatter is due to volume scattering from branches in the crown layer, multiple reflection from the ground to trunks and to branches, and surface scattering from ground [38], [41], [42], [45]. In the limit of zero biomass shown in Fig.5.22 (a), the dominant backscatter is due to the surface scattering from soil or small vegetation. If there is no undergrowth, and the surface is rough and statistically homogeneous, then the image constitutes a well known Gaussian speckle pattern which is described by the Rayleigh distribution, or the K-distribution of very large order parameters. It is expected, therefore, that the order parameter would increase as the biomass becomes very small in Fig.5.17, in particular for the lowest two biomass data. However, the surface was not statistically homogeneous at the time of data acquisition described as follows.

The two data points of low biomass of 0.9 and 5.1 tons/ha in Fig.5.17 correspond to the stands 14 and

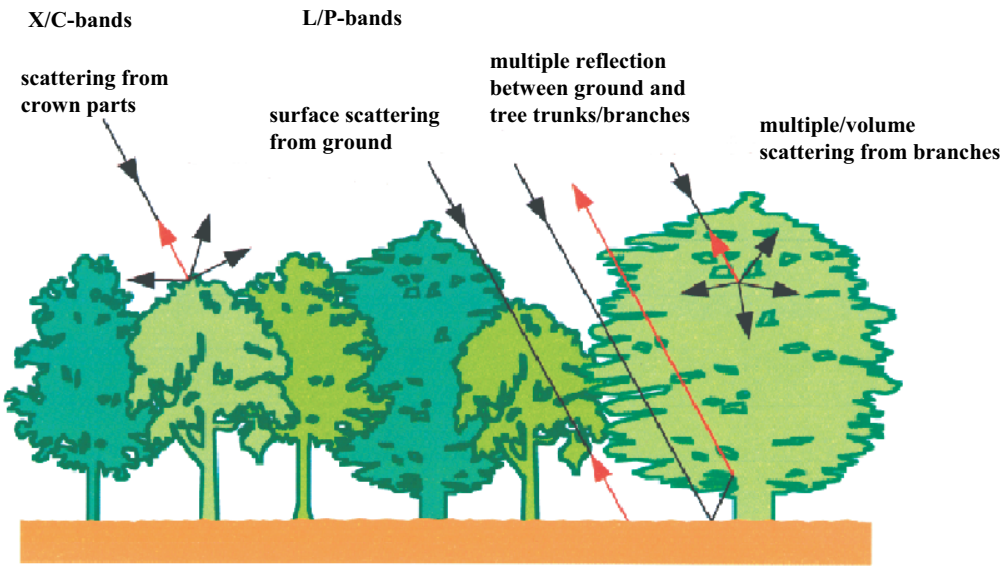

Figure 5.21: Illustration of scattering mechanisms from forests for X/C- and L/P-bands.

18 respectively (see Table 5.3). Both the sites consists of Sakhalin-spruce trees planted in 1998 (stand 14) and 1994 (stand 18), and the mean tree height of these two test sites are 0.9m and 2.5m respectively. Thus, at the time of Pi-SAR data acquisition in 2002, both the forests consisted of very young trees of low biomass and of some low vegetation. These young trees give rise to non-homogeneous radar backscatter and the SAR images of highly non-Gaussian textures. They are certainly not statistically homogeneous surface to yield SAR images of Gaussian speckle. This is the reason why the order parameter does not increase as the biomass decreases to very small values in Fig.5.17. Even if very low biomass area leads to high order parameter value, we can use RCS to check or estimate very low biomass cases.

For forests of small to moderate biomass shown in Fig.5.22 (b) and (c) respectively, trees are sparsely distributed and a high-resolution SAR can, to some extent, resolve tree structures. The radar backscatter in this case is due to the surface scattering, multiple reflection and volume scattering illustrated in Fig.5.21. Discrete strong backscatter results from multiple reflection, and volume scattering from the crown layer gives rise to the structure-dependent variation to the radar backscatter. Reflecting this backscatter of mixed contributions, the image amplitudes are not distributed statistically homogeneous, *i.e.*, the amplitude PDF has a non-Rayleigh distribution, and the K-distributions of small order parameters describe such highly fluctuating amplitudes.

For the forests of small biomass, the soil moisture and surface roughness are considered to take some impact on the order parameter. If the surface is smooth and soil moisture is high, the multiple scattering between the surface and small trees increases, while the surrounding speckle mean amplitude decreases.

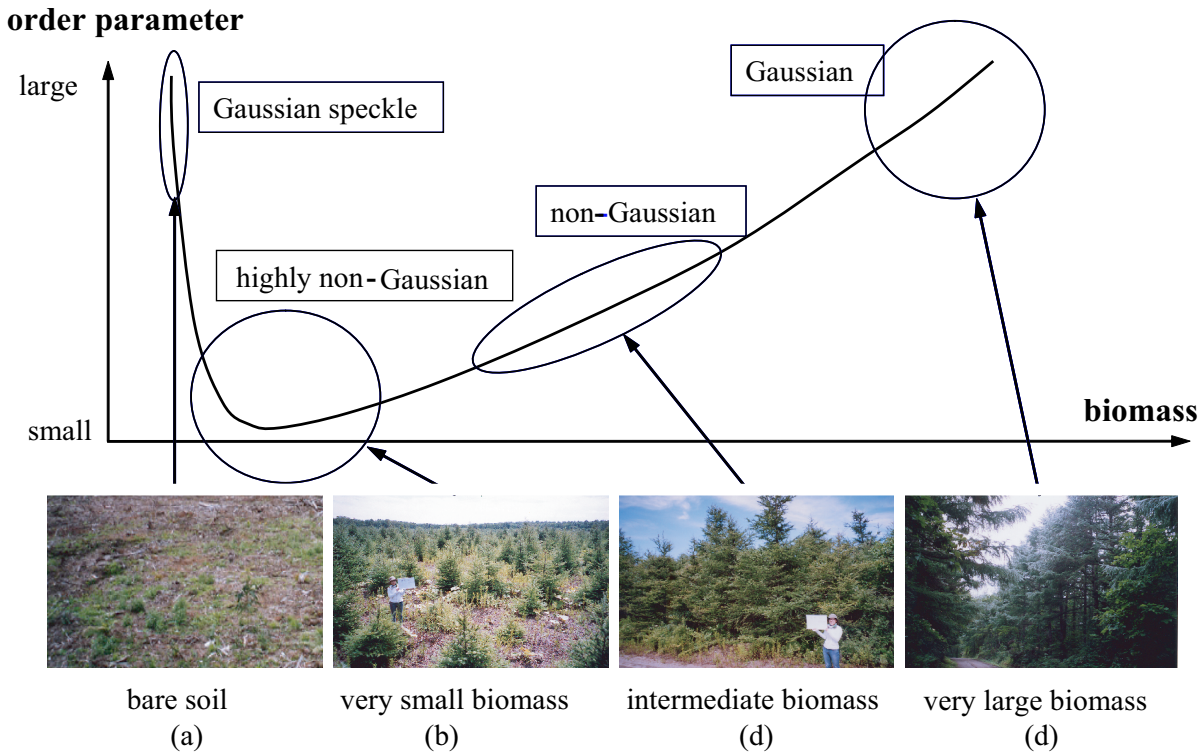

Figure 5.22: Interpretation of the regression curve between order parameter of K-distribution and different biomass, (a) zero biomass, that is, bare soil; (b) low biomass; (c) moderate biomass; (d) high biomass.

Then, the image amplitudes corresponding to the trees increase, leading to non-Rayleigh distribution with very large amplitude variance, and consequently the order parameter would become smaller. In the reversed manner, the order parameter is expected to increase with increasing surface roughness and/or decreasing soil moisture.

As the tree biomass increases and the forests become dense as shown in Fig.5.22 (d), the contributions from the discrete multiple scattering and surface scattering decrease, and the radar backscatter is dominated by the volume scattering from the crown layer. For example, the contributions of volume scattering in test 13 and test 14 are -4.0 dB and -10.2 dB, respectively. Accordingly, the SAR images tend to become Gaussian speckle and the order parameter increases. In the limit of very dense forests with very large biomass, the gaps among trees are filled with dense crown layer. The incident microwave can no longer penetrate to the forest interior and the dominant backscatter comes from the statistically homogeneous crown layer. The SAR images appear as a classical Gaussian speckle pattern, which can be described by the K-distribution of very large order parameter, *i.e.*, Rayleigh distribution. In practice, the K-distribution is nearly identical to the Rayleigh distribution for $\nu \sim 30$, and it becomes less sensitive to the order parameter of large values.

It is clear that the approach based on the non-Gaussian statistics requires high-resolution SAR images.

As the size of SAR resolution cell increases, it becomes difficult to resolve fine features of forests, and the amplitude statistics tend to become Gaussian. The order parameters and regression curves computed in Fig.5.17 is certainly dependent on the SAR resolution as well as the tree biomass, species, and also radar incidence angles. It can be conjectured that at small incidence angles deeper penetration of microwave into the forests yields strong contribution from the multiple reflection between ground and tree trunks and branches. With increasing incidence angles the contribution from the crown layer increases. The order parameter of the K-distribution can then be expected to be small at smaller incidence angles for the forests of same structures. In the present study, the difference in incidence angles for most test sites are not large (40°-44°), and the effect of incidence angle is considered to be small. The quantitative dependencies of the non-Gaussian statistics on SAR resolution and incidence angles are subjects of future investigation.

5.7 Accuracy of Regression Model

The accuracy of the regression curve of equation (5.8) to estimate needs to be investigated. For this purpose, comparison is made between the biomass estimated by the regression model and the ground-truth biomass collected in 2005 as listed in Table 5.4. Table 5.8 and Fig.5.23 are the results of the comparison. It can be seen that the total biomass of the field data is 1855.1 ton/ha, and that estimated from the SAR data is 1898.8 tons/ha. The SAR measurement overestimated by 43.7 tons/ha. The average measurement accuracy of individual plot is 85%. Further, it can also be seen that the differences of 4 test sites are over 20 tons/ha, and 3 of them are underestimated.

The possible sources of large differences between the model prediction and ground-truth data are (1) non-uniformity of forest stand, (2) undergrowth and (3) mixed species.

In (1), structural uniformity is tested by measuring at two plots in a same stand by two independent groups. The test is carried out in two stands. The biomass difference is found to be 5.4% and 7.7%. The statistically non-uniform tree structures may cause large fluctuations in the ground-truth data and model prediction. In (2), there exist substantial differences in undergrowth. We have not taken the effect of undergrowth into consideration. In (3), in some forest stands, there are mixed species of tall broadleaf trees among conifer. It can be seen from Table 5.8 that the estimation errors of 4 stands are over 20 tons/ha, and 3 of them are underestimated. It is probably because there are some very tall broadleaf trees in these stands. These tall broadleaf trees yield highly non-Gaussian texture in the radar images with smaller order parameters, and hence smaller biomass values than that measured on the ground.

Table 5.8: Comparision between the ground truth data and the biomass estimated by regression curve (uint: tons/ha). The numbers in the brackets are the percentage of difference.

site	Species	Field Data	Model Prediction	Difference
1	Japanese larch	50.8	68.6	17.8 (35.0)
2	Japanese larch	107.9	132.4	24.5 (22.7)
3	Sakhalin-spruce	85.6	61.8	-23.8 (27.8)
4	Japanese larch	111.8	102.1	-9.7 (8.7)
5	Sakhalin-spruce	71.9	71.5	-0.4 (0.6)
6	Todo-fir	43.8	55.3	11.5 (26.3)
7	Sakhalin-spruce	161.3	132.0	-29.3 (18.2)
8	Sakhalin-spruce	67.5	71.0	3.5 (5.2)
9	Todo-fir	71.6	80.6	9.0 (12.5)
10	Todo-fir	79.6	93.9	14.3 (18.0)
11	Sakhalin-spruce	126.7	124.5	-2.2 (1.7)
12	Sakhalin-spruce	97.5	110.5	13.0 (13.3)
13	Sakhalin-spruce	36.5	43.8	7.3 (20.0)
14	Sakhalin-spruce	79.3	94.6	15.3 (19.3)
15	Sakhalin-spruce	97.2	93.9	-3.3 (3.4)
16	Sakhalin-spruce	97.4	87.0	-10.4 (10.7)
17	conifer	52.4	67.9	15.5 (29.6)
18	Japanese larch	121.0	88.0	-33.0 (27.3)
19	Sakhalin-spruce	66.8	66.8	0.0 (0.0)
20	Yezo-spruce	0.1	0.0	-0.1 (100.0)
21	Sakhalin-spruce	56.9	67.4	10.5 (18.5)
22	Sakhalin-spruce	46.1	50.8	4.7 (10.2)
23	Sakhalin-spruce	125.3	134.3	9.0 (7.2)
total		1855.1	1898.8	43.7

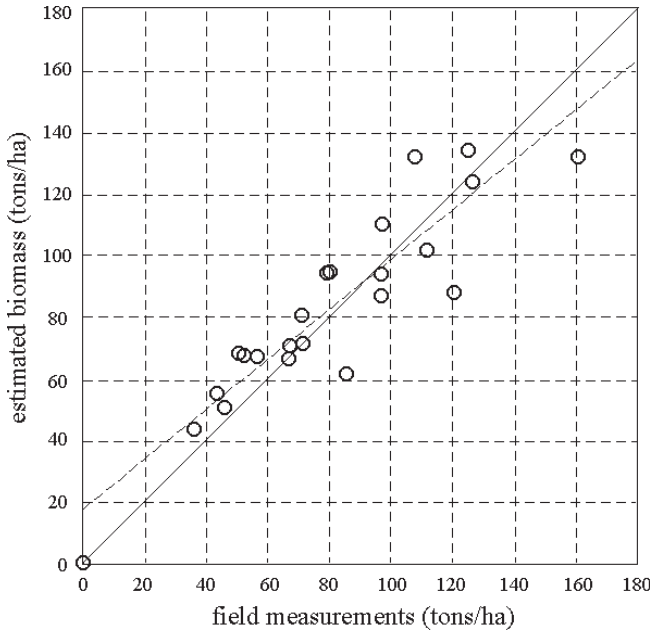

Figure 5.23: The scatter diagram between estimated biomass and ground truth data. The solid line is the ideal theoretical relation, and the broken line is the regression line from the actual data.

5.8 Biomass Classification

Having proven the accuracy of the regression curve given by equation (5.8), a new regression model can be developed by including the ground-truth data collected in 2005 as listed in Table 5.4. Fig.5.24 shows the scatter diagram containing all ground-truth data and the new regression curve. The correlation coefficient is 0.90, which is slightly higher than that in Fig.5.17. The regression curve is found to be

$$\nu = a_0 + a_1 B + a_2 B^2 + a_3 B^3 \tag{5.9}$$

where the coefficients, from a_0 to a_3, are 3.6889, 0.0028, 0.0027 and -1.1996$\times 10^{-5}$, respectively. ν is order parameter, and B denotes biomass.

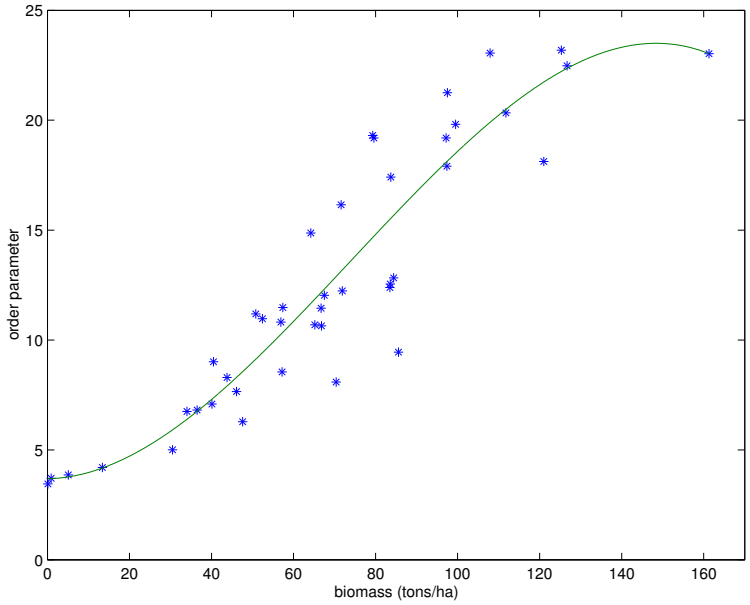

Figure 5.24: Order parameter of K-distribution as a function of forest biomass for the HV-polarization data. The correlation coefficient is 0.90. Third-order polynomial is used to fit the regression curve.

As mentioned before, Tomakomai forests are well-managed national forests with typical stand size 500m $\times$ 500m. The stands around the test sites were selected from the Pi-SAR HV-polarization data and their order parameters of K-distribution were estimated. The corresponding biomass can then be estimated by this regression curve.

Fig.5.25 is the map of tree biomass around the Tomakomai test sites. The tree biomass of each site is computed from the regression curve derived from the order parameter of the K-distribution in the cross-polarisation data in Fig.5.24, *i.e.*, equation (5.9). Though we could not compare the estimated biomass with ground-truth data in the whole area, Fig.5.25 is a good example, highlighting the utilization of the order

parameter of the K-distribution for tree biomass estimation.

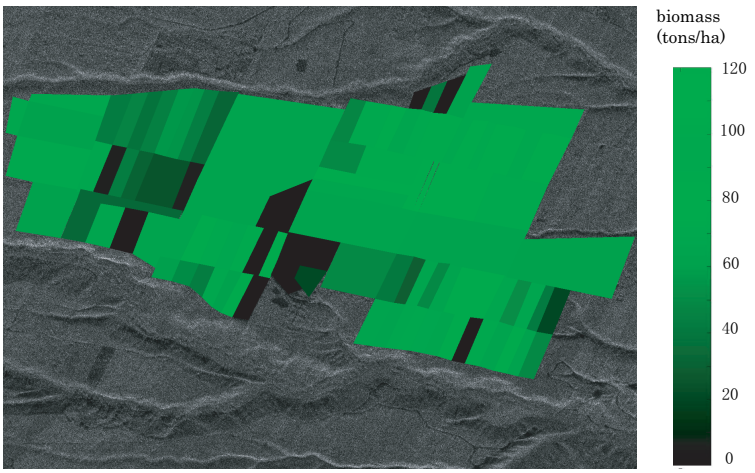

Figure 5.25: Map of tree biomass around the Tomakomai test sites based on the regression curve of the order parameter of the K-distribution derived from the cross-polarisation data shown in Fig.5.24.

5.9 Summary and Future Work

In this chapter, the non-Gaussian statistics described in previous chapters are applied to extracting forest information from the high-resolution polarimetric Pi-SAR data over the Tomakomai forests in Hokkaido, Japan. The forests of interest are conifers of four main species, including Japanese larch, Todo-fir, Yezo-spruce and Sakhalin-spruce. Japanese larch is deciduous, and this is the reason why the decomposition result of X-band data shows that volume scattering is the main scattering mechanism in November as can be seen from Fig.4.12 in Chapter 4.

Ground-truth data collection was made in 2002, 2003 and 2005. There are 19 test sites were measured in 2002 and 2003, and 23 test sites in 2005. At each 20×20 m^2 plot, average tree height, age, basal area, DBH and biomass are measured. The biomass calculation formulae for Hokkaido forests are used to calculate the biomass.

The relations between RCS of X- and L-bands data and forest parameters are investigated for all the polarizations, and the results show that at X-band, the RCS is largest for VV-polarization followed by HH- and HV-polarizations; while at L-band it is largest for HH-polarization followed by VV- and HV-polarizations. Both X- and L-bands RCS increase as the forest parameters increase and saturate at some levels. However, X-band RCS data are not well correlated with forest parameters, and the RCS saturation levels are difficult to define. The L-band RCS saturation levels are found approximately to the biomass of 40 tons/ha, the tree age of 30 years, the basal area of 30 m^2/ha, and the tree height of 8 m.

To search new parameters that relate to the forest biomass and other parameters beyond the RCS saturation limits, the non-Gaussian texture analysis is considered. Since L-band data contain more information than X-band, only L-band data are used for statistical analysis. The best fitted model, K-distribution, is found by using the AIC among the Rayleigh, log-normal, Weibull and K-distributions. The order parameter of K-distribution is then plotted as a function of forest parameters including biomass, tree age, basal area and tree height. The results show that biomass has the highest correlation with the order parameter in the cross-polarization data, and the regression curve is derived by using the third-order polynomial fitting. This regression model is used to estimate the forest biomass and the estimated results are compared with the ground truth data collected in 2005. The comparison shows that the estimation accuracy is 85%. Possible reasons which may cause large uncertainty are considered, including the non-uniformity of forest structure, undergrowth, and mixed species. Finally the regression model is updated by including all the ground truth data, and using this new regression model, a map of biomass is produced for the forests around the study area.

For the future work, the following subjects are considered.

- Effects of incidence angles and resolution on the image amplitude distribution.
- Scattering mechanisms that gives rise to the non-Gaussian distribution.
- Usage of high-resolution optical (IKONOS,QuickBird) images.
- Applications to change detection in forests.
- Applications using the ALOS-PALSAR data.

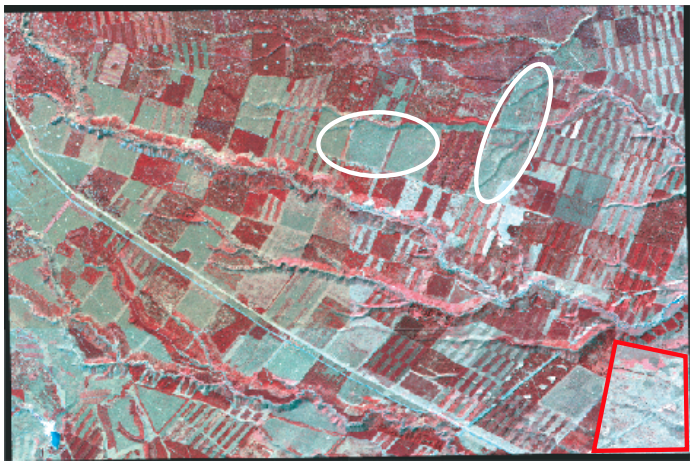

Figure 5.26: False colour composite optical image by QuickBird over Tomakomai forests acquired on 6th, Apr., 2002.

Fig.5.26 shows the QuickBird false colour image, and the tree species in the stands with the color marked by the two white ellipses is Japanese larch, while the tree species in the area marked by the red quadrangle is deciduous broadleaf. Moreover, the Japanese larch can also be identified by the X-band decomposition result shown in Fig.4.12. It is am interesting future study to investigate whether these two approaches can be merged to increase classification accuracy of tree species.

In September 2004, a typhoon caused considerable damage to the Tomakomai forests. An example is shown in Fig.5.27. Some of fallen trees were cleared, and the areas were almost plain as in Fig.5.28. It appeared that the difference in RCS between the forests before and after the typhoon damage is order of 1-2 dB in the Pi-SAR data. Polarimetric analysis may be a useful technique to detect such changes since there is a certain difference in the forest structure.

Figure 5.27: Fallen trees caused by typhoon.

Figure 5.28: The fallen trees caused by typhoon were cleared.

Chapter 6

Applications to Oceanography

6.1 Introduction

This chapter presents the theoretical development and experimental results on the interlook correlation of Gaussian speckle in sub-images of dynamic ocean surfaces produced by multilook processing. The technique of multilook processing is used for speckle noise reduction and equalization of two-dimensional resolution scale in SAR imagery. It is based on incoherent addition of uncorrelated multilook intensity images produced with non-overlapping sub-apertures (an equivalent result, for stationary surfaces, can be obtained by averaging neighboring pixels in the full single-look intensity images), and a substantial number of publications concerning this issue are available (*e.g.* [3], [14]-[16]). However, it is surprising to find that very little, is reported in open literature on the interlook cross-correlation property between speckle patterns produced by using partially overlapped sub-apertures. An exception is the theoretical study of Ouchi and Burge [61] who describe the cross-correlation function (CCF) for Gaussian amplitude sub-aperture weightings. Their results also show that the CCF is independent of a scene coherence time of randomly fluctuating sea surfaces, provided that the backscattered field is modeled as a Gaussian white noise. However, to date no experimental data have been provided to support the theory. However, In the previous study [75] of ship detection by the cross-correlation technique, it is experimentally shown that the interlook cross-correlation function of speckle intensity in the RADARSAT-1 images of sea surface produced by partially overlapped sub-apertures appears to be independent of the scene coherence time.

Fig.6.1 illustrates partially overlapped sub-image processing. Return signal from randomly moving sea surface is subject to fade, i.e., the signal fluctuates with time, and the scene coherence time is around 0.01-0.2 s. These coherence times are shorter than SAR integration times. It may then be possible, by using partially overlapped sub-apertures, to extract extra look sub-images whose speckle patterns are uncorrelated.

Thus, the purpose of this study is to report the theoretical study on the cross-correlation function of intensity speckle patterns in terms of the center time difference of partially overlapped sub-apertures, and the experimental results using real SAR data for comparison with the theory. In the first part of the

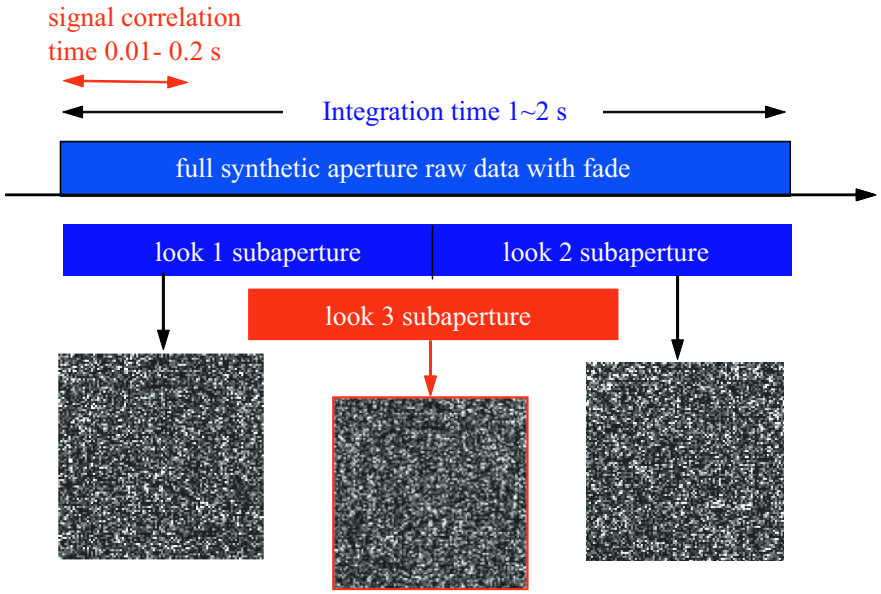

Figure 6.1: Illustration of multilook processing with partially overlapped sub-images over sea surface.

chapter, a general integral expression for the intensity CCF of speckle patterns produced through partially overlapped sub-apertures at arbitrary center times is derived and discussed. An assumption is made that the backscattered spatial field is modeled as being statistically "white", so that the resultant speckle patterns between sub-images produced by non-overlapping sub-apertures are spatially uncorrelated. Further, the theory takes account of the random temporal fluctuation of the return signal from the sea surface. The result shows that the interlook speckle CCF is proportional to the modulus square of the autocorrelation function of the sub-aperture amplitude weighting function, where the time lag variable is the center time difference. It is also shown that the interlook speckle CCF is independent of the temporal fade process of the backscattered field. For simplicity, the theoretical treatment is given only in the azimuth direction since the multilook processing is applied to the azimuth component. An analytic expression of the interlook CCF is then derived from the integral equation for a rectangular amplitude weighting of sub-apertures. Finally, this theoretical CCF is compared with those computed from the JERS-1 L-band SAR and RADARSAT-1 C-band SAR images over the coastal waters of Japan [76].

6.2 Basic Theory of Cross-Correlation Function

6.2.1 Siegert Relation

When a statistically homogeneous random rough surface is imaged by a SAR, a Gaussian speckle pattern, inherent to coherent systems, is formed. As described in the previous chapters, the term "Gaussian" stems

from the fact that the real and imaginary parts of the complex amplitude of the speckle field obey a Gaussian PDF, provided that more than about 4 to 8 independent scatterers exist within a resolution cell to satisfy the central limit theorem [6], [62]. It is well known that the amplitude and intensity fluctuations of such speckle patterns are described by the Rayleigh and negative exponential PDFs respectively [3], [14], [16]. It is also well known that the intensity CCF of Gaussian speckle patterns in the sub-images can be described the Siegert coherence function [89]

$$\langle I(X;\tau_n)\, I(X;\tau_{n'})\rangle = \langle I\rangle^2 + |\langle A(X;\tau_n)A^*(X;\tau_{n'})\rangle|^2 \tag{6.1}$$

where the angular brackets indicate taking an ensemble average (expectation value), $I(X;\tau_n)$ is the intensity at an image position X produced by the sub-aperture of center time τ_n, A is the image complex amplitude, and the asterisk $*$ means taking complex conjugate. The relation of equation (6.1) is valid if the random fluctuation in the image is a wide-sense stationary Gaussian process with $\langle I(X;\tau_n)\rangle = \langle I(X;,\tau_{n'})\rangle$. Equation (6.1) shows that the intensity CCF is proportional to the modulus square of the autocorrelation function of speckle amplitude. The deduction of one-dimensional Siegert relation is shown in Appendix A.

6.2.2 Image Complex Amplitude of Arbitrary Center Time

In order to evaluate equation (6.1), the expression for the image complex amplitude $A(X;\tau_n)$ needs to be derived by taking into account the random temporal fluctuation of the scattering surface. It is important, therefore, to start the analysis from the SAR image formation with an arbitrary azimuth center time as follows.

A SAR antenna transmits a series of pulses and receives return signals as it propagates in the azimuth direction. A signal received at an azimuth time t from a point scatterer at an azimuth surface position x is given by

$$s_s(x,t) = a_s(x)a_t(t|x)\exp\left(-i2kr(x,t)\right) \tag{6.2}$$

where $k = 2\pi/\lambda$ is the wavenumber, λ is the wavelength, and $r(x,t)$ is the distance between the radar and the scatterer. The scattering amplitude is factorized to the spatial field $a_s(x)$ and its temporal change $a_t(t|x)$, where the temporal change is conditional upon the scatterer being observed at x, and it is a function of the azimuth time t only [63]. Examples corresponding to this type of scattering objects include the sea surface that is the subject of the present study, and forests on land under strong wind conditions.

It should be noted that, in practice, the amplitude of the return signal of equation (6.2) is weighted by the illuminating azimuth beam pattern. This weighting is removed in equation (6.2), because in the

SAR processor used for the study [90] the beam pattern is corrected during the image forming process. In brief, the azimuth power spectrum is estimated first, and the amplitude of the image complex spectrum is smoothed before taking inverse FFT to produce each look image. The Doppler offset varies with range, so that the smoothing is required for each azimuth line at different range positions.

Similar as equation (3.25), the slant-range distance r can be approximated as follows.

$$\begin{aligned} r(x,t) &= \sqrt{R_0^2+(v_a t-x)^2} \\ &\simeq R_0+\frac{(v_a t-x)^2}{2R_0} \end{aligned} \tag{6.3}$$

In the expression, R_0 is the slant-range distance when the radar is directly above (abeam of) the scatterer, and v_a is the platform velocity. The return signal from an extended surface can then be given by substituting equation (6.3) into equation (6.2), and integrating the return signal of equation (6.2) over the surface with respect to the azimuth spatial variable x as

$$s(t)=E_0\int_{-\infty}^{\infty} a_s(x)a_t(t|x)\,\exp\left(-i\frac{kv_a^2}{R_0}(t-\frac{x}{v_a})^2\right)dx \tag{6.4}$$

where the term $\exp(-i2kR_0)$ has been absorbed in the constant E_0. The complex amplitude of a look n image can be produced by correlating the return signal of equation (6.4) with a sub-reference signal s_r as

$$A(X;\tau_n)=\int_{-\infty}^{\infty} s\left(\frac{X}{v_a}+t\right)s_r(t)\,dt \tag{6.5}$$

where the look n sub-reference signal is given by

$$s_r(t;\tau_n)=W\left(\frac{t-\tau_n}{\tau_A}\right)\,\exp\left(i\frac{kv_a^2}{R_0}t^2\right)dt \tag{6.6}$$

In this expression, W is the amplitude weighting function centered at the azimuth time τ_n, and τ_A is the integration time to synthesize the sub-aperture. Substituting equation (6.4) and equation (6.6) into equation (6.5) yields the complex amplitude of the look n image

$$\begin{aligned} A(X;\tau_n)=A_0\int_{-\infty}^{\infty}dx\int_{-\infty}^{\infty}dt\,W\left(\frac{t-\tau_n}{\tau_A}\right)a_s(x)a_t\left(\frac{X}{v_a}+t\,\middle|\,x\right) \\ \cdot\exp\left(-i\frac{k}{R_0}(X-x)^2\right)\exp\left(-i\frac{2kv_a}{R_0}(X-x)t\right) \end{aligned} \tag{6.7}$$

where A_0 is a normalizing constant.

6.2.3 General Integral Expression for CCF of Speckle Intensity

From equation (6.7), the amplitude CCF between the look n and look n' images can be expressed as

$$\begin{aligned}\langle A(X;\tau_n)A^*(X;\tau_{n'})\rangle = |A_0|^2 \iint_{-\infty}^{\infty} dx_1 dx_2 \iint_{-\infty}^{\infty} dt_1 dt_2 W\left(\frac{t_1-\tau_n}{\tau_A}\right) W^*\left(\frac{t_2-\tau_{n'}}{\tau_A}\right) \\ \cdot\langle a_s(x_1)a_s^*(x_2)\rangle \left\langle a_t\left(\frac{X}{v_a}+t_1|x_1\right) a_t^*\left(\frac{X}{v_a}-t_2|x_2\right)\right\rangle \\ \cdot\exp\left(-i\frac{k}{R_0}\left((X-x_1)^2-(X-x_2)^2\right)\right) \\ \cdot\exp\left(-i\frac{2kv_a}{R_0}\left((X-x_1)t_1-(X-x_2)t_2\right)\right) \end{aligned} \tag{6.8}$$

In order to simplify the four-fold integral of equation (6.8), the backscattered field is modeled as being statistically white. This assumption of a white noise approximation implies that the phases are random and distributed uniformly over $[0, 2\pi)$, and that they are uncorrelated to each other and to the amplitudes [3]. The autocorrelation function of the backscattered spatial field can then be approximated by the following ensemble average.

$$\langle a_s(x_1)a_s^*(x_2)\rangle = \langle\sigma\rangle\,\delta(x_1-x_2) \tag{6.9}$$

where $\langle\sigma\rangle$ is the radar cross section, and δ is the Dirac delta function. The temporal correlation function can be defined as [63]

$$\langle a_t(t_1|x_1)a_t^*(t_2|x_2)\rangle = \gamma(t_1-t_2)|_{x_1=x_2} \tag{6.10}$$

which is a function of time difference between t_1 and t_2 only at a same surface position $x_1 = x_2$. In equation (6.9) and equation (6.10), the spatial and temporal fluctuations a_s and a_t are wide-sense stationary stochastic processes. Substituting equation (6.9) and equation (6.10) into equation (6.8), and integrating with respect to x_1, equation (6.8) can be simplified to

$$\begin{aligned}\langle A(X;\tau_n)A^*(X;\tau_{n'})\rangle = |A_0|^2\langle\sigma\rangle \int_{-\infty}^{\infty} dx \iint_{-\infty}^{\infty} dt_1 dt_2 W\left(\frac{t_1-\tau_n}{\tau_A}\right) W^*\left(\frac{t_2-\tau_{n'}}{\tau_A}\right) \\ \cdot\gamma(t_1-t_2)\exp\left(-i\frac{2kv_a}{R_0}(X-x)(t_1-t_2)\right)\end{aligned} \tag{6.11}$$

where $x = x_2$. The spatial extent of the statistically homogeneous surface is assumed to be large, then the integration of equation (6.11) with respect to x can be approximated as

$$\int_{-\infty}^{\infty}\exp\left(i\frac{2kv_a}{R_0}(t_1-t_2)x\right)dx \simeq c_0\,\delta(t_1-t_2) \tag{6.12}$$

where c_0 is a constant with an appropriate dimension. Then, integrating equation (6.11) with respect to t_1 and putting $t=t_2$, equation (6.11) reduces to the following simple integral.

$$\langle A(X;\tau_n)A^*(X;\tau_{n'})\rangle = |A_0|^2 \int_{-\infty}^{\infty} W\left(\frac{t-\tau_n}{\tau_A}\right) W^*\left(\frac{t-\tau_{n'}}{\tau_A}\right) dt \tag{6.13}$$

where all constants have been absorbed in $|A_0|^2$.

The result of equation (6.13) states that the interlook CCF of speckle complex amplitudes in the sub-images centered at azimuth center times τ_n and $\tau_{n'}$ is given by the autocorrelation function of the amplitude weighting function of sub-reference signals. The CCF of the intensity speckle patterns given by equation (6.1) is therefore proportional to the modulus square of equation (6.13). It is important to emphasize that the interlook cross-correlation property is dependent only on the sub-aperture weighting function, and it is independent of the temporal correlation function of equation (6.10), provided that the backscattered spatial field is a statistically white random process.

6.2.4 Interlook CCF for Rectangular Weighting Function

For a rectangular weighting function

$$\begin{aligned} W\left(\frac{t-\tau_n}{\tau_A}\right) = \text{rect}\left(\frac{t-\tau_n}{\tau_A}\right) = 1 \quad &: \quad -\frac{\tau}{2} \le t-\tau_n \le \frac{\tau}{2} \\ 0 \quad &: \quad \text{otherwise} \end{aligned} \tag{6.14}$$

the normalized intensity CCF is readily given by

$$\begin{aligned} C(\Delta\tau) &\equiv \frac{\langle I(X;\tau_1)I(X;\tau_2)\rangle}{\langle I\rangle^2} - 1 \\ &= \left(1-\frac{\Delta\tau}{\tau_A}\right)^2 \end{aligned} \tag{6.15}$$

where $\Delta\tau = |\tau_1 - \tau_2| \le \tau$ is the center time difference between the look 1 and look 2 sub-apertures. The two speckle patterns in the sub-images are identical when $\Delta\tau = 0$, and they are, of course, perfectly correlated. As $\Delta\tau$ increases, the overlapping area of sub-apertures decreases and the speckle patterns start to decorrelate. They decorrelate completely when the center time difference equals ($\Delta\tau = \tau$) or $\Delta\tau$ is greater than the integration time, since there is no overlapping area between two sub-apertures. When these uncorrelated speckle patterns are added on an intensity basis, the speckle fluctuation reduces by the factor of $1/\sqrt{N}$ where N is the number of uncorrelated speckle patterns. This is the basis of speckle reduction by multilook

processing.

In spaceborne SARs such as ENVISAT, RADARSAT-1 and JERS-1 SAR, the integration times of a full single look are approximately 0.5-2.0 s, so that the integration times of N-look sub-images are in the range between $0.5/N$ and $2.0/N$ s, while the coherence (decorrelation) time of sea surfaces is in the order of 0.05–0.1 s for L-band, and 0.05 s or less for C-band [64]-[70]. It has been suggested that if the interlook speckle patterns were to decorrelate according to the sea surface coherence time (which is much shorter than the integration time of a sub-aperture), sub-images with uncorrelated speckle patterns could be produced through partially overlapped sub-apertures. Hence, an extra look sub-image could be extracted from the raw data of full synthetic aperture length. For example, instead of two sub-apertures three partially overlapped sub-apertures of the same bandwidth could be used to produce three sub-images with uncorrelated speckle patterns [71]. However, this cannot be done for the case of Gaussian speckle, since, from the result of equation (6.13) and equation (6.15), the CCF of intensity speckle patterns is independent of the scene coherence time.

The situation is different for scatterers that give rise to non-Gaussian intensity fluctuations [16], [61], [72], [73]. It can easily be conjectured that the image of an isolated deterministic scattering object such as a corner reflector or transponder must have high degrees of interlook correlation even if the center time difference becomes very large. If the received signal from such a scatterer (elementary scattering object) has temporal fluctuations within the integration time (for example, by randomly varying the return signal from a transponder), the interlook correlation time would be shorter than the integration time. If, therefore, the backscattered field is statistically "non-white" consisting of a few such randomly fluctuating scatterers, then the fluctuations in image intensity obey non-Gaussian statistics, and the interlook CCF becomes dependent on the scene coherence time. Analysis of such situation is given in the previous theoretical study [75], but it is not the purpose of this thesis to examine the non-Gaussian speckle. Thus, we restrict the present discussion to the case of Gaussian speckle fluctuations, where the CCF is a function only of the sub-aperture weighting function and the interlook time difference, provided that the backscattered field is statistically white.

6.3 Experimental Results and Discussion

6.3.1 JERS-1 SAR Data

The JERS-1 SAR [77] was in operation from 1992 to 1998 at L-band (wavelength 0.235 m; frequency 1.275 GHz) in HH-polarization with nominal resolution of 6 m (full single-look) in azimuth and 18 m in ground-range directions. It was designed for the global land observation, having the nominal off-nadir angle of 35° to reduce the foreshortening and layover effects, and hence it was considered as being not well suited for

oceanic applications. However, under favorable conditions, the JERS-1 SAR data can be used to extract oceanic information [74].

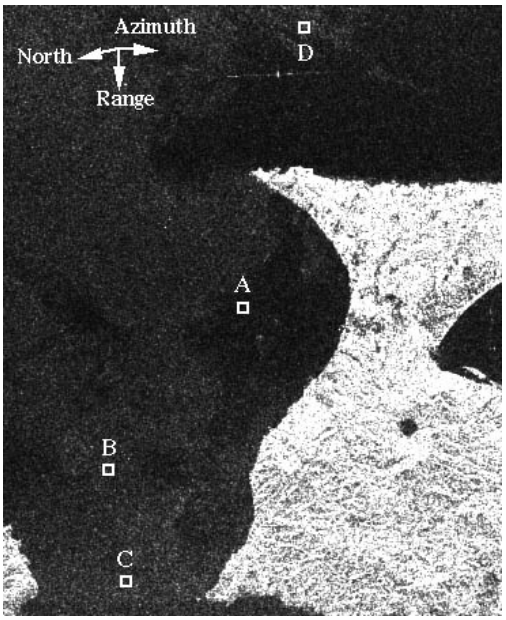

Figure 6.2: JERS-1 SAR intensity image of the Tsugaru Strait between the mainland Honshu and Hokkaido, Japan. The size is approximately 68 km and 55 km in azimuth and range respectively. The white boxed areas marked "A", "B", "C" and "D" of size 100×100 pixels are used for the analysis.

Fig.6.2 shows the JERS-1 SAR intensity image of the Tsugaru Strait located between Hokkaido and mainland (Honshu) Japan, and the image center is approximately at 41° 30' N and 141° 17' E, with data acquisition time of 01:23 GMT on the 26th of June 1997. The ocean currents are strong in the strait flowing from west to east (from "C" to "B" in Fig.6.2). According to the Japan Oceanographic Data Center, the maximum current velocity at the area "C" in June is 4.6 knots (2.4 m/s) with mean velocity of 1.1 knots (0.57 m/s). The database of the Japan Weather Association (JWA) show that at the time approximately an hour and half prior to the data acquisition (00:01 GMT), the wind speed was 4.0 m/s from west at the position marked "C" in Fig.6.2, and the ocean waves of mean wavelength 0.35 m, propagating toward south-west with the period 3.7 s. The image size is approximately 68 km and 55 km in azimuth and range directions respectively. In the image, no clear wave patterns are observed, and the image modulations over the strait appear to be associated with wind and currents. The white boxed areas labeled as "A", "B", "C" and "D" of each size 100×100 pixels are used to test the theory described in Section II. In order to compute the interlook cross-correlation function, the total of 9 images of the same area are processed. The bandwidth of the sub-reference signal is 400 Hz, and the Doppler center frequency is changed from -200 Hz to 200 Hz

with interval of 50 Hz. The relation between the Doppler frequency f_D and azimuth time t is given by

$$t = \frac{\lambda R}{2v_a^2} f_D \tag{6.16}$$

For this particular data set, the relative platform velocity is 7.3 km/s and slant-range distance is 697 km with the incidence angle of 39° at the center of the image of Fig.6.2. Then, the azimuth integration time of each sub-reference signal becomes 0.62 s and the interlook center time difference is 0.077 s. Both the azimuth and range resolution cells of the sub-images are 18 m.

6.3.2 RADARSAT-1 SAR Data

The RADARSAT-1 SAR is currently in operation at the radar wavelength of 5.6 cm (5.3 GHz at C-band HH-polarization) since its launch in 1995 [78]. Among several beam modes, the Standard Beam 1 is used in this thesis, with its nominal incidence angle of 24°, and the nominal azimuth (4-look) and range resolutions of 28m and 25 m respectively.

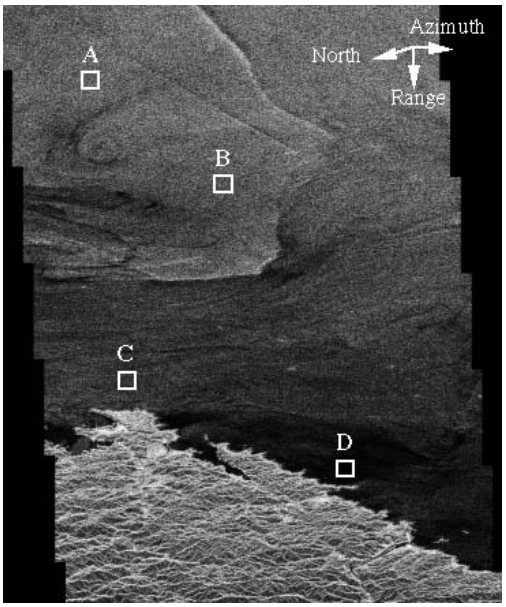

Figure 6.3: RADARSAT single-look intensity image of the Kumano Sea, Japan. The size is 24 km and 60 km in azimuth and range respectively. The white boxed areas marked "A", "B", "C" and "D" of size 100×100 pixels are used for the analysis.

Fig.6.3 shows the RADARSAT-1 intensity image over the coast of the Yoshino-Kumano National Park and the Kumano Sea (image center: 33° 34' N, 136° 00') acquired at 21:05 GMT on the 28th of October 1998. The size is approximately 24 km in azimuth and 60 km in range, and the white boxed areas marked as "A", "B", "C" and "D" of each size 100×100 pixels are used for analysis.

The meteorological data from the Japan Weather Association at the time three hours prior to the RADARSAT pass show the wind speed of 3 m/s from the northwest and significant waveheight of 0.9 m with period of 8 s, propagating from the southeast. A close inspection of the full scene shows the presence of ocean waves in the deep sea in the south-east away from the center of Fig.6.3, but no clear wave images are seen in the coastal sea shown in Fig.6.3, except some wind and frontal features and several ships with their wake lines. The mean intensity is largest in "A" indicating the presence of some wind, and it is smallest in "D" which is a wind-sheltered area.

In the present analysis, 11 sets of images are processed from the raw data using the sub-reference signal having the bandwidth of 500 Hz and the center frequencies ranging from -250 Hz to 250 Hz with the center frequency interval of 50 Hz. For the present data set, the slant-range distance is 983.5 km with the incidence angle of 27° at the center of the image of Fig.6.3, and the relative platform velocity is 7.0 km/s. From these parameters, the integration time of each look and interlook time difference are calculated as 0.28 s and 0.028 s respectively, and the azimuth and range resolution cells are 14 m and 25 m respectively.

6.3.3 Statistical Analysis of JERS-1 SAR Data

Before taking cross-correlation, the PDF of each area is estimated to ensure that the amplitude and intensity fluctuations constitute a Gaussian speckle pattern. Fig.6.4 is the amplitude and intensity PDFs of the areas "A" , "B" , "C" , and "D" in Fig.6.2, where the measured PDFs represented by the step line is in good agreement with the Rayleigh and negative exponential distributions of the smooth curves.

The data points in Fig.6.5 are the CCF values of intensity speckle patterns as a function of center time difference between two sub-apertures. It can be seen that the measured CCFs in the areas "A", "B" and "C" are in excellent agreement with the theoretical result of equation (6.15) indicated by the solid line, but the measured CCF in the area "D" is slightly larger than the theoretical curve. Close inspection shows that this is because there are some spatially correlated features in the image. The speckle image of the area "D" is well behaved in terms of the single-point statistics since the amplitude PDF follows the Rayleigh distribution as in Fig.6.4. However, the look 1 and 9 images of the area "D" shown respectively in the left and center images of the bottom row of Fig.6.6 are not statistically homogeneous and the spatial features seem to retain some correlation between look 1 and 9. The right image of each row shows the coherence image, *i.e.*, a map of correlation values, estimated by using 10 × 10 moving windows. The images are thresholded such that the bright pixels correspond to the degree of coherence larger than 0.35. A certain number of pixels with high degrees of coherence explain the discrepancy of the area "D" in Fig.6.5. Note that large-scale correlated features visible in the left and center images in the bottom row of Fig.6.6 are not captured in the coherence

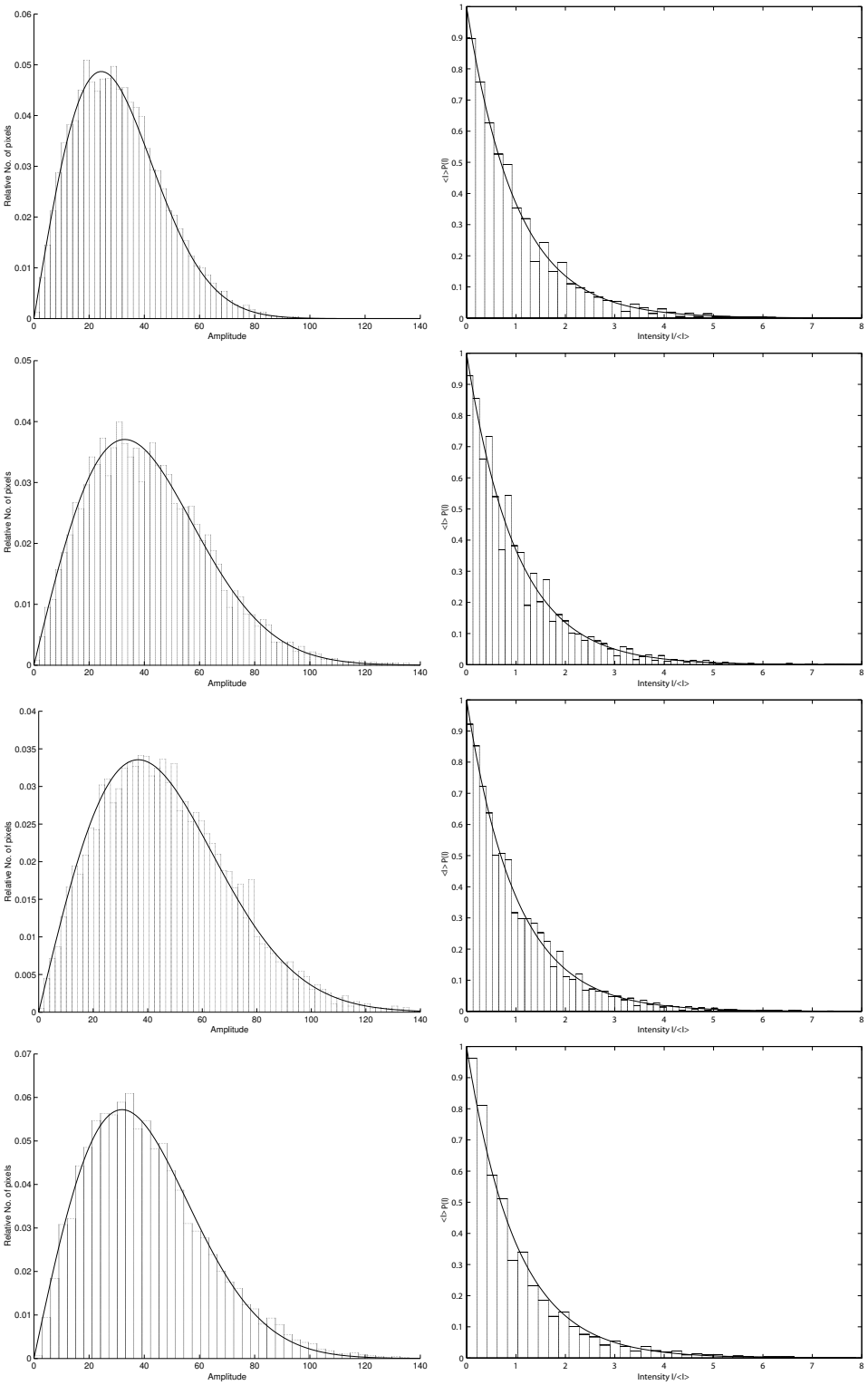

Figure 6.4: The PDFs of speckle amplitude (left) and intensity (right) corresponding to the area "A", "B", "C", and "D" (from top to bottom) in the JERS-1 SAR image shown in Fig.6.2. In the left graphs, the vertical axis is the relative number of pixels and the horizontal axis is the amplitude in digital number. In the right graphs, the vertical and horizontal axes the normalized PDF and intensity by the mean intensity, respectively. The measured amplitude and intensity PDFs represented by the step lines closely follow respectively the Rayleigh and negative exponential distributions of the smooth curves.

image, because of the small size of the moving windows.

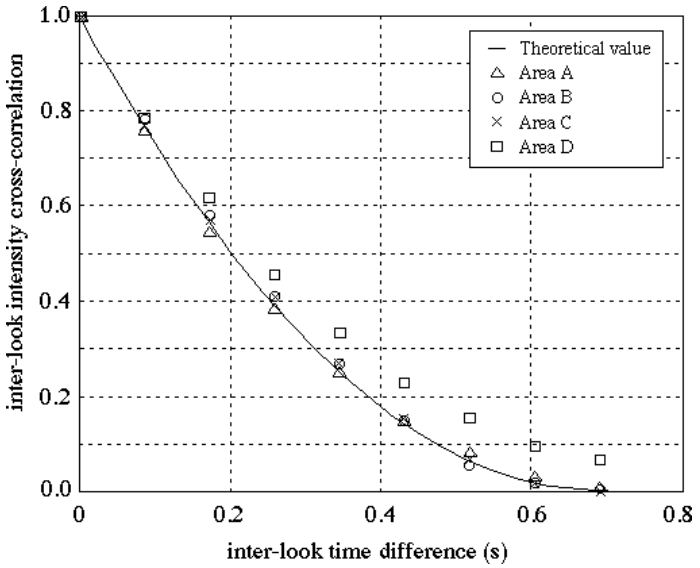

Figure 6.5: The interlook cross-correlation function of the area "A", "B", "C" and "D" in the JERS-1 SAR image shown in Fig.6.2 as a function of the center time difference. The solid line is the theoretical curve based on equation (6.15).

The look 1 and 9 images of the area "A", "B", "C", and "D" shown in the lower row of Fig.6.6 appear to be statistically uniform with little correlation between looks. The coherence images on the right also indicate that there are very small number of pixels with the degrees of coherence above 0.35. Thus, the correlated spatial features are the main reason why the degree of interlook cross-correlation in the area "D" is higher than the theoretical result of equation (6.15).

The look 1 to look 9 sub-images of the test areas in Fig.6.2 are shown in Fig.D1- Fig.D4 in the Appendix D. In close inspection, it can be seen that the look 1 and look2 images are very similar, *i.e.*, they are correlated, and that the images tend to become different with increasing look difference. Similar features can no longer be found between the look 1 and 9 images.

There are no simultaneous sea truth data on the scene coherence time, but in general the coherence time is approximately 0.1 s or less as mentioned in the above section. Therefore, if the scene coherence time were to enter the interlook cross-correlation function, then the interlook speckle patterns should have decorrelated at time lags of similar order, and the measured CCF in Fig.6.5 should have had shorter correlation times than the theoretical solid curve. The result shown in Fig.6.5 is an evidence that this is not the case, and the interlook CCF of speckle patterns is independent of the random temporal fluctuation of the backscattered field as predicted by equation (6.13) and equation (6.15), provided that the backscattered field is modeled as a statistically white random process.

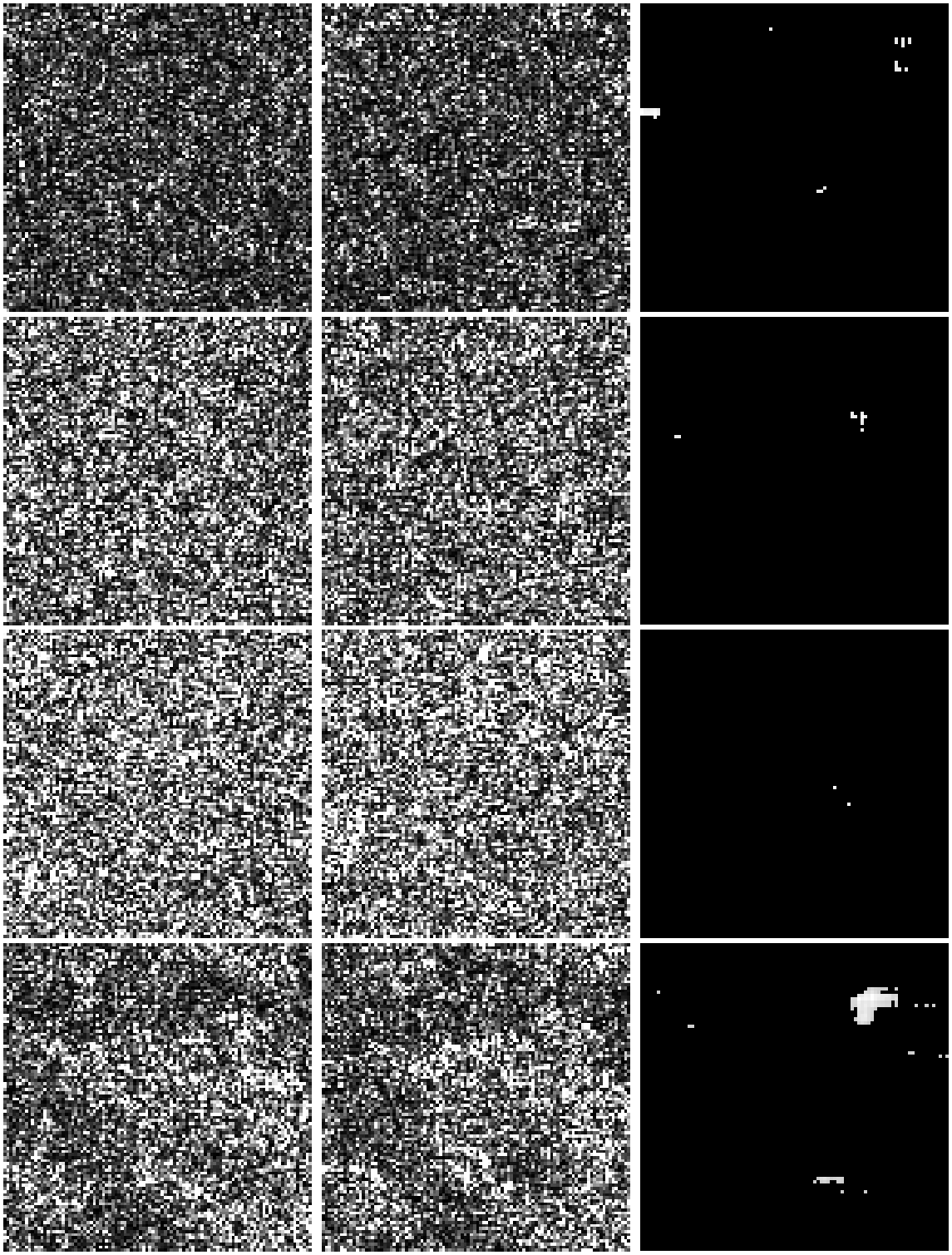

Figure 6.6: The left and center images from top to bottom are respectively the look 1 and 9 images of the area "A", "B", "C", and "D" in Fig.6.2. The right images are the corresponding coherence images produced by cross-correlating the look 1 and 9 images with moving windows of size 10 $\times$ 10 pixels, and thresholding by the correlation value of 0.35.

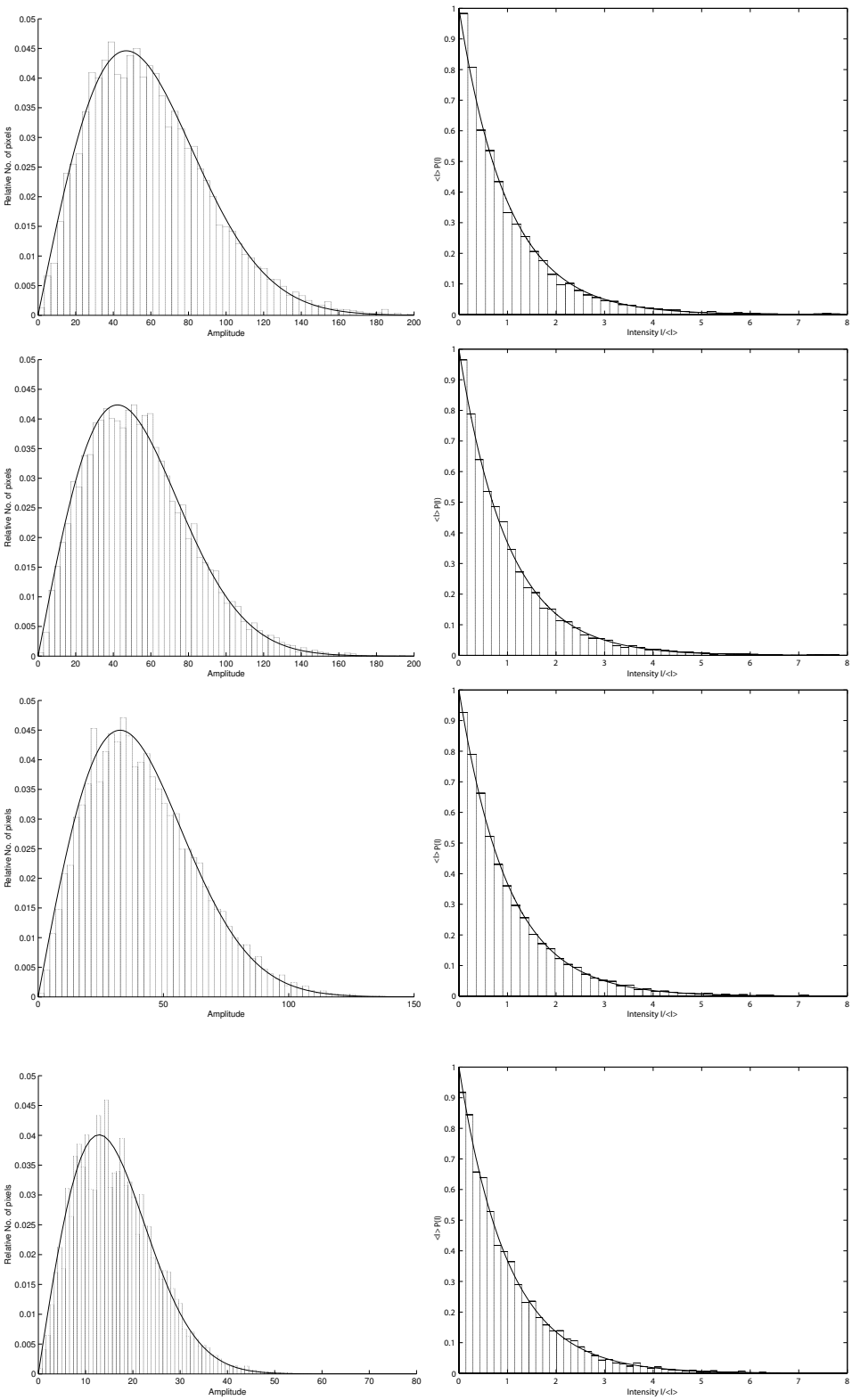

Figure 6.7: The PDFs of speckle amplitude (left) and intensity (right) corresponding to the area "A", "B", "C", and "D" (from top to bottom) in the RADARSAT-1 SAR image shown in Fig.6.3. The other parameters are the same as Fig.6.4.

6.3.4 Statistical Analysis of RADARSAT-1 Data

Fig.6.7 is the amplitude and intensity PDFs of the area "A", "B", "C", and "D" in the RADARSAT-1 image shown in Fig.6.3. Again, good agreements can be seen respectively between the measured PDFs and Rayleigh and negative exponential distributions.

Fig.6.8 is the interlook cross-correlation function of the RADARSAT-1 test images as a function of center time difference. The measured CCF values tend to over-estimate the theoretical curve mainly because of spatially correlated features (although the features are not as clear as those in Fig.6.6). This spatial correlation can be seen in Fig.6.9, where the left and center images are the look 1 and 11 images of the areas "A", "B", "C", and "D" (from top to bottom) in Fig.6.3, and the right is the coherence image estimated by the same way as in Fig.6.6. Again, there exist some pixels of high correlation, explaining the discrepancy between the theory and experimental results seen in Fig.6.8.

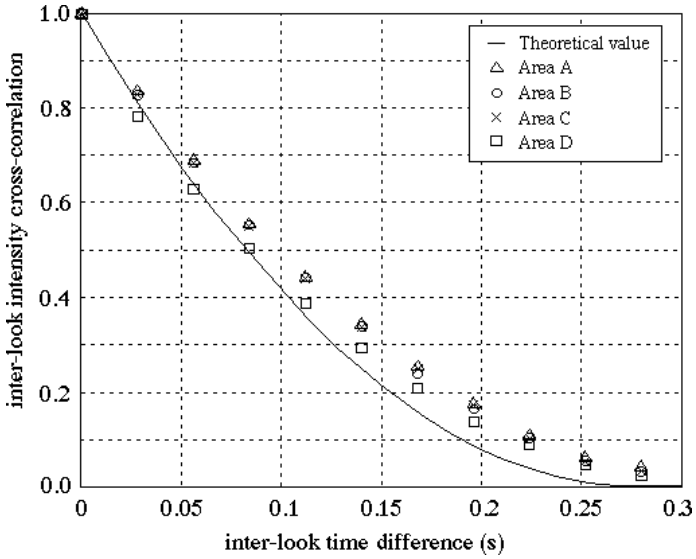

Figure 6.8: The interlook cross-correlation function of the area "A", "B", "C" and "D" in the RADARSAT-1 SAR image shown in Fig.6.3 as a function of the center time difference. The solid line is the theoretical curve based on equation (6.15).

The look 1 to look 11 sub-images of the test areas in Fig.6.3 are shown in Fig.D5- Fig.D8 in the Appendix D. As in the Tsugaru images of Fig.D1- Fig.D4, gradual changes in speckle patterns with increasing look number difference can be seen.

The CCF measurements given by Fig.6.8 provide a further support to the theoretical result of equation (6.15) on the cross-correlation function of speckle intensity in the images produced by partially overlapped sub-apertures.

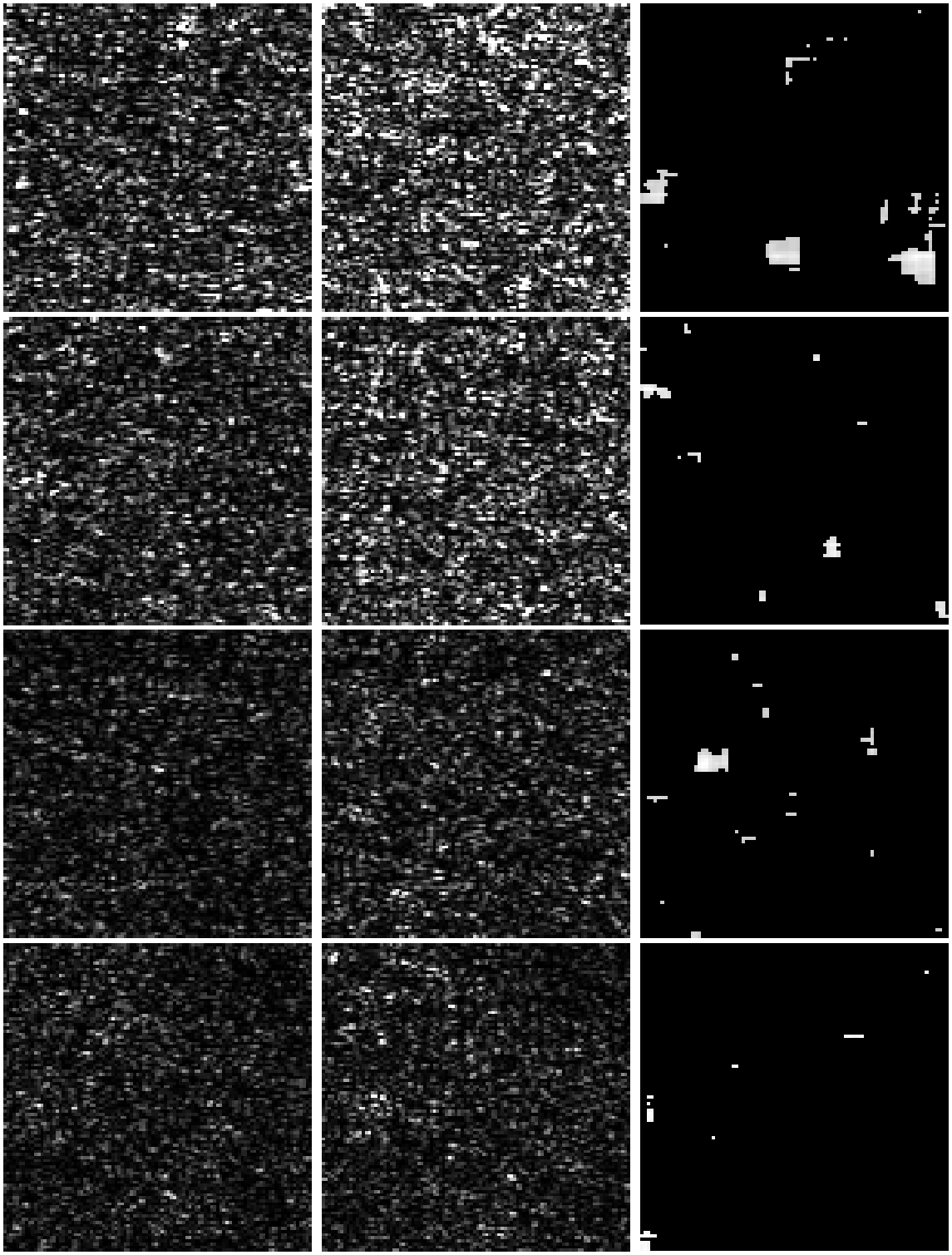

Figure 6.9: The left and center images from top to bottom are respectively the look 1 and 11 images of the area "A", "B", "C", and "D" in Fig.6.3. The right images are the corresponding coherence images produced by cross-correlating the look 1 and 11 images with moving windows of size 10 $\times$ 10 pixels, and thresholding by the correlation value of 0.35.

6.4 Summary

A general integral expression is derived for the intensity CCF of interlook speckle patterns in the sub-images processed with partially overlapped sub-apertures, and a simple analytical expression is derived for a rectangular sub-aperture weighting function. The results show that, for statistically white (spatially homogeneous non-correlated) backscattered fields which give rise to the classical Gaussian speckle, the CCF depends only on the amplitude weighting function and center time difference of sub-apertures; and that it is independent of the temporal correlation properties of the backscattered fields. This theoretical conclusion is supported by the JERS-1 L-band and RADARSAT-1 C-band SAR images over the coastal waters of Japan.

Chapter 7

Conclusions

In this thesis, the statistical characteristics of speckle in SAR systems are investigated with applications to forestry and oceanography. Gaussian speckle is formed as a result of random interference from many coherent contributions within a resolution cell, and it does not carry information on the scattering objects. Gaussian speckle is therefore often treated as unwanted noise. Non-Gaussian speckle, on the other hand, arises from small number of scatterers, and hence it does carry information on the scattering objects. These properties of Gaussian and non-Gaussian speckle patterns are described using simulated speckle as examples in Chapter 2.

In order to understand SAR speckle, it is necessary to capture the concept of SAR image formation, and the fundamentals of SAR systems are described in Chapter 3. In Chapter 4, the theory of SAR polarimetry is described. Although polarimetry is not the main theme of this thesis, it is useful to distinguish the types of scattering from different objects, and to provide a complementary support to understanding of speckle in SAR images of low and high vegetation. The polarimetric analyses are applied to the airborne Pi-SAR data over the rice fields and Tomakomai forests.

The applications of SAR speckle to forestry described in Chapter 5 are based on the high-resolution polarimetric Pi-SAR data over the coniferous forests in Tomakomai, Hokkaido, Japan. The relations between RCS of X- and L-bands data and forest parameters are first investigated. It is found that there are fairly well-defined relations between RCS and tree parameters within limited ranges. The largest RCS at X-band is VV- followed by HH- and HV-polarizations, and at L-band is HH- followed by VV- and HV-polarizations. The L-band RCS saturation levels are found approximately to the biomass of 40 tons/ha, the tree age of 30 years, the basal area of 30 m^2/ha, and the tree height of 8 m. However, X-band RCS saturation levels are difficult to define. The L-band RCS data can therefore be used to estimate the forest biomass up to a certain level.

Among the Rayleigh, log-normal, Weibull and K-distributions, the estimated PDFs of L-band image amplitude are found to fit best to the K-distribution according to AIC. The correlation coefficient is then estimated between the order parameter of the K-distribution and the forest parameters. The highest corre-

lation is obtained between the order parameter of cross-polarization data and tree biomass, where the order parameter increases consistently with increasing biomass for all polarizations. Thus, the order parameter of the K-distribution in the cross-polarization data are used to estimate the forest biomass beyond the saturation limits of the RCS measurements. The accuracy of the regression model based on the ground-truth data collected in 2002 and 2003 is examined from the comparison of the model prediction with the ground-truth data collected in 2005. As a result the accuracy of 85% is obtained. Finally, a new regression model is developed taking into account all ground-truth data, and a map of biomass in the forests around the test sites is produced. The regression model developed in this study can certainly be used to estimate the biomass of coniferous forests on fairly flat ground in Hokkaido. Applicability of the model to the forests on sloped ground and forests consisting of broadleaf trees is not known.

The applications of SAR speckle to oceanography described in Chapter 6 are to examine the hypothesis of partially overlapped multilook processing technique over dynamic sea surface. The general expression is derived for the intensity CCF of interlook speckle patterns in the sub-images processed with partially overlapped sub-apertures. It is shown that the interlook cross-correlation function of spackle intensity is given by the modulus square of the autocorrelation function of the amplitude weighting function of sub-apertures. For statistically white backscattered fields which give rise to classical Gaussian speckle, the interlook CCF is independent of the scene coherence time of sea surface; and it is depends only on the amplitude weighting function and center time difference of sub-apertures. To verify our theory, experiments were carried out by using JERS-1 L-band and RADARSAT-1 C-band SAR data over the coastal waters of Japan, and good agreement is obtained for both the data though small discrepancy is found to be caused by locally correlated small features between looks.

References

[1] J.C.Dainty (ed.), *Laser Speckle and Related Phenomena*, Berlin: Springer-Verlag, 1975.

[2] D. E. Kerr (ed.), *Propagation of Short Radio Waves*, McGraw-Hill Book Company, New York, 1951

[3] J.W.Goodman, "Statistical properties of laser speckle patterns," in ref. [1], pp.9-77.

[4] K.Ouchi, *First-order Statistics of Speckle from Hard-edged Apertures*, Ph.D thesis, University of London, 1980.

[5] B.R.Frieden, *Probability, Statistical Optics, and Data Testing*, New York: Springer, 1983.

[6] A.Papoulis, *Probability, Random Variables, and Stochastic Processes*, 3rd ed., McGraw-Hill: New York, 1991. pp.214-221.

[7] A.E.Ennos, "Speckle interferometry," in ref. [1], pp.203-254.

[8] J.C.Dainty, "Stellar speckle interferometry," in ref. [1], pp.255-280.

[9] D. Massonnet and K. L. Feigel, "Radar interferometry and its application to changes in the Earth's surface," *Reviews of Geophysics*, vol.36, pp.441-500, 1998.

[10] P. A. Rosen, S. Hensley, I. R. Joughin, F. K. Li, S. N. Madsen, E. Rodriguez, and R. M. Goldstein, "Synthetic aperture radar interferometry, *Proc. IEEE*, vol. 88, pp. 333-382, Mar. 2000.

[11] W.T.Welford, "Optical estimation of statistics of surface roughness from light scattering measurements," *Opt. Quant. Elect.*, pp. 269-287, vol. 9, 1977.

[12] M.Francon, "Information processing using speckle patterns," in ref. [1], pp.171-202.

[13] T.S.Mckechnie, "Speckle reduction," in ref. [1], pp.123-170.

[14] J.S.Lee and I.Jurkevich, "Speckle filtering of synthetic aperture radar imagery: a review," *Remote Sens. Rev.*, vol.8, pp.313-340, 1994.

[15] L.J.Porcello, N.G.Massey, R.B.Innes, and J.M.Marks, "Speckle reduction in synthetic aperture radar," *J. Opt. Soc. Amer.*, vol.66, pp.1305-1311, 1976.

[16] C.Oliver and S.Quegan, *Understanding Synthetic Aperture Radar Images*. London: Artech House, 1998.

[17] M.Sekine and Y.H.Mao, *Weibull Radar Clutter*. London: Peter Peregrinus, 1990.

[18] G.V.Trunk and S.F.George, "Detection of targets in non-Gaussian sea clutter," *IEEE Trans. Aerosp. Electron. Syst.*, vol.AES-6, pp.620-628, 1970.

[19] K.D.Ward, "Compound Representation of High Resolution Sea Clutter," *Electron. Lett.,* vol.17, pp. 561-565, 1981.

[20] M.P.Warden, "An Experimental Study of Some Clutter Characteristics," *AGARD Conf. Proc. on Advanced Radar Systems,* no.66, 1970.

[21] E.Jakeman and P.N.Pusey, "A model for non-Rayleigh sea echo," *IEEE Trans. Antennas Propagat.*, vol.AP-24, pp.806-814, 1976.

[22] E.Jakeman, "On the statistics of *K*-distributed noise," *J. Phys. A: Math. Gen.*, vol.13, pp.31-48, 1980.

[23] C.J.Oliver, "A model for non-Rayleigh scattering statistics," *Opt. Acta*, vol.31, pp.701-722, 1984.

[24] C.J.Oliver, "Representation of correlated clutter textures in coherent images," *Inverse Problems*, vol.4, pp.843-867, 1988.

[25] I.R.Joughin, D.B.Percival, and D.P.Winebrenner, "Maximum likelihood estimation of K distribution parameters for SAR data," *IEEE Trans. Geosci. Remote Sens.*, vol.31, pp. 989-999, 1993.

[26] Y.Deligon and W.Pieczynski, "Modeling non-Rayleigh speckle distribution in SAR images, " *IEEE Trans. Geosci. Remote Sens.*, vol.40, pp. 1430-1435, 2002.

[27] F.T.Ulaby, F.Kouyate, B.Brisco, and T.H.L.Williams, "Textural information in SAR images," *IEEE Trans. Geosci. Remote Sens.*, vol.24, pp.235-245, 1986.

[28] G.De Grandi, J-S.Lee, D.Shuler, and E.Nezry, "Texture and speckle statistics in polarimetric SAR synthesized images," *IEEE Trans. Geosci. Remote Sens.*, vol.41, pp.2070-2088, 2003.

[29] J.C.Curlander and R.N.McDonough, *Synthetic Aperture Radar: Systems and Signal Processing*. New York: John Wiley, 1991.

[30] K.Ouchi, *Synthetic Aperture Radar for Remote Sensing*, (in Japanese) Tokyo Denki Daigaku Press, Tokyo, 2004.

[31] X.K.Yuan, *Introduce to the Spaceborne Synthetic Aperture Radar*, (in Chinese) National Defence Industry Press, Beijing, 2003.

[32] C.B.Zhang, *Synthetic Aperture Radar, Theory, System Analysis, and Application*, (in Chinese) Science Press, Beijing, 1989.

[33] M.I.Skolnik, *Radar Handbook* (2nd Ed.), McGraw-Hill: New York, 1990.

[34] M.Hellmann, *SAR Polarimetry Tutorial* (Beta version 0.1a), 2001.

[35] S.R.Cloude and E.Pottier, "An Entropy Based Classification Scheme for Land Applications of Polarimetric SAR," *IEEE Trans. Geosci. Remote Sens.*, vol.35, pp.68-78, 1997.

[36] A.Freeman and S.L.Durden, "A Three-Component Scattering Model for Polarimetric SAR Data," *IEEE Trans. Geosci. Remote Sens.*, vol.36, pp. 963-973, 1998.

[37] Y.Yamaguchi, T.Moriyama, M.Ishido, and H.Yamada, "Four-component scattering model for polarimetric SAR image decomposition," IEEE Trans. Geosci. Remote Sens., vol.43, pp.1699-1706, 2005.

[38] F.T.Ulaby, K.Sarabandi, K.McDonald, M.Whitt, and M.C.Dobson, "Michigan microwave canopy scattering model," *Int. J. Remote Sens.*, vol.11, pp.1223-1253, 1990.

[39] K.McDonald, M.C.Dobson,, and F.T.Ulaby, "Modeling multifrequency diurnal backscatter from a walnut orchard," *IEEE Trans. Geosci. Remote Sens.*, vol.29, pp.852-863, 1991.

[40] P.Ferrazzoli and L.Guerriero, "Radar sensitivity to tree geometry and woody volume: a model analysis," *IEEE Trans. Geosci. Remote Sens.*, vol.33, pp.360-371, 1995.

[41] M.L.Imhoff, "A theoretical analysis of the effect of forest structure on synthetic aperture radar backscatter and the remote sensing of biomass," *IEEE Trans. Geosci. Remote Sens.*, vol.33, pp.341-352, 1995.

[42] M.Moghaddam and S.Saatchi, "Analysis of scattering mechanisms in SAR imagery over boreal forest: results from BOREAS'93," *IEEE Trans. Geosci. Remote Sens.*, vol.33, pp.1920-1926, 1995.

[43] Y.H.Hussin, R.M.Reich, and R.M.Hoffer, "Estimating slash pine biomass using radar backscatter," *IEEE Trans. Geosci. Remote Sens.*, vol.29, pp.427-431, 1991.

[44] M.C.Dobson, F.T.Ulaby, T.L.Toan, A.Beaudoin, E.S.Kasischke, and N. Christensen, "Dependence of radar backscatter on coniferous forest biomass," *IEEE Trans. Geosci. Remote Sens.*, vol.30, pp.412-415, 1992.

[45] T.L.Toan, A. Beaudoin, J.Riom, and D. Guyon, "Relating forest biomass to SAR data," *IEEE Trans. Geosci. Remote Sens.*, vol.30, pp.402-411,1992.

[46] K.J.Ranson and Q.Sun, "Mapping biomass of a northern forest using multifrequency SAR data," *IEEE Trans. Geosci. Remote Sens.*, vol.32, pp.388-396, 1994.

[47] E.Rignot, C.Williams, J.B.Way, and L.Viereck, "Radar estimates of aboveground biomass in boreal forests of interior Alaska," *IEEE Trans. Geosci. Remote Sens.*, vol.32, pp.1117-1124, 1994.

[48] M.L.Imhoff, "Radar backscatter and biomass saturation: ramifications for global biomass inventory," *IEEE Trans. Geosci. Remote Sens.*, vol.33, pp.511-518, 1995.

[49] L.Kurvonen, J.Pulliainen, and M.Hallikainem, "Retrieval of biomass in boreal forests from multitemporal ERS-1 and JERS-1 SAR images," *IEEE Trans. Geosci. Remote Sens.*, vol.37, pp.198-205, 1999.

[50] E.Rignot, C.Williams, J.B.Way, and L.Viereck, "Mapping of forest types in Alaskan boreal forests using SAR imagery," *IEEE Trans. Geosci. Remote Sens.*, vol.32, pp.1052-1060, 1994.

[51] T.M.Kuplich, *Temporal, spatial, spectral and polarisation characteristics of the SAR backscatter from regenerating tropical forests*, (Ph.D thesis), University of Southampton, Dec., 2001.

[52] J.P.Pulliainen, P.J.Mikkela, M.T.Hallikainen, and J-P Ikonen, "Seasonal dynamics of C-band backscatter of boreal forests with applications to biomass and soil moisture estimation," *IEEE Trans. Geosci. Remote Sens.*, vol.34, pp.758-770, 1996.

[53] H.Wang, K.Ouchi, M.Watanabe, M.Shimada, T.Tadono, A.Rosenqvist, S.A.Romshoo, M.Matsuoka, T.Moriyama, and S.Uratsuka, "In Search of the Statistical Properties of High-Resolution Polarimetric SAR Data for the Measurements of Forest Biomass beyond the RCS Saturation Limits," (has been accepted by *IEEE Trans. Geosci. Remote Sens. Lett.*.

[54] H.Wang, K.Ouchi, "The relation between the order parameter of *K*-distribution in high-resolution polarimetric SAR data and forest biomass," *Proc. IGARSS, Soul, Korea*, Jul. 2005 (DVD).

[55] S.R.Cloude and E.Pottier, "A review of target decomposition theorems in radar polarimetry," *IEEE Trans. Geosci. Remote Sens.*, vol.34, pp.498-518, 1996.

[56] J.S.Lee, S.R.Cloude, K.P.Papathanassiou, M.R.Grunes, and I.H.Woodhouse, "Speckle filtering and coherence estimation of polarimetric SAR interferometry data for forest applications, *IEEE Trans. Geosci. Remote Sens.*, vol.41, pp.2254-2263, 2003.

[57] L.Kurvonen and M.T.Hallikainen, "Textural information of multitemporal ERS-1 and JERS-1 SAR images with applications to land and forest type classification in boreal zone," *IEEE Trans. Geosci. Remote Sens.*, vol.37, pp.680-689, 1999.

[58] C.J.Oliver, "Rain forest classification based on SAR texture," *IEEE Trans. Geosci. Remote Sens.*, vol.38, pp.1095-1104, 2000.

[59] T.Kobayashi, T.Umehara, M.Satake, A.Nadai, S.Uratsuka, T.Manabe, H.Masuko, M.Shimada, H.Shinohara, H.Tozuka, and M.Miyawaki, "Airborne dual-frequency polarimetric and interferometric SAR," *IEICE Trans. Commun.*, vol.E83-B, No.9, pp.1945-1954, 2000.

[60] Project department, Forestry Agency Ed., Stand volume table -East Japan-, Japan Forestry investigation committee, Oct. 1998.

[61] K.Ouchi and R.E.Burge, "Speckle cross-correlation function in multilook SAR images of moving discrete scatterers," *Int. J. Remote Sens.*, vol.12, pp.1933-1946, 1991.

[62] H.Goldstein, "The fluctuations of clutter echos, " in *Propagation of Short Radio Waves*, MIT Rad. Lab. Series 13, D.E.Kerr, Ed. McGraw-Hill: New York, 1951, p.554.

[63] R.K.Raney, "SAR response to partially coherent phenomena," *IEEE Trans. Antennas Propagat.*, vol.28, pp.777-787, 1980.

[64] W.R.Alpers and C.Brüning, "On the relative importance of motion-related contributions to the SAR imaging mechanism of ocean surface waves," *IEEE Trans. Geosci. Remote Sens.*, vol.24, pp.873-885, 1986.

[65] R.E.Crande, "Estimating ocean coherence time using dual-baseline interferometric synthetic aperture radar," *IEEE Trans. Geosci. Remote Sens.*, vol.32, pp.846-854, 1994.

[66] S.J.Frasier and A.J.Camps, "Dual-beam interferometry for ocean surface current vector mapping," *IEEE Trans. Geosci. Remote Sens.*, vol.39, pp.401-414, 2001.

[67] D.P.Kasilingham and O.H.Shemdin, "Theory for synthetic aperture radar imaging of the ocean surface: With application to the tower ocean wave and radar dependence experiment of focus, resolution and wave height spectra," *J. Geophys. Res.*, vol.93, no.C11, 13837-13848, 1988.

[68] W.J.Plant and W.C.Keller, "Evidence of Bragg scattering in microwave Doppler spectra of sea return," *J.Geophys. Res.*, vol.95, no.C9, pp.16299-16310, 1990.

[69] L.Shemer and M.Marom, "Estimates of ocean coherence time by an interferometric SAR," *Int. J. Remote Sens.*, vol.14, no.16, pp.3021-3029, 1993.

[70] M.J.Tucker, "The decorrelation time of microwave radar echoes from the sea surface," *Int. J. Remote Sens.*, vol.6, pp.1075-1089, 1985.

[71] R.K.Raney and P.W.Vachon, "Synthetic aperture radar imaging of ocean waves from an airborne platform: focus and tracking issues," *J. Geophy. Res.*, vol.93, C10, pp.12,475-12,486, 1988.

[72] C.J.Oliver, "The representation of radar sea clutter," *Proc. IEE, Pt. F*, vol.135, pp.497-500.

[73] K.Ouchi and R.A.Cordey, "Statistical analysis of azimuth streaks observed in digitally processed CASSIE imagery of sea surface," *IEEE Trans. Geosci. Remote Sens.*, vol.29, pp.727-735, 1991.

[74] K.Ouchi and H.Mitsuyasu, "Determination of ocean wave propagation direction by split-look processing using JERS-1 SAR data," *IEEE Trans. Geosci. Remote Sens.*, vol.37, pp.849-855, 1999.

[75] K.Ouchi, S.Tamaki, H.Yaguchi, and M.Iehara "Ship detection based on coherence image derived from cross-correlation of multilook SAR images" *IEEE Trans. Geosci. Remote Sens. Lett.*, vol.1, pp.184-187, 2004.

[76] K.Ouchi and H.Wang, "Interlook cross-correlation function of speckle in SAR images of sea surface processed with partially overlapped subapertures," *IEEE Trans, Geosci. Remote Sens.*, vol.43, pp.695-701, Apr. 2005.

[77] Y.Nemoto, H.Nishio, M.Ono, H.Mizutamari, K.Nishioka and K.Tanaka, "Japanese earth resources satellite-1 synthetic aperture radar," *Proc. IEEE*, vol.79, pp.800-809, 1991.

[78] R.K.Raney, A.P.Luscombe, E.J.Langham, and A.Ahmed, "RADARSAT," *Proc. IEEE*, vol.79, pp.839-849, 1991.

[79] S.Sayama and M.Sekine, "Weibull, log-Weibull and K-distributed ground clutter modeling analyzed by AIC," *IEEE Trans. Aerosp. Electron. Syst.*, vol.37, pp.1108-1113, 2001.

[80] R.J.A. Tough and K.D. Ward, " The correlation properties of gamma and other non-Gaussian processes generated by memoryless nonlinear transformation," *J. Phys. D: Appl. Phys.*, vol. 32, pp.3705-3084, 1999.

[81] G.Davison,*www.radarworks.com*.

[82] D. Blacknell, "New method for the simulation of K distributed clutter.", *IEE Proc. Radar, Sonar and Navigation,* vol.141, pp. 53-58, 1994.

[83] S.J.Wu, "Estimations of the Parameters of the Weibull Distribution with Progressively Censored Data," *J. Japan Statist. Soc.*, vol. 32, no.2, pp. 155-163, 2002.

[84] D.O.North, "An analysis of the factors whice determine signal/noise discrimination in pulsed-carrier systems," *Proc. IEEE* 51 (1963), 1016-1027 (reprint of *RCA Technical Report PTR-6C*, Jun. 25, 1943).

[85] K.Ouchi, H.Wang, N.Ishitsuka, G.Saito, and K.Mohri, "On the Bragg Scattering Observed in L-band Synthetic Aperture Radar Images of Flooded Rice Fields," (accepted by *IEICE Trans. Commun.*).

[86] Meteorological Society of Japan, *Encyclopedia of Meteorology and Atmospheric Sciences,* Tokyo Shoseki Press, Tokyo, 1998.

[87] T.Tsujii, S.Umezawa, and T.Satou, *Common Trees of Hokkaido,* Hokkaido University Press, 1992.

[88] H.Akaike, "A New Look at the Statistical Model Identification," *IEEE Trans. Automat. Contr.*, vol.AC-19, pp. 716-723, 1974.

[89] A.J.F.Siegert, "On the fluctuations in signals returned by many independently moving scatterers," *MIT Rad. Lab. Rep.*, no.465, 1943.

[90] A.M.Smith, "A new approach to range-Doppler SAR processing," *Int. J. Remote Sens.*, vol.12, pp.235-51, 1991.

Appendix A

Siegert Relation

In chapter 2, we only discussed first-order statistical properties. First-order statistics describe the statistical properties of a point in space or for time-varying speckle, in space-time. To describe the coarseness of the spatial structure of speckle, the second-order statistics is necessary. The autocorrelation function (ACF) is frequently used. For simplification, here only one dimension autocorrelation function is given. The autocorrelation of complex amplitude is given by

$$\langle A(x_1)A^*(x_2)\rangle = \frac{1}{N}\sum_{j=1}^{N}\sum_{j'=1}^{N}\langle a(x_j)a^*(x_{j'})\rangle E_A(X_1-x_j)E_A^*(X_2-x_{j'}) \tag{A.1}$$

Here, we assume the speckle is Gaussian distributed. The phases are random and uncorrelated to each other. Therefore, in equation (A.1), the items are zero for $j \neq j'$ and the contributions are only from the items with $j = j'$. Equation (A.1) can then be simplified to

$$\langle A(x_1)A^*(x_2)\rangle = \frac{\langle\sigma\rangle}{N}\sum_{j=1}^{N}E_A(X_1-x_j)E_A^*(X_2-x_j) \tag{A.2}$$

Now, let's deduce the ACF of image intensity. Again, only one dimension result is given. Since the intensity is the module square of amplitude, the intensity ACF is the given by

$$\begin{aligned}\langle I(x_1)I(x_2)\rangle &= \langle A(X_1)A^*(X_1)A(X_2)A^*(X_2)\rangle \\ &= \frac{1}{N^2}\sum_{j,}^{N}\sum_{j',}^{N}\sum_{j'',}^{N}\sum_{j'''=1}^{N}\langle a(x_j)a^*(x'_j)a(x_{j''})a^*(x_{j'''})\rangle \\ &\cdot\ E_A(X_1-x_j)E_A^*(X_1-x_{j'})E_A(X_2-x_{j''})E_A^*(X_2-x_{j'''})\end{aligned} \tag{A.3}$$

Again, white noise approximation is used to simplify equation (A.3). The items in equation (A.3) are not 0 only for the following conditions:

1. when $j = j' \neq j'' = j'''$, all together $N(N-1)$ items
2. when $j = j''' \neq j' = j''$, all together $N(N-1)$ items

3. when $j = j' = j'' = j'''$, all together N items

There are only N items satisfy condition 3, these items can be ignored for large N comparing to the items of condition 1 and 2. Equation (A.3) then becomes

$$\begin{aligned}\langle I(x_1)I(x_2)\rangle &= \frac{1}{N^2}\sum_{j\neq}^{N}\sum_{j'=1}^{N}\langle\sigma(x_j)\sigma(x_{j'})\rangle[|E_A(X_1-x_j)|^2|E_A(X_2-x_{j'})^2| \\ &\quad +E_A(X_1-x_j)E_A^*(X_1-x_{j'})E_A(X_2-x_{j'})E_A^*(X_2-x_j)] \end{aligned} \tag{A.4}$$

Further, because RCS is uncorrelated to space, that is,

$$\langle\sigma(x_j)\sigma(x_j')\rangle = \langle\sigma(x_j)\rangle\langle\sigma(x_j')\rangle = \langle\sigma\rangle^2 \tag{A.5}$$

Substituting equation (A.5) into equation (A.4), we can get

$$\begin{aligned}\langle I(x_1)I(x_2)\rangle &= \frac{\langle\sigma\rangle^2}{N^2}\sum_{j\neq}^{N}\sum_{j'=1}^{N}\Big[|E_A(X_1-x_j)|^2|E_A(X_2-x_j')^2| \\ &\quad +E_A(X_1-x_j)E_A^*(X_1-x_{j'})E_A(X_2-x_{j'})E_A^*(X_2-x_j)\Big] \end{aligned} \tag{A.6}$$

It can be rewritten as

$$\langle I(x_1)I(x_2)\rangle = \left|\frac{\langle\sigma\rangle}{N}\sum_{j=1}^{N}|E_A(X_1-x_j)|^2\right|^2 + \left|\frac{\langle\sigma\rangle}{N}\sum_{j=1}^{N}E_A(X_1-x_j)E_A^*(X_2-x_j)\right|^2 \tag{A.7}$$

By using equation (A.2), the intensity ACF can be expressed as

$$\langle I(X_1)I(X_2)\rangle = \langle I\rangle^2 + |\langle A(X_1)A^*(X_2)\rangle|^2 \tag{A.8}$$

It can be seen from equation (A.8) that the intensity ACF depends only on the spatial difference X', and equation (A.8) is called Siegert relation.

Appendix B

K-distribution of Multilook Images

The disadvantage of Weibull distribution is that it cannot be used to describe multilook data. However, K-distribution does not have this limitation. For N-look intensity image, the PDF of the speckle contribution n is

$$P(n) = \frac{N^N n^{N-1}}{\Gamma(N)} \exp\left[-Nn\right] \tag{B.1}$$

By combing the noise PDF with the Gamma RCS PDF, and the image intensity PDF can be given by [16]

$$\begin{aligned} P(I) &= \int_0^\infty P(I \mid \sigma) P(\sigma) d\sigma \\ &= \frac{2}{\Gamma(N)\Gamma(\nu)} \left(\frac{N\nu}{< I >}\right)^{(N+\nu)/2} \times I^{(N+\nu-2)/2} K_{\nu-N}\left[2\left(\frac{\nu N I}{\langle I \rangle}\right)^{1/2}\right] \end{aligned} \tag{B.2}$$

where $K_{\nu-N}[\cdot]$ is the modified Bessel function of order $\nu - N$. The normalized nth moments are given by

$$\frac{\langle I^n \rangle}{\langle I \rangle^n} = \frac{\Gamma(N+n)}{N^n \Gamma(N)} \frac{\Gamma(N+n)}{\nu^n \Gamma(\nu)} \tag{B.3}$$

The corresponding amplitude distribution is then given by

$$\begin{aligned} P(A) &= \int_0^\infty P(A|\sigma) P(\sigma) d\sigma \\ &= \frac{4}{\Gamma(N)\Gamma(\nu)} \left(\frac{N\nu}{\langle I \rangle}\right)^{(N+\nu)/2} \times A^{N+\nu-1} K_{\nu-N}\left[2A\left(\frac{\nu N}{\langle I \rangle}\right)^{1/2}\right] \end{aligned} \tag{B.4}$$

and the moments are:

$$\langle A^n \rangle = \langle I \rangle^{n/2} \frac{\Gamma(N + n/2)}{N^{n/2}\Gamma(N)} \frac{\Gamma(\nu + n/2)}{\nu^{n/2}\Gamma(\nu)} \tag{B.5}$$

The above equation is equal to normalized amplitude variance when $n = 2$.

Appendix C

L-Band Cross-Polarization Images of Tomakomai Test Sites

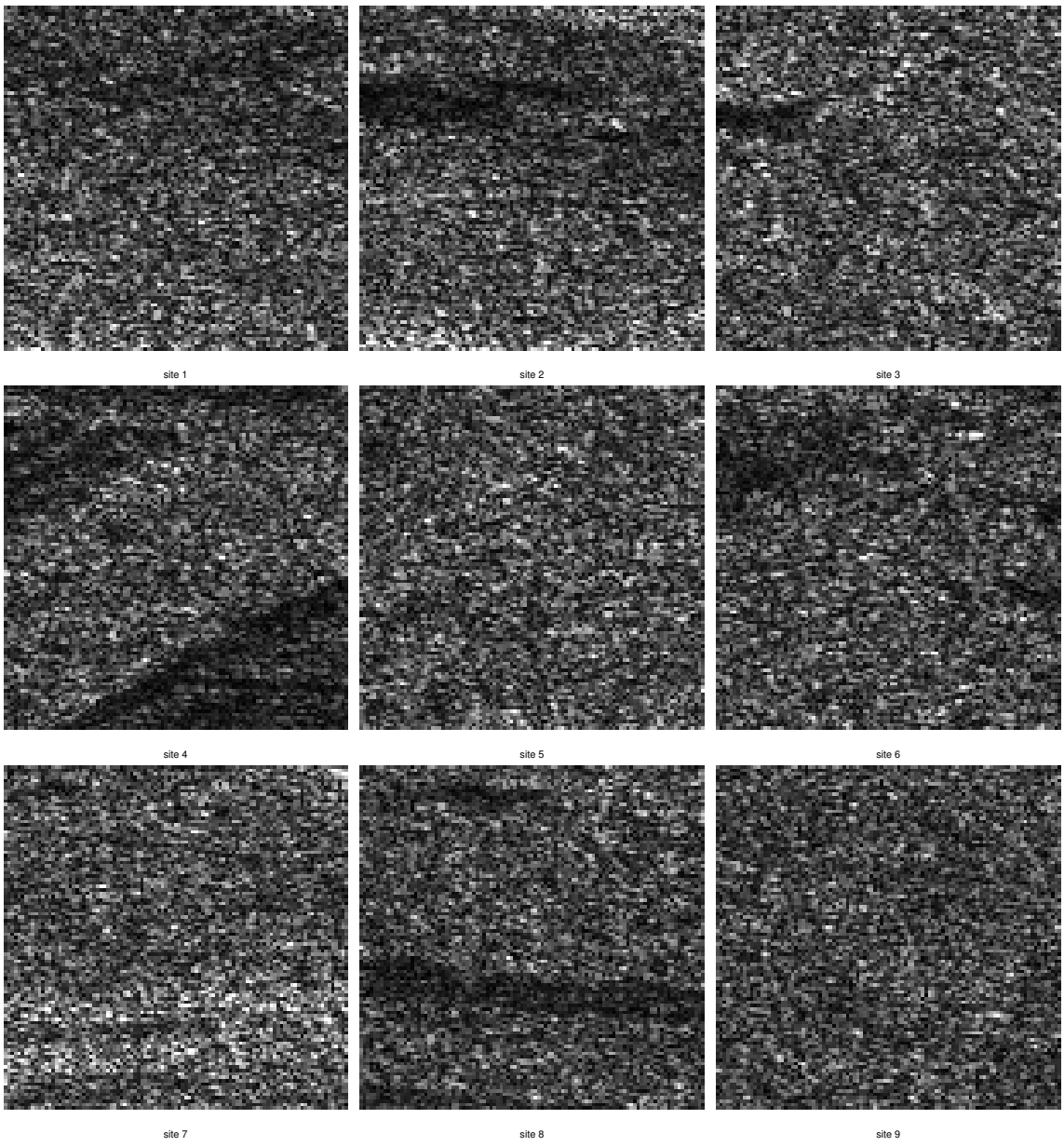

Figure C.1: L-band cross-polarization images of Tomakomai test sites 1-9. The size of each image is 100×100 pixels.

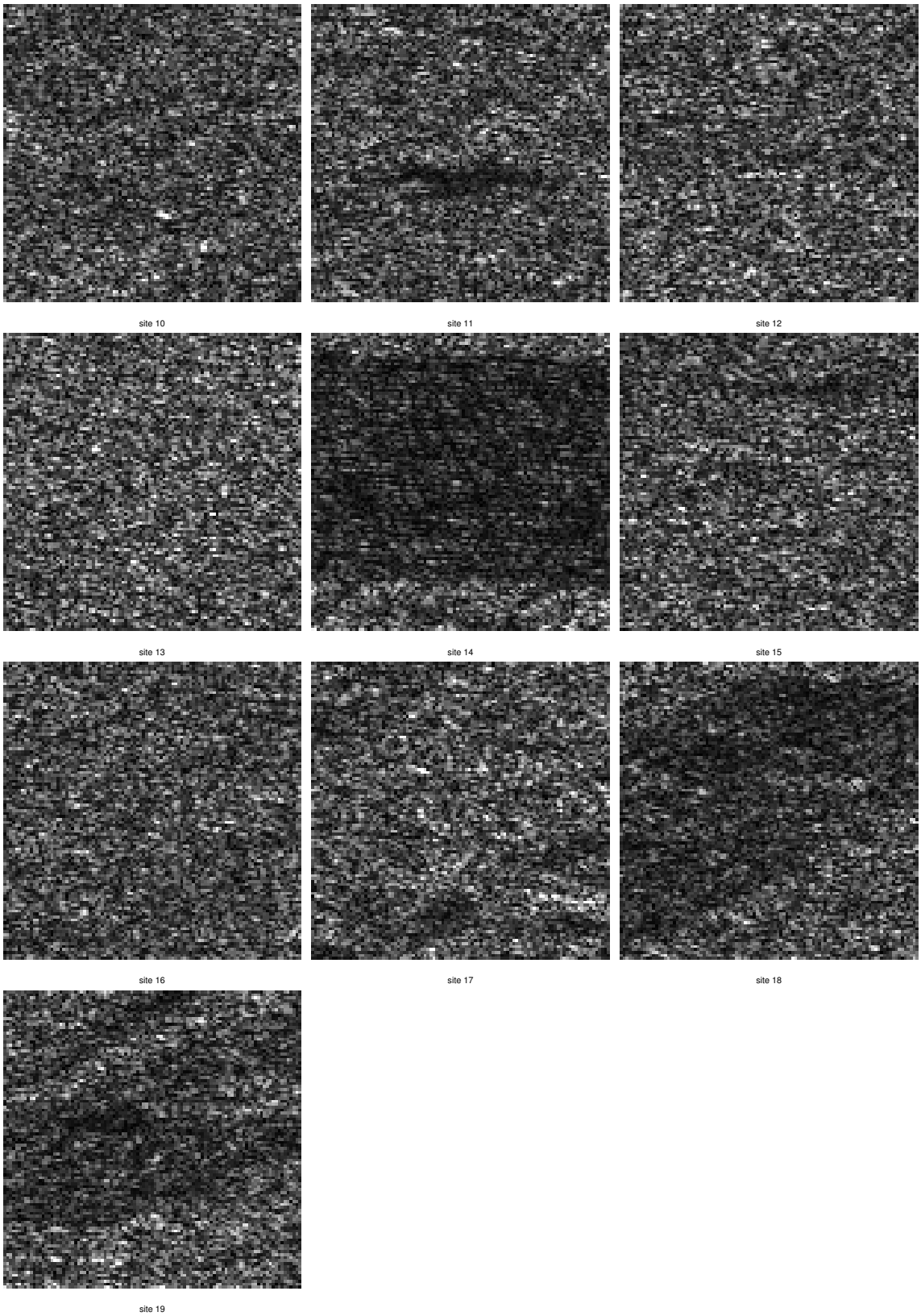

Figure C.2: L-band cross-polarization images of Tomakomai test sites 10-19. The size of each image is 100×100 pixels.

Appendix D

Sub-Images of Tsugaru Strait and Kumano Sea

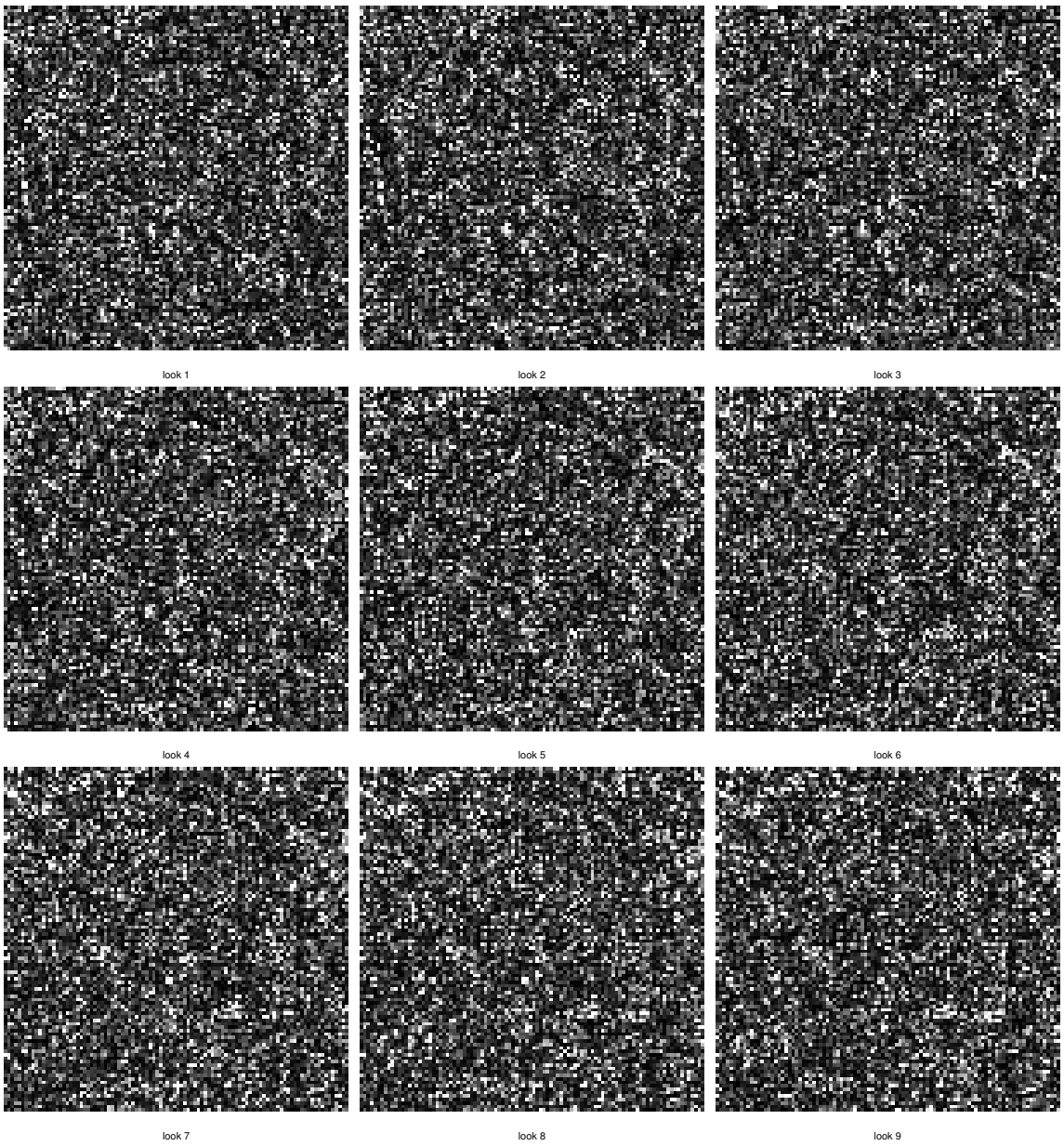

Figure D.1: Sub-images of area A in Fig.6.2.

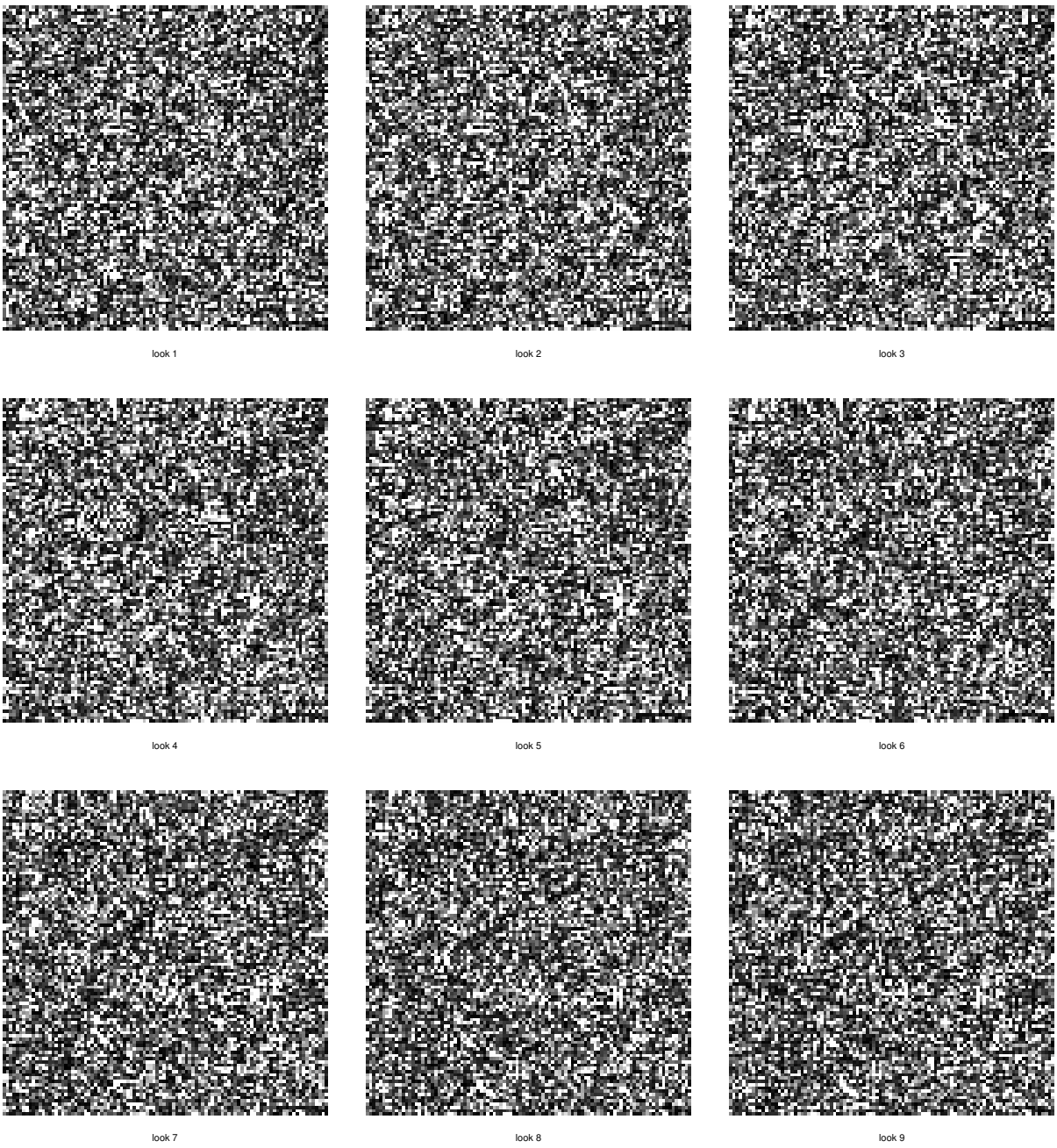

Figure D.2: Sub-images of area B in Fig.6.2.

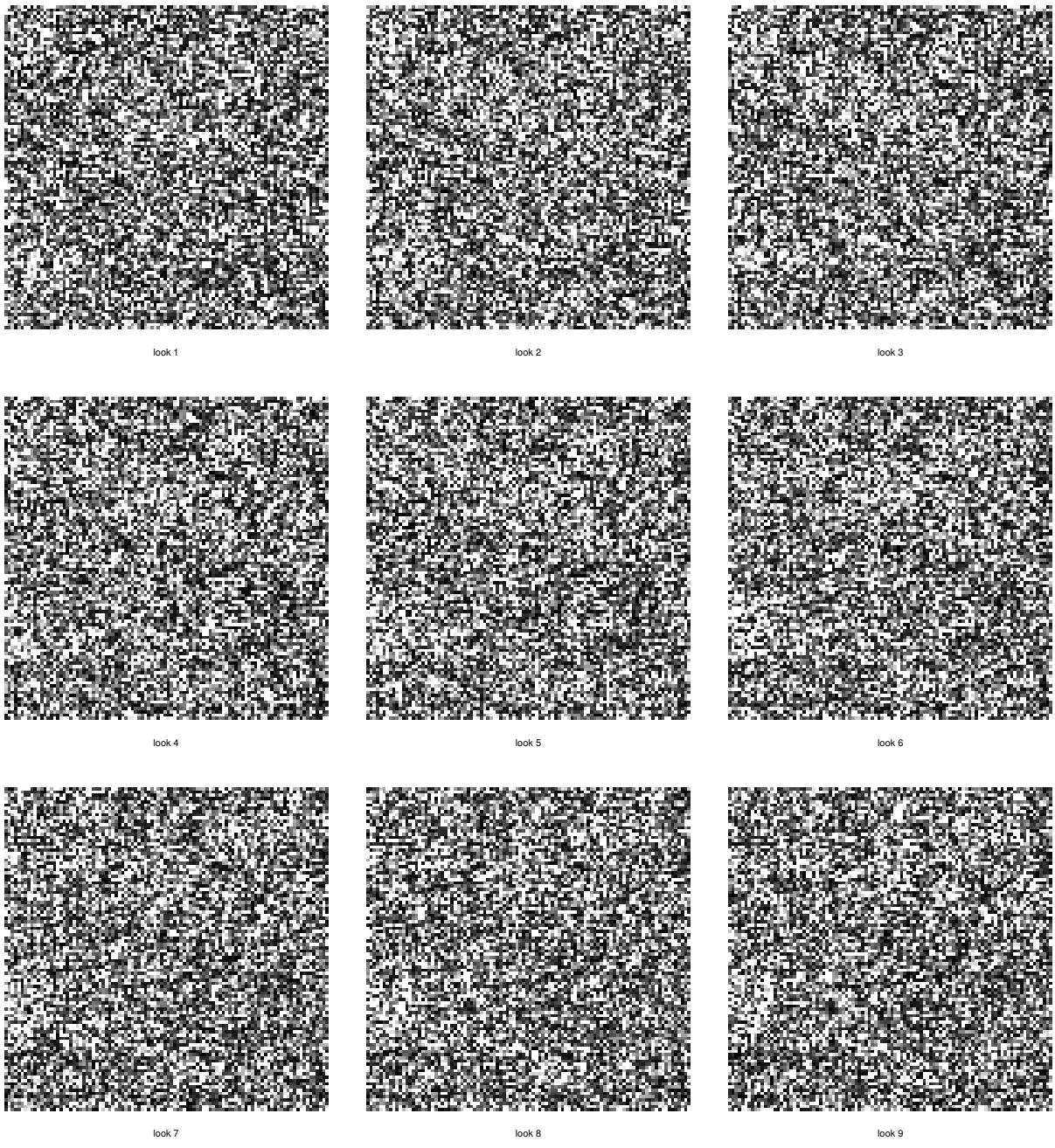

Figure D.3: Sub-images of area C in Fig.6.2.

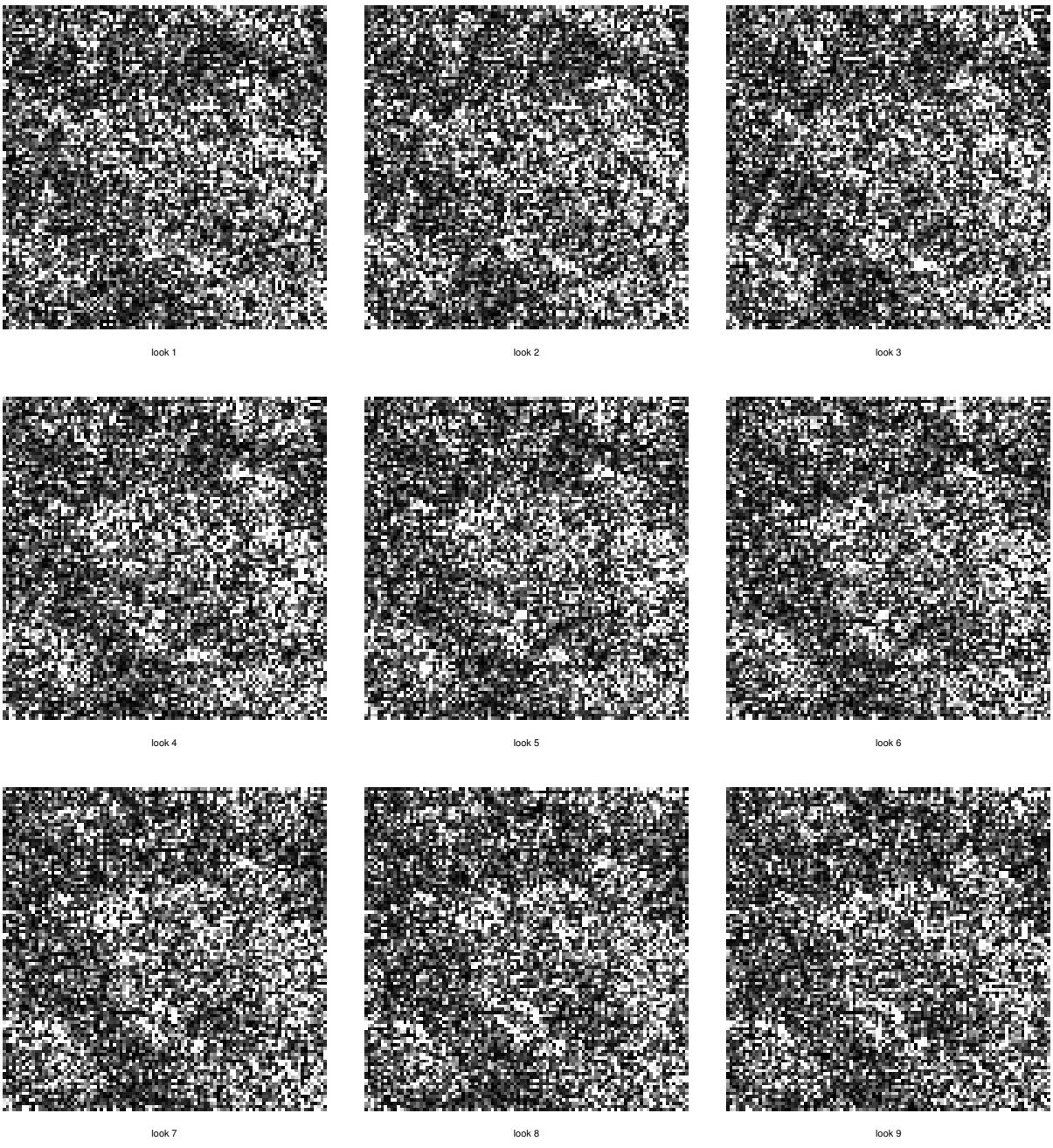

Figure D.4: Sub-images of area D in Fig.6.2.

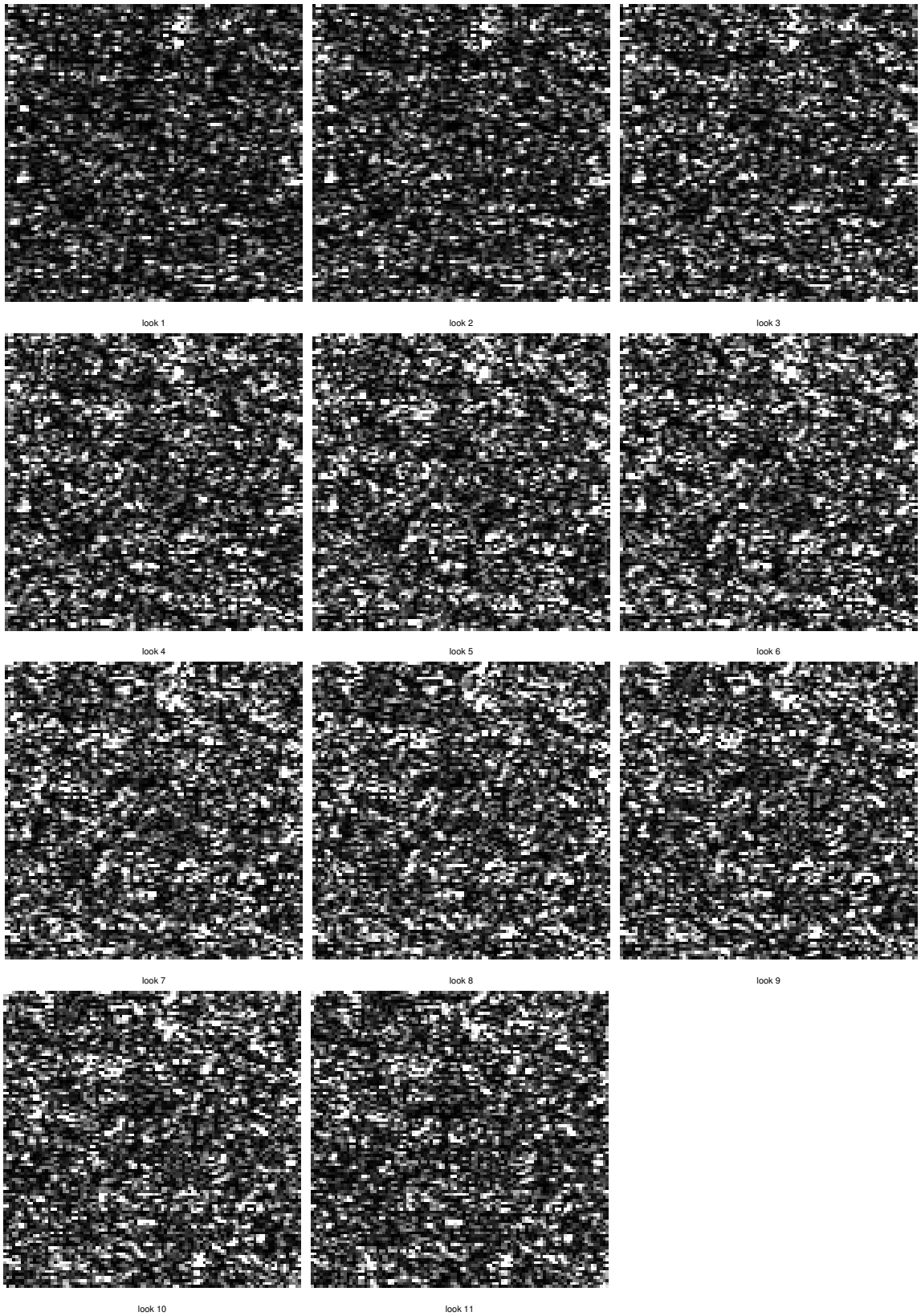

Figure D.5: Sub-images of area A in Fig.6.3.

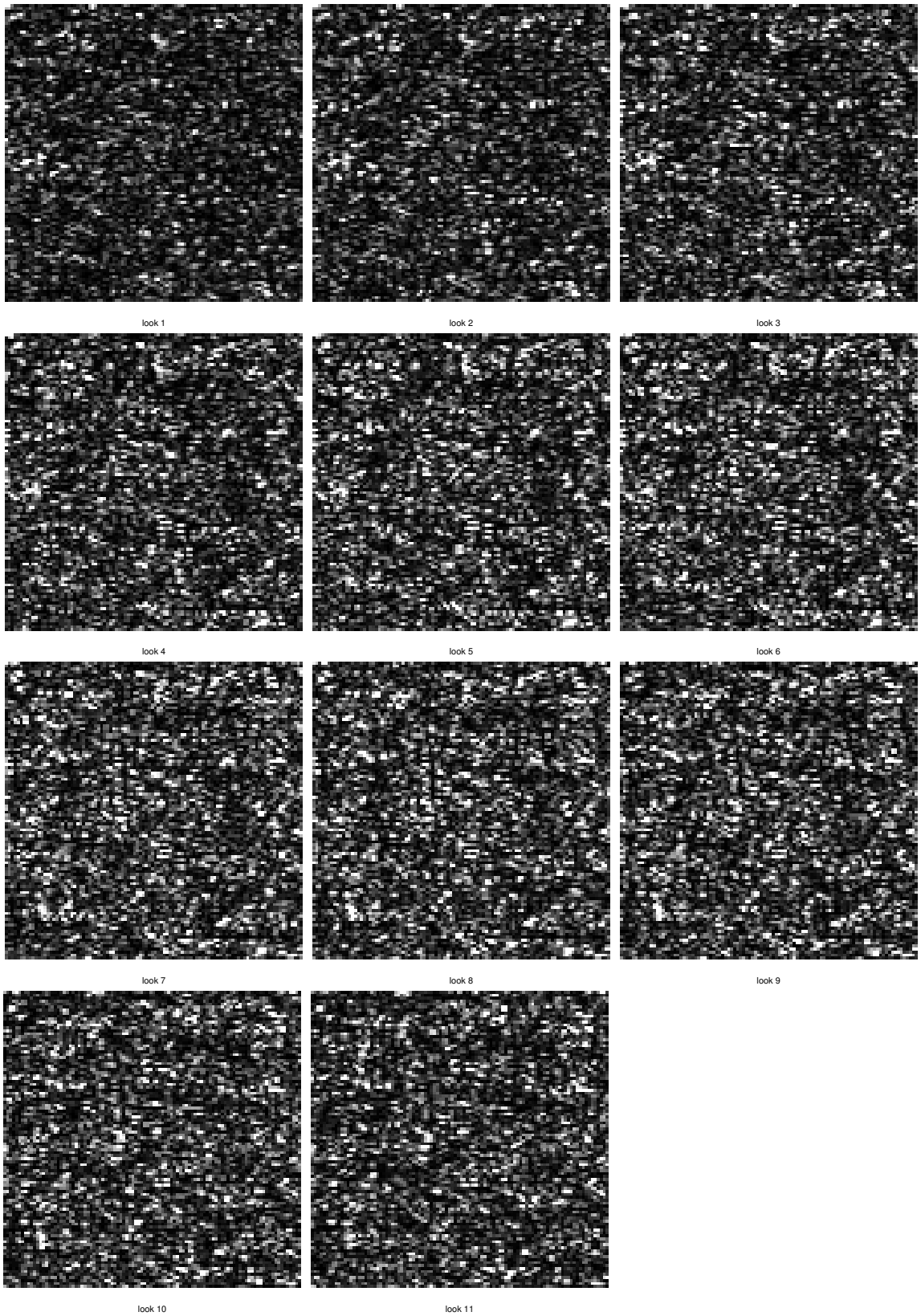

Figure D.6: Sub-images of area B in Fig.6.3.

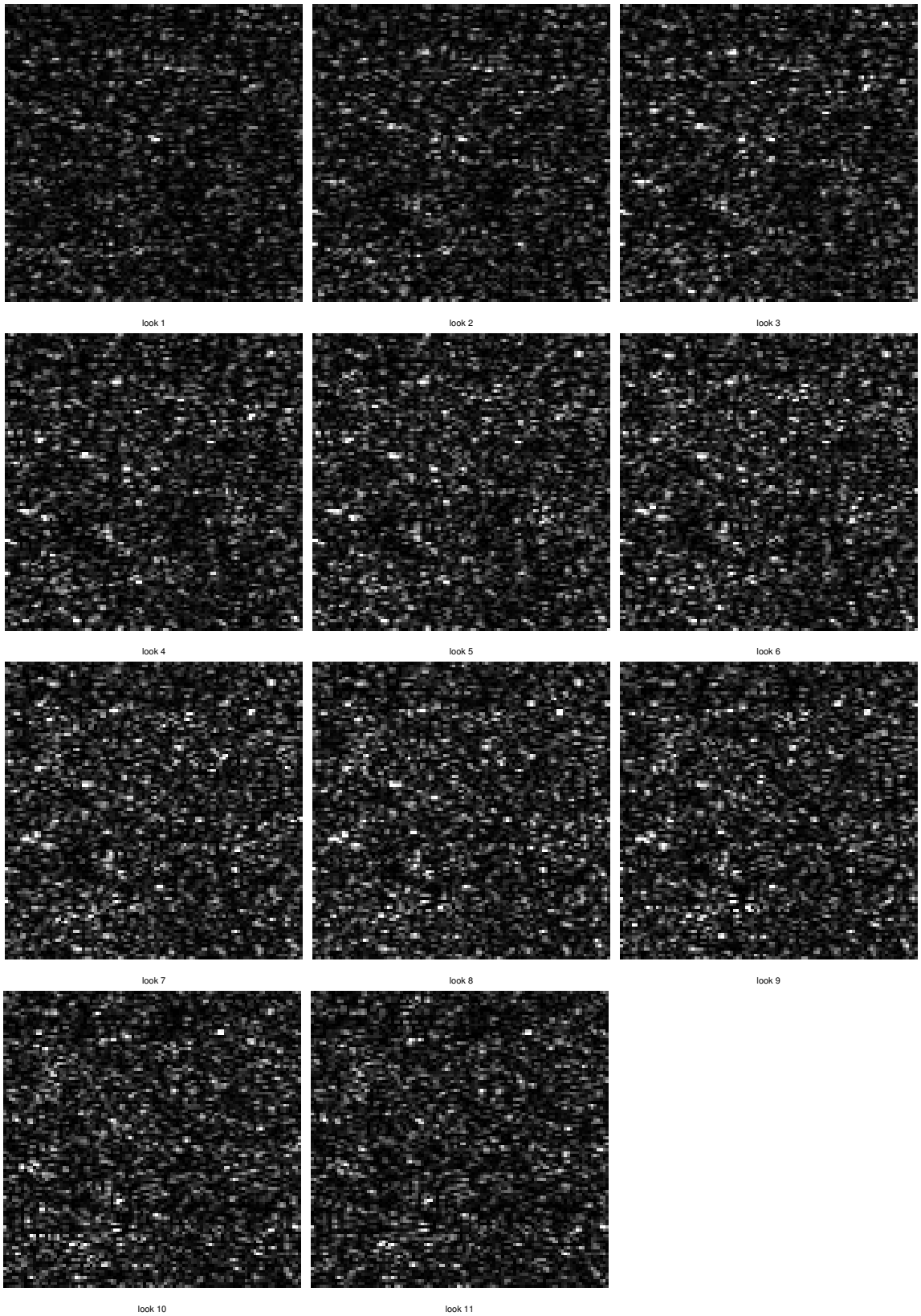

Figure D.7: Sub-images of area C in Fig.6.3.

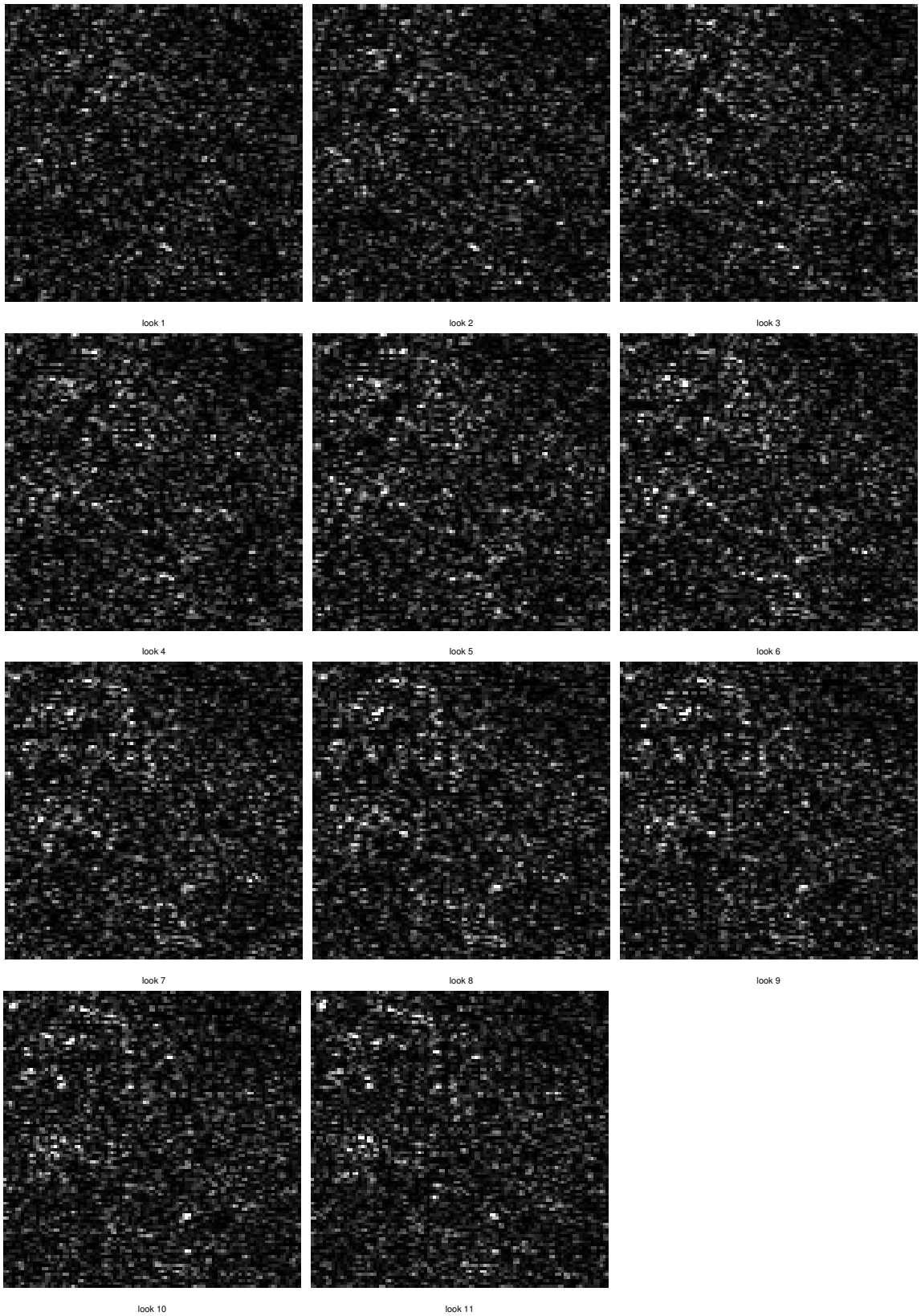

Figure D.8: Sub-images of area D in Fig.6.3.